**POLITECNICO DI MILANO**

Facoltà di Ingegneria Industriale
Corso di Laurea in Ingegneria Meccanica


# Fine abrasive water jet machining of piezoelectric ceramics

Supervisor:
Prof. M. ANNONI
Tutors :
Dr. F. ARLEO
Dr. A. SUAREZ

Tesi di laurea di:
Alessandro TROLLI Matr: 755655

Anno Accademico 2010/2011

**To my family, to my girlfriend.**

# Contents

**Abstract** 11

**1. INTRODUCTION AND LITERATURE REVIEW** 13
1.1. Introduction . . . 13
1.2. Literature review . . . 14

**2. WATER JET TECHNOLOGY** 17
2.1. The water jet system . . . 18
2.1.1. The system for water treatment . . . 18
2.1.2. The pumping system . . . 19
2.1.3. The cutting head . . . 20
2.1.4. The abrasive . . . 24
2.1.5. The catcher . . . 25
2.2. Water jet applications . . . 25
2.3. Advantages of water jet technology . . . 28
2.3.1. Advantages of water jet compared to laser machining . . . 31
2.3.2. Advantages of water jet compared to electric discharge machining . . . 32

**3. WATER JET: FROM MACRO TO MICRO** 33
3.1. The industrial state of the art of water jet technology . . . 34
3.1.1. The state of the art of conventional abrasive water jet . . . 34
3.1.2. The state of the art of micro abrasive water jet . . . 34
3.2. Conventional water jet system and miniaturized cutting head . . . 35
3.3. Applications of fine water jet . . . 37

**4. PIEZOCERAMICS: PROPERTIES AND APPLICATIONS** 45
4.1. Piezoelectric materials . . . 45
4.1.1. Polycrystalline piezoceramics . . . 47
4.1.2. Linear theory of piezoelectricity . . . 49
4.1.3. Soft and hard piezoceramics . . . 53
4.2. Piezoceramic actuators . . . 55
4.3. The key study: the bending actuators . . . 59
4.3.1. General description . . . 59
4.3.2. Functioning principles . . . 59
4.3.3. The case study: new design of piezoelectric actuators . . . 62

4.4. Fine abrasive water jet of piezoelectric ceramics against competitors . 65
4.4.1. The case study: water jet against laser machining . . . . . 66
4.5. Material removal mechanism . . . . . 67
4.5.1. Erosion mechanism of a polycrystalline ceramic . . . . . 68
4.5.2. Preliminiary experiments in Politecnico di Milano . . . . . 69

**5. INTRODUCTION TO THE EXPERIMENTAL WORK 73**
5.1. Optimization of water jet cutting: the state of the art . . . . . 73
5.2. Kerf quality attributes . . . . . 74
5.2.1. Cut geometry . . . . . 75
5.2.2. Topography of generated surface . . . . . 79
5.2.3. Integrity of generated surface . . . . . 82
5.3. Feasibility experiments in Politecnico di Milano . . . . . 82
5.3.1. Quality of the cutting surface of feasibility experiments by Università di Pisa . . . . . 83
5.3.2. Conclusions . . . . . 85

**6. EXPERIMENTAL DESIGN AND ANALYSIS OF THE RESULTS 87**
6.1. Water jet system setup and monitoring . . . . . 87
6.1.1. The hopper and the abrasive feeding system . . . . . 87
6.1.2. The fixturing system . . . . . 92
6.2. Design of experiments . . . . . 93
6.2.1. Statistical review . . . . . 94
6.2.2. Screening experiments . . . . . 94
6.2.3. Optimization experiments . . . . . 96
6.2.4. Validation experiments . . . . . 97
6.3. Analysis of results . . . . . 98
6.3.1. Kerf quality analysis of the optimization experiments . . . . . 98
6.3.2. Results summary of optimization experiments . . . . . 107
6.3.3. Kerf surface quality in validation experiments . . . . . 108
6.3.4. Scanning electron microscope analysis . . . . . 109
6.3.5. Post - Anova analysis: the Pearson - Hartley charts . . . . . 113

**7. CONCLUSIONS AND FUTURE DEVELOPMENTS 117**
7.1. Conclusions . . . . . 117
7.2. Future developments . . . . . 120
7.2.1. Fine abrasive water jet machining of hard piezoceramics . . . 120
7.2.2. Fine abrasive water jet milling of piezocomposites . . . . . 120

**Acknowledgments 125**

**A. EXPERIMENTAL DATA 127**
A.1. Optimization experiments . . . . . 127
A.2. Analysis of the kerf top width . . . . . 131

A.3. Analysis of the kerf bottom width . . . . . 135
A.4. Analysis kerf taper . . . . . 139
A.5. Analysis of kerf roughness . . . . . 143

**B. PEARSON-HARTLEY CHARTS** **151**
B.1. Operating characteristic curves . . . . . 151
B.2. Program for calculation of power and sample size . . . . . 155

**C. DATA SHEET** **161**
C.1. Water jet cutting system . . . . . 161
C.2. Optical microscope . . . . . 162
C.3. Scanning electron microscope . . . . . 163
C.4. Profilometer . . . . . 164

**Bibliography** **167**

**Elenco dei simboli** **171**

# List of Figures


2.1. System of pumping, cutting head and system for abrasive adduction (picture by Ingersoll Rand) . . . 18
2.2. Worn primary nozzle (WJ cutting of pasteboard) . . . 19
2.3. Double effect pump (1) and single effect pump (2) . . . 20
2.4. Pressure fluctuation during an experimention at Politecnico di Milano: notwithstanding the presence of an accumulator the fluctuations are not avoided, but only damped. . . . 20
2.5. Two different cutting head for pure water jet (1) and for abrasive water jet (2) . . . 21
2.6. Example of a pure water jet cutting head . . . 21
2.7. Example of injection abrasive water jet . . . 22
2.8. Effect of pressure on depth of kerf for same hydraulic power . . . 23
2.9. Example of orifice . . . 23
2.10. Scheme of focuser tube wear . . . 24
2.11. Example of Garnet abrasive . . . 25
2.12. Dragon machined from 2.5 cm thick bulletproof glass, and inlay of marble and granite . . . 25
2.13. Sandstone specimen turned by abrasive water jet . . . 26
2.14. An example of abrasive water jet milling, that uses the same nozzle and garnet abrasive that is used for conventional water jet metal cutting. . . . 26
2.15. Steel rebars after water jet fragmentation . . . 27
2.16. Water jet polishing: sea and salt removal . . . 27
2.17. Water jet cutting system in a food processing plant . . . 28
2.18. A comparison among precision water jet cutting, wire erosion, laser, conventional abrasive water jet and plasma cutting . . . 30

3.1. The special specimen studied for the comparison between macro and miniaturized cutting head on a traditional water jet system . . . 37
3.2. The minimum radius with conventional cutting head is around 700 µm, while with miniaturized cutting head is around 430 µm. . . . 37
3.3. Some micro features machining with micro water jet of different materials: a) Teflon; b) Delrin; c) Carbon steel; d) Stainless steel; e) Nitinol; f) Sterling silver . . . 39
3.4. Process chain for micro-tool manufacturing. . . . 39
3.5. Copper electrode sheet machined by WJ, 80 µm WJ nozzle and the final tool produced by MEDM. . . . 40

3.6. Eighty-five micron diameter holes on 250 µm pitch through 50 µm stainless steel. . . . . 40
3.7. Profile from 50 µm thick stainless steel, cut with 300 nm abrasive. . . . . 40
3.8. An example of profiling with thin sections (smallest division 100 µm) . . . 41
3.9. Microfluidic devices for biological analysis, fabricated by Epigem . . . . . 41
3.10. Upper side of a stent-like structure machined by (a) pure water jet and (b) by micro milling . . . . . 42
3.11. Heart patch Reinforcement (Institute Material Science – University Hannover 42
3.12. AWJ-machined orthopaedic components – scale in mm . . . . . 42
3.13. The 2-degree-of-freedom actuators developed by Dipartimento di Ingegneria Nucleare, Università di Pisa . . . . . 43
3.14. In this picture is shown a PZT pump. . . . . 43

4.1. A scheme of the main family of electro-sensible materials. . . . . 46
4.2. A scheme of the direct piezoelectric effect. . . . . 46
4.3. Graphical representation of the direct piezoelectric effect, in case of a single cell of quartz crystal; (a) undeformed cell, with no electric polarization; (b) longitudinal piezoelectric effect: the polarization arises in the same direction of the external load; (c) transverse piezoelectric effect: the polarization is normal to the load axis. . . . . 47
4.4. The picture shows the crystalline structure of barium titanate ($BaTiO_3$). . 48
4.5. Perovskit tetragonal structure of a PZT crystal . . . . . 48
4.6. Electric dipoles in piezoelectric materials before, during and after poling . 49
4.7. Hysteresis loop of a poled piezoelectric ceramic. . . . . 49
4.8. Tyipical PZT butterfly loop; over a value of tension, piezoelectric material change the direction of deformation. . . . . 50
4.9. The variation of strain caused by hysteresis is minimal for low value of applied electric field. . . . . 50
4.10. Designation of axis in piezoelectric material. . . . . 51
4.11. The typical application of piezoelectric ceramic as electric power source is in cigarette lighters. . . . . 55
4.12. Piezoelectric disk used as guitar pickup. . . . . 55
4.13. An ultrasound probe for nondestructive testing: the probe uses a piezoelectric crystal to send out ultra-sounding signals. . . . . 56
4.14. Constructive diagram of a stack linear actuator. . . . . 57
4.15. Monomorph bending beam actuator; (a) general design; (b) deformed shape when an external voltage is applied. . . . . 58
4.16. Stick-slip piezoelectric motor. . . . . 58
4.17. General architecture of the S-bender; (a) PZT layer, (b) steel layer, (c) rigid base, (d) zircon hemisphere. . . . . 60
4.18. U-bending (a) and S-bending (b) deformed shapes. . . . . 60
4.19. Stick-slip control of the S-bender actuator; (a) starting condition, (b) stick condition, (c) slip condition. . . . . 61

4.20. Orthogonal bending modes excited during the operation of a bending mode actuators. . . . 61
4.21. The theoretical trace of a bending mode actuator for one period: the elliptical motion is achieved by coupling orthogonal first-order bending modes. . . . 62
4.22. Drawing of the existing prototype of the S-bender. . . . 63
4.23. Architecture of the new 1-DOF actuator. . . . 63
4.24. Preliminary CAD model of the 2-DOF actuator. . . . 64
4.25. Geometrical parameters of the 2-DOF actuator. . . . 64
4.26. Cutting beam diameters for abrasive water jets and lasers. . . . 65
4.27. 2-DoF actuator machined at Università degli Studi Federico II di Napoli. . 66
4.28. An enlargement of 2-DoF actuator that shows clearly the heat affected zone. . . . 67
4.29. Mechanism of material removal by solid-particle erosion . . . . 68
4.30. Solid-particle material removal characteristics: a ) Micro-cutting; b) Lateral cracking. . . . 68
4.31. Steps impacted by deflected jet. . . . 69
4.32. Model of crack formed as jet exits from workpiece. . . . 69
4.33. Domain structure around cracks visualized by SEM microscopy: it's possible to see the typical intergranular cracking. . . . 70
4.34. Evidence of plastic flow and melting on an impact site of alumina ceramic sample (jet direction from right to left) . . . . 70
4.35. Enlargement of cutting surface with optical microscope. . . . 71
4.36. Picture that shows the cutting surface: the circled zone A and B are enlarged furtherly. . . . 71
4.37. Enlargement of 20x of zone A of previous picture. . . . 71
4.38. Enlargement of 20x of zone B of previous picture. . . . 72

5.1. Analysis of the costs in a water jet process. . . . 73
5.2. Enlargement Geometry of a cut generated by abrasive water jet cutting. . 76
5.3. Parameter influence on the top cut width in brittle materials . . . . 77
5.4. Parameter influence on the bottom cut width in brittle materials . . . . 78
5.5. Cut taper-formation in difficult-to-machine materials . . . . 78
5.6. Flank-angle formation in ceramic material . . . . 79
5.7. Mechanism of water jet cutting. . . . 80
5.8. Parameters influence on the surface roughness . . . . 81
5.9. Abrasive-parameters influence on the surface roughness . . . . 81
5.10. The fixturing system used during the feasibility experiments. . . . 82
5.11. Two pictures taken during the experiments . . . . 83
5.12. The specimen after the feasibility experimentation. . . . 83
5.13. Enlargement 20x of transversal section . . . . 84
5.14. Profilometer used to make roughness measurements . . . . 84

5.15. The machined surface with a SEM analysis in different conditions (the entrance of the jet is on the left side): a) f=60 mm/min p=200 Mpa; b) f = 30 mm/min p=200 Mpa; c) f = 60 mm/min p = 300 Mpa; d) f = 30 mm/min p = 300 MPa . . . . . 85
5.16. The 2-DOF actuator machined in Politecnico di Milano. . . . . 86
5.17. An enlargement of 2-DOF actuator machined in Politecnico di Milano with optimizing parameter after the feasibility experiments. . . . . 86
5.18. An enlargement of 2-DOF actuator machined in Politecnico di Milano with non-optimizing parameter after the feasibility experiments. . . . 86

6.1. The 3D-drawing of the new mini-hopper designed in cooperation with Tecnalia: 1) lower base; 2) cylinder; 3) upper base; 4) selector base; 5) lid; 6) rod; 7) selector; 8) selector of flow rate . . . . . 88
6.2. The self-made mini hopper installed in the water jet system. . . . . 89
6.3. Good orifice: the signal shows that the working pressure does not influence the depression in the abrasive system. . . . . 90
6.4. Worn orifice: the signal shows that the working pressure influences the depression in the abrasive system. . . . . 90
6.5. The signal shows that the pressure fluctuations do not influence the depression in the abrasive system if the orifice is in good conditions. . 91
6.6. The signal shows that the pressure fluctuations influence the depression in the abrasive system if the orifice is worn. . . . . 91
6.7. The distance among the peaks is more less 2,85 mm, that is equivalent to a frequency of 0,64 Hz. . . . . 92
6.8. Depression fluctuations affect directly the quality of the cut surface. . 92
6.9. The fixturing system used during this experimentation. . . . . 93
6.10. The final setup of the waterjet system used to machine piezoelectric material. . . . . 93
6.11. Kerfs quality at feed rates of 190 mm/min . . . . . 95
6.13. Kerfs quality at feed rates of 110 mm/min . . . . . 95
6.12. Kerfs quality at feed rates of 150 mm/min . . . . . 96
6.14. Machining of the piezoelectric material . . . . . 97
6.15. The two 2-DoF machined by (a) Garnet#200 and by (b) Alumina#220 98
6.16. An enlargement of the detail machined only by water after the clogging of Alumina#220. . . . . 98
6.17. The kerf taper is characterized by simmetry . . . . . 99
6.18. The main effects plot for the top kerf width. . . . . 99
6.19. The interaction plot for the top kerf width . . . . . 100
6.20. The analysis of the machined top kerf width. . . . . 101
6.21. The main effects plot for the bottom kerf width. . . . . 101
6.22. The interaction plot for bottom kerf width. . . . . 102
6.23. The analysis of the machined bottom kerf width. . . . . 103
6.24. The main effects plot for the kerf taper. . . . . 103
6.25. The interaction plot for the kerf taper. . . . . 104

6.26. The profilometer used during the analysis . . . . . 105
6.27. The main effects plot for the roughness. . . . . 106
6.28. The interaction plot for the roughness. . . . . 106
6.29. An example of the program output for roughness measurement. . . . 107
6.30. Angles machined by Garnet#200 (a) and by Alumina#220 . . . . . 109
6.31. Back side machined by Garnet#200 (a) and by Alumina#220 . . . . 109
6.32. The kerf structure of the PZT material with an enlargement of 5.000X. 110
6.33. The brittle fracture is dominant, but there are also tracks of ductile fracture. . . . . 111
6.34. An abrasive particle embedded in the ceramic material. . . . . 111
6.35. Enlargement of 2.500X for different feed rate: a) 30 mm/min; b) 70 mm/min; c) 110 mm/min . . . . . 112
6.36. The chemical analysis of the abrasive particles . . . . . 113
6.37. Pearson – Hartley charts for the calculation of the analysis power. . . 114
6.38. Calculation of the maximum detectable difference due to the power. . 115
6.39. Pearson – Hartley charts for the calculating of the sample size, setting a power of 90% . . . . . 115

7.1. The structure of the specimen at the exit is characterized by chipping. 118
7.2. The chipping phenomenon in piezoelectric material: a) it's evident that the entrance of the jet is on the right side; b) on the bottom side there are considerable craters, as highlighted in the red circle . . . . . 119
7.3. The "cracking among powder particles" is the typical fracture mode of piezoelectric ceramic. . . . . 119
7.4. Composites by Smart Materials Corp: a) rectangular fibers, b) round fibers. . . . . 121
7.5. The fixturing system is composed by polystyrene and sellotape . . . . 122
7.6. Milling attemps at p=200 MPa and v=600 mm/min. In the case of clogging abrasive or too high forces the brittle behaviour of the material is evident, with the typical macro craters. . . . . 122
7.7. The fixturing system is composed by a metallic bar and glue . . . . . 123
7.8. An enlargement of 15x of the specimen, machined with pressure 200 MPa, feed rate 1000 mm/min, Garnet#200 and abrasive flow rate 80 g/min . . . . . 123
7.9. The specimen machined by fine abrasive water jet technology . . . . . 123

A.1. Main effects plots for top kerf width. . . . . 131
A.2. Interaction plot for top kerf width. . . . . 132
A.3. The probability plot shows the normality of the residuals (p-value bigger than 0,05) . . . . . 133
A.4. The test for equal variances shows that the variances are homogenous (p-value bigger than 0,05) . . . . . 133
A.5. The time series plot shows that there aren't any trends, but the residuals are independent: it's useful to see a systematic error. . . . . 134

A.6. Main effects plots of the bottom kerf width. . . . . 135
A.7. Interaction plot for bottom kerf width. . . . . 136
A.8. The probability plot shows the normality of the residuals (p-value bigger than 0,05) . . . . . 137
A.9. The test for equal variances shows that the variances are homogenous (p-value bigger than 0,05) . . . . . 137
A.10. The time series plot shows that there aren't any trends, but the residuals are independent: it's useful to see a systematic error. . . . . 138
A.11. Main effects plots of the kerf taper. . . . . 139
A.12. Interaction plot for the kerf taper. . . . . 140
A.13. The probability plot shows the normality of the residuals (p-value bigger than 0,05) . . . . . 141
A.14. The test for equal variances shows that the variances are homogenous (p-value bigger than 0,05) . . . . . 141
A.15. The time series plot shows that there aren't any trends, but the residuals are independent: it's useful to see a systematic error. . . . . 142
A.16. Main effects plots of the roughness. . . . . 143
A.17. Interaction plot for the roughness. . . . . 144
A.18. The probability plot shows the non-normality of the residuals (p-value smaller than 0,05) . . . . . 145
A.19. The test for equal variances shows that the variances are homogenous (p-value bigger than 0,05) . . . . . 145
A.20. The time series plot shows that there aren't any trends, but the residuals are independent: it's useful to see a systematic error. . . . . 146
A.21. The Box-Cox plot shows the estimate lambda, that is necessary to transform the original data into data with normal distribution . . . . 146
A.22. The probability plot shows the non-normality of the residuals (p-value smaller than 0,05) . . . . . 147
A.23. The test for equal variances shows that the variances are not homogenous (p-value smaller than 0,05) . . . . . 147
A.24. The time series plot shows that there aren't any trends, but the residuals are independent: it's useful to see a systematic error. . . . . 148
A.25. The probability plot shows the normality of the residuals (p-value bigger than 0,05) . . . . . 148
A.26. The test for equal variances shows that the variances are homogenous (p-value bigger than 0,05) . . . . . 149
A.27. The time series plot shows that there aren't any trends, but the residuals are independent. . . . . 149

B.1. An exemple of Pearson-Hartley Charts. . . . . 153
B.2. An example of the ouput of the program, which can plot the operating characteristic curves. . . . . 154

C.1. Water jet cutting system used in this experimentation . . . . . 162

C.2. The optical microscope used in this experimentation . . . . . 163
C.3. The scanning electron microscope used in this experimentation . . . . 164
C.4. The profilometer used in this experimentation . . . . . 165

# List of Tables


2.1. A comparison of peculiar feature of conventional AWJ, MAWJ, Laser, EDM and micro machining. . . . . 30

3.1. Some peculiar features for water jet system, taken from the website of different companies. . . . . 34
3.2. Some peculiar features of water jet system for micro manufacturing, taken from the website of different companies. . . . . 36
3.3. Parameters of macro AWJ and fine AWJ used for the comparison. . . 37
3.4. A complete summary of the materials that can be cut with water jet. . . . 38

4.1. A summary of the mechanical and electric properties of lead zirconate titanate ceramic (PZT ceramic) . . . . . 53
4.2. Table of mechanical and electric characteristic of different piezoelectric materials: in the red column the soft piezoelectric used in this experimentation, in the blue column a hard piezoelectric . . . . . 54
4.3. A summary of 1-DOF actuator dimensions . . . . . 62
4.4. A summary of 2-DOF actuator dimensions . . . . . 64

5.1. The parameters investigated by the experimenter . . . . . 75
5.2. The measurement of roughness . . . . . 85

6.1. Calibration of abrasive system . . . . . 89
6.2. Constant parameters used in this experimentation . . . . . 94
6.3. Constant parameters used in this experimentation . . . . . 95
6.4. Parameters of optimization tests. . . . . 96
6.5. Mean value and standard deviaton of top kerf width. . . . . 100
6.6. Mean value and standard deviaton of the bottom kerf width . . . . . 102
6.7. Mean value and standard deviaton of the taper of the cut . . . . . 104
6.8. The table of ISO 4288-1996 . . . . . 105
6.9. Mean value and standard deviaton of the roughness . . . . . 107
6.10. Significant parameters. . . . . 107
6.11. Optimal parameters. . . . . 108
6.12. Mean value and standard deviaton of kerf roughness. . . . . 108
6.13. Chemical analysis of the abrasive particles embedded in the machined kerf . . . . . 114

A.1. Experimental data. . . . . 127

B.1. Operative characteristic curve parameters for the two factor-factorial, fixed effects model. . . . . 153

C.1. Data sheet of ByJet Classic 3015 . . . . . 161
C.2. Data sheet of Motic SMZ - 140 Series . . . . . 162
C.3. Data sheet of Motic SMZ - 140 Series . . . . . 163
C.4. Data sheet of Mitutoyo SV - 2000N2 . . . . . 164

# Abstract

Advanced ceramics are increasingly applied in optical, electronic, mechanical and biomedical applications thanks to their inherent physical properties such as electrical behavior, electromagnetic response, high temperature strength, hardness and corrosion resistance. Nevertheless, this kind of materials are usually very difficult-to-machine by conventional technologies, while their applications become more and more demanding in terms of quality and precision. In such scenario, the Fine Abrasive Water Jet (FAWJ) represents a very appealing and promising technology compared to micromachining, laser or EDM, offering many advantages such as the absence of thermal distortions, high flexibility and versatility, small cutting forces and the increasing capability to cut smaller and smaller features. In the present work, carried out at Tecnalia R&I in collaboration with Politecnico di Milano, the machining of thin sheets of piezoelectric material (lead titanate zirconate, also called PZT) is investigated with a DOE approach, in order to optimize the FAWJ system cutting parameters, to test its capability and to demonstrate this is a concrete alternative to high-precision machine ceramic materials. Finally, a possible application of PZT as actuator for micro positioning is presented.

Keywords: fine abrasive water jet, piezoelectric ceramic, cutting optimization, design of experiments

# 1. INTRODUCTION AND LITERATURE REVIEW

## 1.1. Introduction

Engineered ceramic materials exhibit a host of very attractive properties for today's scientists, design and R&D engineers. Properties of interest include high hardness, high thermal resistance, chemical inertness, tailored electrical conductivity, high strength-to-weight ratio and longer life expectancy. These characteristics make ceramic materials, particularly piezoelectric ceramics, attractive for a variety of applications, including structural, semiconductor, micro electromechanical systems (MEMS), medical, defense, aerospace and electronics. Many of these applications demand intricate shapes, tighter tolerances and finer, more precise dimensions. In addition, minimal surface damage and very specific surface characteristics are critical in many end uses. Water jet technology can satisfy the particular requirements of these kinds of materials. Conventional forming and sintering techniques are often not able to meet these demands. Diamond tool machining is limited in the number of feature shapes and sizes possible, and is also time consuming. Electrical discharge machining (EDM) offers a range of feature shapes and sizes, but it is only suitable for use on conductive materials. Since laser machining is a thermal process, heat-affected damage does occur and can have a negative impact on the end use, especially in high-reliability applications. In contrast, abrasive water jet is a non-thermal, non-chemical and non-electrical machining process that leaves the chemical composition, material microstructure and physical properties of the workpiece unchanged.
The aim of this thesis work is to demonstrate the capability of water jet to machine

a typical difficult-to-cut material such as the piezoelectric ceramics. This thesis work represents also a first attempt to optimize cutting parameters, to overcome the lack of precision, a typical problem of water jet machining. Moreover, an accurate analysis with scanning electron microscope (SEM) is made to characterize the piezoelectric ceramic micro structure and the interaction between abrasive particle and material. In addition, a possible application is presented: a piezoelectric actuators for micro positioning. This application could represent a new market, in which fine abrasive water jet (FAWJ) is a very appealing technology.

## 1.2. Literature review

Few works in literature focus on topics regarding the micro abrasive water (MAWJ) jet of hard-to-machine materials, such as ceramics. However, a review on traditional WJ machining it's necessary to better understand the mechanism of micro water jet cutting and the problems related to it.
M. Monno et al. [1] summarized the characteristic of traditional water jet technology and its peculiarity. A. W. Momber and R. Kovacevic [2] made a state of the art of this technology, analyzing possible machining process, material removal mechanism and the quality of kerf.
MAWJ technology is an innovative machining process, so the literature about this topic is poor of books, scientific papers, proceedings of conference, dissertations and articles. However, these few articles represent a very effective background of knowledge and so are very helpful to get aware of the problems and difficulties concerning an experimental approach. The first contributions on these topics were given in 1999 by D. Miller [3], who presented the developments of micro abrasive water jets of 50 μm diameter and, furthermore, he introduced some possible industrial applications for this technology. From this perspective, the article of O. Blatnik et al. [4] is meaningful, because it explains a possible application of water jet technology in combination with micro electric discharge machining (MEDM) for tooling production in micro manufacturing. I. Sabotin et al. [5] evaluated the possibility to use micro water jet in an alternative process chain producing electrodes for MEDM: aim of this work is to investigate on repeatability and limitations of producing microchannel structures through statistical analysis.
To better understand the machining mechanism of ceramic materials and the cutting parameters used, a review about these materials is necessary. T. Aklint et al. [6] evaluated the micro cutting of alumina and single crystal materials as silicon and sapphire, analyzing the cutting accuracy, precision, taper angle and circularity of hole diameters. Furthermore, some articles investigated the cutting of ceramics materials in order to create a predictive statistical model. Among the others, P. Gudimetla et al. [7] investigated the machinability of industrial ceramics and the kerf formation characteristics associated with the abrasive water jet cutting. J. Wang [8] carried out an experimental study on the effects of nozzle oscillation,

in order to create a predictive depth of jet penetration model for AWJ cutting of alumina ceramics. J.Wang et al. [9] carried out an experimental investigation to minimize the kerf taper in abrasive water jet cutting of alumina ceramics by using a kerf-taper compensation technique.
Many works have been carried out with an experimental approach based on statistical methods. Among the others, A. Devineni [10] discussed the use of abrasive water jet for the cutting of glass, investigating of the combined effect of process parameters on the depth of cut and kerf using Design Of Experiments. F. Kolahan et al. [11] presented a work dealing with the effects of various parameters, such as nozzle diameter, jet traverse rate, jet pressure and abrasive flow rate, in cutting of an aluminum alloy using regression analysis. J. Wang [12] discussed the influence of multipass on industrial ceramics, giving a general guide to the selection of cutting parameters, basing on an experimental analysis.
Nevertheless, a brief review about piezoelectric materials and piezoelectric actuators is helpful. R. Guo et al. [13] described the industrial process to obtain lead zirconate titanate ceramics (PZT), analyzing piezoelectric and mechanical properties of this material. A. Bellosi et al. [14] studied ceramic materials in order to define relationship among micro-structures (in the micro- and nano-size range) and mechanical properties. J. Watson et al. [15] demonstrated how piezoelectric ultrasonic actuators have the greatest potential to produce a varied range of micro/milli-scale designs.
These works are a selection among the several works reviewed during the present study and effectively forming its theoretical background guideline. Moreover, further works are referenced throughout the present work concerning specific topics presented in each section.

# 2. WATER JET TECHNOLOGY

Water jet machining is a relatively recent and promising technology because of its inner simplicity and extreme flexibility.
The machining energy carrier is water, a fluid characterized by large availability in nature, low cost and low environmental impact. Despite water (for the pure jet) and abrasive plus water (for the abrasive water jet) are very common in nature, water jet technology is considered an unconventional technology for its peculiar machining of materials and its common fields of application. The physical process is quite simple because it consists in the conversion of energy pressure into kinetic energy: the high-pressure water is forced into an orifice and converted in a high-velocity water jet whose huge amount of kinetic energy is able to machine almost any kind of material.
The first work with water jet was in 1930s, when low-pressure jet was used in coalmines in Russia. Day by days, the capability of pressurizing water increased, and that technology was exploited industrially, especially for material removal and surface cleaning. N. Franz is regarded as the father of water jet. He was the first person who studied the possibility to use the ultrahigh-pressure water as a cutting tool. In the 1950s, Dr.Franz, a forestry engineer, forced pressured water through a tiny orifice. In this way he was able to cut wood and other materials. Eventually N. Franz proved that a focused beam of water at very high velocity has enormous cutting power, which can be used in several industrial applications. However, the technology didn't develop until 1970s, when abrasive was added to the jet thanks to the studies of M. Hashish. Since then, many types of water jet have been developed, including abrasive water jets, cavitation jets, ice water jets, hybrid jets [1].
Nowadays, many research centers and also manufacturers are carrying out several studies to better understand the mechanics of material removal and to optimize the process parameters. A versatile WJ machining process is the answer to the

industrial demand for new and improved ways to manufacture products of complex geometry in high-strength materials. The reason of the growth of this technology is surely the possibility to cut easily a wide variety of materials, the non-intrusiveness due to low forces transmitted to the workpiece, the presence of no heat-affected zone and the environmental sustainability. These main advantages make WJ technology particularly suitable and competitive for modern unconventional machining.

## 2.1. The water jet system

The WJ system is composed by:

- a system for water treatment
- a low-pressure (oil circuit)
- a high-pressure circuits (intensifier)
- an accumulator a cutting head
- a catcher

A typical water jet system is shown in **Figure2.1**.

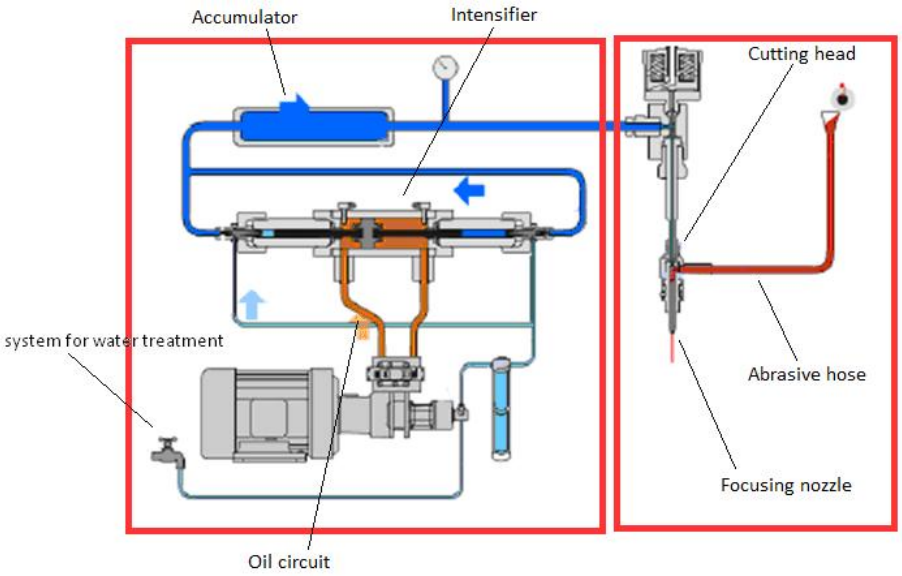


**Figure 2.1.:** System of pumping, cutting head and system for abrasive adduction (picture by Ingersoll Rand)

### 2.1.1. The system for water treatment

The system for water treatment is specifically set up for any single water jet plant depending on the water quality coming from the water network. Solid particles in

the water can accelerate the wearing of the pumping system, pipes, valves, focuser and orifices, as shown in **Figure 2.2** ([16]).

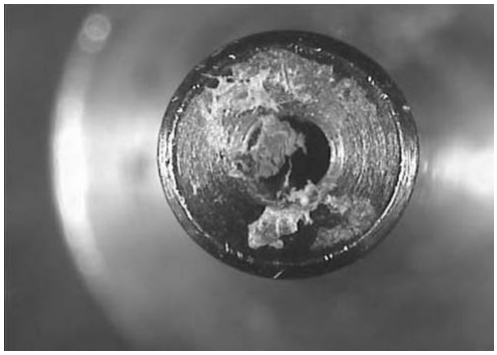

**Figure 2.2.:** Worn primary nozzle (WJ cutting of pasteboard)

Moreover, calcium and magnesium salts dissolved in water can create deposits which reduce the efficiency of the water jet system increasing the pressure drop and cause dangerous pipe clogging; besides, chlorides and sulfates can cause the corrosion of metallic parts. The water treatment system is a vital component of the machine. Installed upstream the pumping system, it is usually composed by micrometric filters and a reverse osmosis apparatus: in this way, the pureness of the water is guaranteed.

### 2.1.2. The pumping system

Since the pressure is one of the most important parameters in a water jet process, the pumping system is the heart of a water jet system and it is composed by the pressure system and the accumulator. The high-pressure circuit is powered by the water pump actuated by the oil coming from the low-pressure circuit: the water pressure is increased proportionally to the ratio between the areas of the primary and secondary piston, as shown in **Eq.2.1**:

$$P_{water} \cdot S_{water} = P_{oil} \cdot S_{oil} \rightarrow P_{water} = P_{oil} \cdot \frac{S_{oil}}{S_{water}} \tag{2.1}$$

Currently, two types of intensifiers are used: single effect pump and double effect pump, as shown in **Figure 2.3**.

The advantage of a single effect pump is the elimination of the accumulator which is needed in the case of double effect pump for the damping of pressure fluctuations, visible in **Figure 2.4** during an experimentation at Politecnico di Milano. In fact, a correct phasing of single effect pumps allows a more regular supply of the pressure and the accumulator is not needed. The water pressure reachable with this pumping system is commonly around 400 MPa.

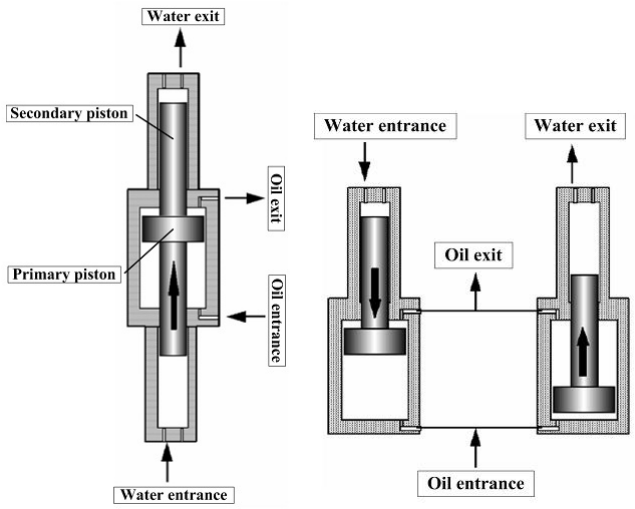


**Figure 2.3.:** Double effect pump (1) and single effect pump (2)

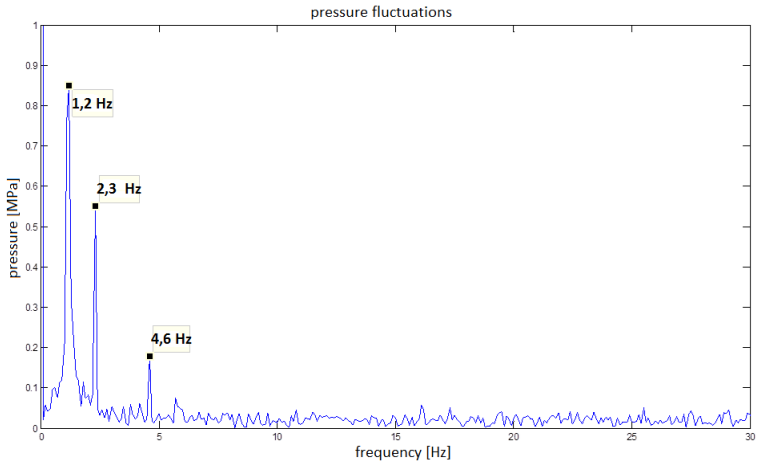


**Figure 2.4.:** Pressure fluctuation during an experimention at Politecnico di Milano: notwithstanding the presence of an accumulator the fluctuations are not avoided, but only damped.

### 2.1.3. The cutting head

The cutting head is the responsible for the transformation of pressure energy into kinetic energy and the cutting water jet formation; it is composed by several elements whose design and geometry affect its efficiency. The two most common technologies in cutting are pure water jet and abrasive water jet, as shown in **Figure 2.5**.

In the pure water jet, the tool that machines the material is only made by water. A

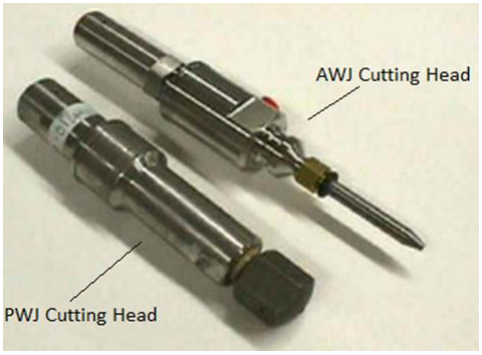


**Figure 2.5.:** Two different cutting head for pure water jet (1) and for abrasive water jet (2)

typical water jet cutting head is shown in **Figure 2.6**. This kind of jet is industrially used to cut low-hardness and low-density materials, such as leather, paper, pasteboard, wood, food, plastic, clothes, foam, etc. Typically, the orifice diameters are very small (around 0,1 mm), in order to concentrate all the energy in the smallest area and increase the jet specific energy.

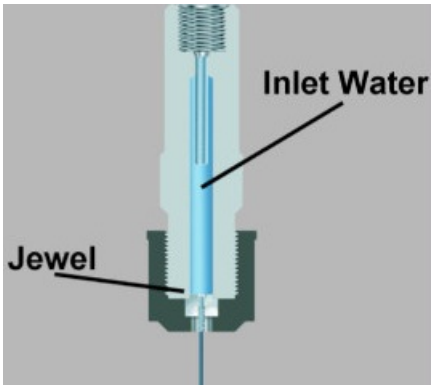


**Figure 2.6.:** Example of a pure water jet cutting head

The abrasive water jet (AWJ) is obtained by adding abrasives to the jet in order to increase its erosive power and allow to machine harder materials such as metals, ceramics and piezoelectric materials, composites and multi-layer materials, glass, metal matrix composites and sandwich materials.
There are two typical abrasive water jet configurations: injection jet and suspension jet.
In the abrasive water injection jet (AWIJ) (**Figure 2.7**), the high-velocity water jet is used to transfer its momentum to abrasive particles which are added downstream to it inside a mixing chamber and accelerated inside a focuser: the impact exerted by these high-speed particles when they hit the workpiece causes material removal of the workpiece. Generally, for conventional AWIJ the orifice diameter is around

0.3 mm, the diameter of the focuser is around three times bigger (around 1 mm) and its total length is 75 mm.
In an abrasive water suspension jet (AWSJ), a pre-mixed water-abrasive slurry is directly pumped through the nozzle, in order enhance the momentum transfer and so the power density of the abrasive particles.

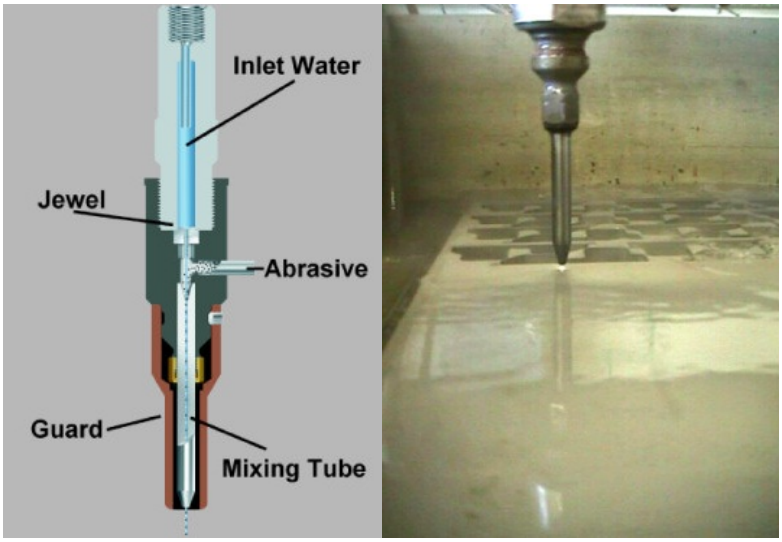


**Figure 2.7.:** Example of injection abrasive water jet

The performance comparison of AWIJ and AWSJ is shown in **Figure 2.8** ([1]), in the case of same hydraulic power input and in the case of same generated width of kerf. The comparisons have shown a twice deeper depth of kerf by using an AWSJ with the same hydraulic power as the AWIJ system. In the case of same width of kerf, that means nozzle diameter and focus diameter are the same, the depth of cut is four times deeper by a ten times higher hydraulic power.

In conclusion, the AWSJ has much higher cutting performance compared to AWIJ, as above mentioned. Anyway, it still suffers some big disadvantages in terms of process management and maintenance: for this reason, the AWIJ is certainly much more common than AWSJ.
As previously mentioned, a typical cutting head for AWIJ is composed by an orifice, a mixing chamber and a focuser. The orifice (**Figure 2.9**) is in contact only with pressured water so it has to bear high pressure and resist to wear. Orifices are typically made by synthetic sapphire and are inexpensive (from 5 to 50 €). There are also diamond orifices (200 € and up) which can last much longer (the average life is about 100 hours for a sapphire orifice and 1000 hour for diamond orifice) due to the higher hardness and wear resistance [16]

The mixing chamber carries abrasive into the jet and transfers momentum to abra-

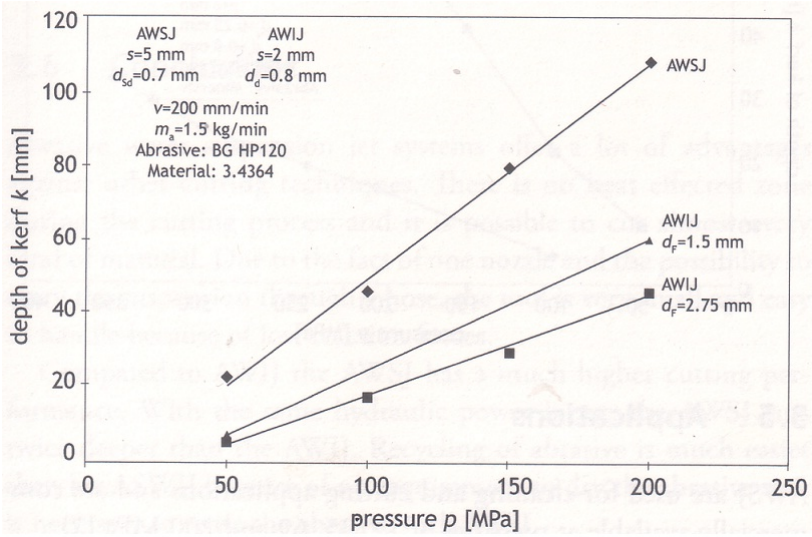


**Figure 2.8.:** Effect of pressure on depth of kerf for same hydraulic power

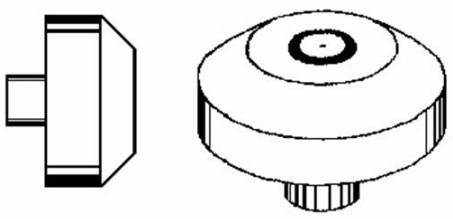

**Figure 2.9.:** Example of orifice

sive particles. Its geometry eases the entrance of abrasive and assures an optimal mixing between the two phases (water-abrasive).
Downstream the mixing chamber, the jet is constituted by three phases (air-water-abrasive) and turns out markedly divergent, a characteristic which reduces the power density available for the cutting. The focuser has the task to increase the momentum transfer between water and abrasive, and, meanwhile, to make the stream coherent and collimated. In the focuser, the mechanism of material removal is both erosion and abrasion, as shown in **Figure 2.10**. The main causes for the substitution of focuser are wear (85%) and break (13%). They are made in wolfram carbide since it has the best resistance compromise between erosion and abrasion and so the best wear resistance [16].

Abrasive water jet is a mixture of water and particles and this brings several limitations and inconveniences. Although acceptable, the energy efficiency of abrasive water jet is still low and strongly dependent on the water-particles interaction efficiency; nevertheless the mixing between water and particles limits the minimization of the jet diameter and special solutions are required for particles supply and dis-

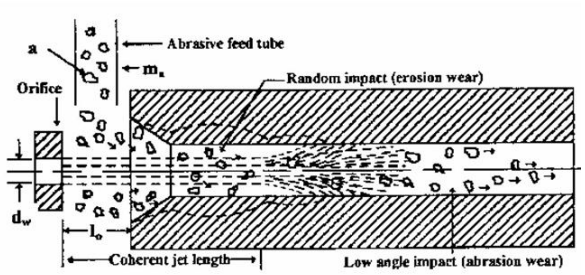


**Figure 2.10.:** Scheme of focuser tube wear

posal. Besides, the addition of abrasive particles increases the cost of processing and its environmental impact.
It would be highly desirable to enhance the water jet productivity and also to avoid the usage of traditional abrasives which are usually difficult to dispose. This objective can be achieved by the replacement of conventional abrasive materials by ice particles, thus resulting in formation of ice-water jet (IWJ). The solid ice particles are able to erode the material during the impingement. Instead of water, the use of cryogenic fluid, such as liquid nitrogen, ammonia and carbon dioxide aids to eliminate off-products as well as substrate contamination. The obvious difficulty of this technology is the necessity to maintain a working fluid at a cryogenic temperature. The most effective way to improve jet performance without water contamination is addition of small amount of polymers, which increase jet coherence. This last method is adopted by industry[1].

### 2.1.4. The abrasive

In AWJ the tools which machine the workpiece are just the abrasive particles, while the water task is only to transfer its energy to abrasives. The peculiar proprieties of abrasive particles are:

- homogeneous size (controlled by the mesh number)

- minimized dust contents, both for operator safety and to avoid problems of clogging in mixing chamber

- no hygroscopicity

The Garnet (garnet–almandite) is the most common abrasive for its good property in material cutting and its relatively low-cost. Garnet (**Figure 2.11**) is the most highly efficient, effective and safe abrasive for both wet and dry blasting applications.

There are also other abrasive, which can be industrially used, such as alumina and olivine abrasive. Alumina abrasives are primarily used as mechanical abrasives because of their high hardness and durability. Olivine is known for its high hardness,

**Figure 2.11.:** Example of Garnet abrasive

low uniform thermal expansion, sharp edges and its remarkable ability to resist to fracture from thermal and impact shock.

### 2.1.5. The catcher

The catcher collects water, abrasive and scraps at the end of working. Furthermore, the catcher has also the function of damping the remaining kinetic energy of the jet, protecting operator and machine parts.

## 2.2. Water jet applications

Industrial demand for new and improved way to machine products of complex geometry in high-strength materials often turns on the attention to the possible use of abrasive water jet machining process. Water jets have been adapted to perform a wide range of operation:

- Cutting: the jet is used to cut shapes from several materials, as shown in **Figure 2.12**.

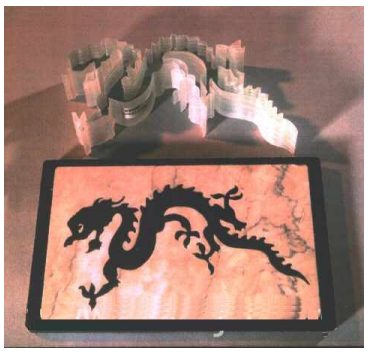

**Figure 2.12.:** Dragon machined from 2.5 cm thick bulletproof glass, and inlay of marble and granite

- Drilling: the jet is used to pierce a hole without trepanning; this technique for obtaining small diameter holes attract industrial attention as a replacement for EDM or laser drilling operations, which share a drawback in their use of thermal processes for material removal.

- Turning: the jet is used to create a axis-symmetric surface as shown in **Figure 2.13**. Water jet turning is a relatively simple process: the workpiece rotates while the abrasive water jet is traversed axially and radially to produce the required turned surface. This technique may facilitate production of rotational-symmetries in hard-to-cut materials.

**Figure 2.13.:** Sandstone specimen turned by abrasive water jet

- Milling: the jet is used to remove material to a specific depth, as shown in **Figure 2.14**. To control and limit the depth of cut by a water jet, either the jet needs to be weak or moving at relatively high feed rates. Another approach involves the use of masks made out of more resistant materials: a steel mask can be used for aluminum or titanium workpieces. Other materials may need a tungsten carbide mask.

**Figure 2.14.:** An example of abrasive water jet milling, that uses the same nozzle and garnet abrasive that is used for conventional water jet metal cutting.

- Fragmentation: the jet is used to break the workpiece, as shown **Figure 2.15**.

- Water jet assisted process: the jet is used to assist other material removal processes such as cooling, lubrification, debris removal, and laser beam guiding. The use of

laminar water jets (0,1 mm) to guide pulsed Nd:YAG laser beams for cutting, drilling and surface structuring has been commercially introduced: the laser is the primary cutting tool, while the water jet acts as a guide and coolant.

**Figure 2.15.:** Steel rebars after water jet fragmentation

- Surface treatment, the jet is used to modify the surface such as cleaning, rust removal, peening, texturing, stripping or polishing, as shown in **Figure 2.16**.

- Ferrling, deburring, peeling, powder fabrication. In powder fabrication the impact of water jets on molten metal streams causes them to disintegrate and form powder: three converging water jets are used to provide a symmetric impingement forces on a central stream of molten tin.

**Figure 2.16.:** Water jet polishing: sea and salt removal

- Forming: the jet is used to generate on the workpiece a permanent plastic deformation.

- Food processing: water jet tools have been used in a wide variety of food processing applications, such as for portioning chicken (**Figure 2.17**), meat and fish. The use of pressure is becoming more attractive for food sterilization compared to heat, chemical and irradiation method.

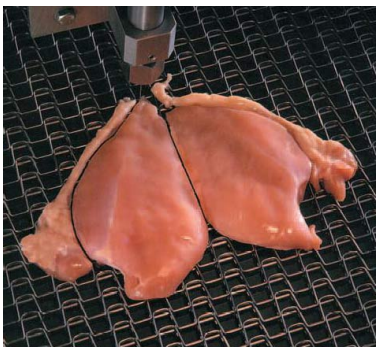

**Figure 2.17.:** Water jet cutting system in a food processing plant

## 2.3. Advantages of water jet technology

In this section the advantages of water jet technology is presented in comparison with the direct competitors in micro manufacturing, such as laser and EDM.
The water jet not only transfers its kinetic energy to entrained abrasive particles but also acts as a coolant to carry away the heat generated by the erosion process. As a result, there is no heat affected zone (HAZ) in the materials which might induce thermal damage on the workpiece. It is then possible to machine without surface hardening and/or localized modification of the chemical properties of the parent material, neither generating poisonous fumes nor re-casting or warping.
Abrasive water jet machining is characterized by environmental sustainability: it typically uses garnet as abrasive material which is a non-reactive biologically inert mineral. If the machined material is hazardous, the used abrasive and the waste material become suitable for landfill.
Furthermore, the process causes low mechanical stresses on the machined material: water jet machining induces light compressive stresses, abrasion and erosion into the material, but the machined surface doesn't show any residual stresses and the roughness is quite (Ra=1-2 μm); moreover, there is nearly burr production, except for ductile materials and thin thicknesses.
Among the advantages above-mentioned, the followings are responsible for the future growth of this technology:

- abrasive water jet machining is fundamentally cost-effective with fast turnaround: a part can be completed from design to finish from minutes to hours;

- one of the major advantages of abrasive water jets is their versatility. They are material independent as they can cut all materials according to their machinability: the mixture of water and abrasive can machine a wide variety of materials, from metallic materials to composite materials as well as glass. The only constraint is that the hardness of abrasive particles has to be stronger than the machined material;

- another advantage of abrasive water jets is their ability in easily machining thick materials, up to 30-cm thick. Abrasive water jet also cut thick heat-treated steel

that presents considerable challenges to most of the conventional process. Extremely hardened steel is not only slow to be cut by contact tools but often leads to frequent tool breakage. In most cases, parts must be machined by conventional tools prior the heat treatment. Post heat treatment leads to dimensional distortion and might need further machining to meet the specifications [17];

- abrasive water jet exerts a very small force to the workpiece during piercing and cutting, so that only simple fixing is required. The small force also allows machining large-aspect-ratio slots and ribs that are difficult to achieve otherwise with conventional tools such as pressing [17];

- the process is characterized by a kerf with relatively small width: the amount of material removed by water jet stream is generally around 1,1 mm wide, that means that very little material is removed in passing through cut. When working with expansive materials (like titanium), precious materials (like gold) or hazardous materials (like lead), this can be a meaningful benefit. Besides, this can mean that more parts can be cut from a given sheet of material;

- for applications affected by fatigue resistance, abrasive-water jet-machined aircraft metals are required to go through the secondary trimming by conventional machining to avoid that the striations induced by the abrasive water jet become a source of microcracks premature initiation after many loading cycles. Such problem has greatly limited in terms of cost-effectiveness the spreading of this this technology. A recent revisit of abrasive-water jet machining has shown that applying simple dry-grit blastings as a secondary treatment to remove the visual appearance of striation pattern has increased the fatigue life of abrasive-water jet-machined aluminum and titanium at least three time compared to those of traditionally-machined counterparts [17][18];

- the process is reproducible (and the tolerances are very little [5];

- this technology can satisfy both high production volumes and little batches.

As water jet is trying to gain more important place among non-conventional cutting technologies. Next sections will present a series of advantages which water jet offers when compared to two direct competitor technologies such as laser and electric discharge machining (EDM). Another competitor could be plasma cutting, but, as shown in **Figure 2.18** ([19]), the comparison for micro manufacturing is not meaningful.

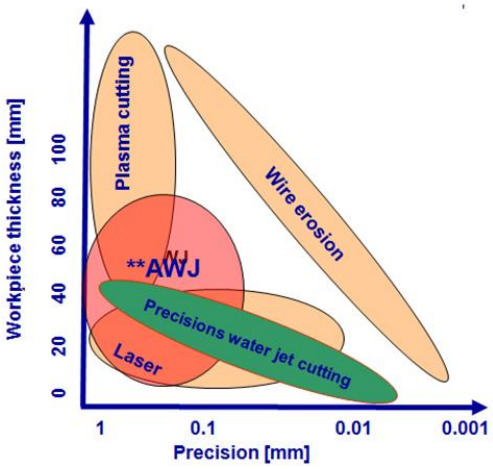


**Figure 2.18.:** A comparison among precision water jet cutting, wire erosion, laser, conventional abrasive water jet and plasma cutting

A summary of the characteristics of these technologies is shown in **Table 2.1**.

**Table 2.1.:** A comparison of peculiar feature of conventional AWJ, MAWJ, Laser, EDM and micro machining.

| | **Conventional AWJ** | **Micro AWJ** | **Laser** | **EDM** | **µMachining** | **UM** |
|---|---|---|---|---|---|---|
| **Repeatability** [mm] | ± 0,05 | ± 0,005 | very high | high | ± 0,0005 | not available |
| **Parts Accuracy** [mm] | ± 0,01 | ± 0,01 | very high | ± 0,005 | ± 0,001 | ± 0,1 (SUM) ± 0,05 (RUM) |
| **Minimum Hole Diameter** [mm] | 0,8 | 0,3 | 0,001 | 0,1 | not available | 0,33 (SUM) 0,6 (RUM) |
| **Kerf width** [mm] | 0,8 (AWJ) 0,5 (PWJ) | 0,3 (AWJ) 0,08 (PWJ) | 0,001 | 0,1 | not available | not available |
| **Thickness Range** [mm] | 5 up to 300 | 0,01 up to 100 | 0,01 up to 2 | 0,01 up to 250 | not available | up to 170 mm |
| **Ra** [µm] | 1,6 | 0,8 | low | 1,38 | 0,17 | not available |

### 2.3.1. Advantages of water jet compared to laser machining

Nowadays, laser technology is probably the most precise and fast cutting technology as well the best choice to satisfy high production volumes when cutting relatively thin materials. Anyway, water jet technology has a number of advantages over laser technology, which are listed below:

- machining of a wider range of materials: water jet can cut a wide range of materials without requiring important changes in setup. Moreover, it can easily machine highly reflective materials that lasers cannot, such as copper and aluminum, as well as materials which are heat-sensitive;

- no heat affected zone: water jet cutting does not heat machined parts and does not change the properties of the material. As a conclusion, there is no HAZ or thermal distortion, which can occur with lasers;

- machining of thicker materials: rising up pressure and slowing down the feed rate it is possible to cut very thick parts. Water jet easily handles up to 100 mm steel, although some applications have used abrasive water jet on thicknesses up to 250 mm in steel, but with less precision and really slow feed rates. On the contrary, laser technology seems to have a maximum practical cutting thickness up to 20-25 mm depending on the material to be machined. Moreover, water jet offers better tolerances on parts thicker than 10 mm. For thinner parts, both water jet and lasers offer comparable tolerances;

- manufacturing of multilayer materials: multilayer materials are practically impossible to be cut with laser due to the different behavior of each material to laser radiation, while water jet does not have any problems in machining these products, providing a solution about the delamination;

- lower investment and maintenance cost: the cost of a water jet machine is generally much lower than the cost of a laser system. Moreover, the cost per machined part is slightly lower in case of water jet cutting. Finally, maintenance is easier and cheaper for a water jet system than for a laser;

- better edge finish and no burrs: materials cut by water jet have a fine, sand-blasted surface because of the way the material is abraded, which makes a high-quality weld easier. Particularly, thick materials cut by laser tend to have a rougher, scaly edge, which may require additional machining operations to clean up. Water jet produces less or even no burrs on the finished workpiece;

- independence from sheet-metal planarity: in laser applications, the material needs to be relatively uniform, since when cutting over uneven surfaces, the laser can lose its focus and therefore cutting power. A water jet still retains much of its cutting power over uneven material; although the material may deflect the cutting stream, it typically has a negligible effect;

- more environmental sustainability: water jet is basically a more environmentally friendly technology compared to laser.

### 2.3.2. Advantages of water jet compared to electric discharge machining

Electrical discharge machining (EDM) is used to machine electrically conductive materials by eroding the metal. A high-frequency series of electric sparks removes metal by melting and vaporizing it, while the material particles removed are flushed away by a continuously flowing non-conductive fluid, such as deionized water or kerosene. EDM can create intricate shapes in hard materials that are difficult to machine using traditional methods, satisfying very small tolerances with excellent surface finishing. The main drawback of this process is that it is really slow.
The main advantages of water jet over EDM are the following:

- abrasive water jet is much faster than EDM in metal cutting;

- machining of a wider range of materials: water jets can machine almost any material, included non-conductive materials, such as glass, wood, plastic, and ceramic;

- make its own pierce hole: in some types of EDM, such as wire-EDM, a hole needs to be first made in the material, which has to be done by a separate process. Water jet can pierce the material on its own, requiring no additional fixturing or machining;

- no heat affected zone: in water jet cutting there is no HAZ, thermal distortion or change in the properties of the material, which can occur with standard EDM;

- cutting of pieces: the size of the part created with a water jet is limited by the size of the material or the x-y table of the water jet machine, while machining big part by means of EDM is quite uncommon and time consuming;

- less setup requirement: the setup process in water jet is generally faster, while setup needs more attention in EDM, especially in operations involving complex matrices or in wire EDM.

# 3. WATER JET: FROM MACRO TO MICRO

Abrasive water jet is a non-conventional machining process characterized by extreme flexibility and versatility. Nowadays, abrasive water jets have improved their machining capability and precision being often used as an alternative of lasers, electric discharge machining (EDM) and ultrasonic machining. As a matter of fact, in many applications, abrasive water jets have better performances in terms of cost-effectiveness, short machining and turnaround times, ease of use and preservation of structural and chemical properties of parent materials. These advantages are fully analyzed in **Section 3.3**.

In the past years, considerable resources have been invested in the development of precision water jets to satisfy the high demand for low-cost micromachining components. As abrasive water jet machining is achieved by the contribution of many individual particles performing micromachining, abrasive water jets cutting could be suitable to micromachining by using small size abrasives along the nozzle to minimize the beam diameter of the jet.

In **Section 3.1** and **Section 3.2**, an industrial state of the art of conventional water jet and micro water jet are described to demonstrate the versatility of this technology.

# 3.1. The industrial state of the art of water jet technology

## 3.1.1. The state of the art of conventional abrasive water jet

Nowadays, standard abrasive water jet technology is applied both for research and industrial activities such as automotive and aerospace industry, medical applications, tool manufacturing. A summary is shown in **Table 3.1**.

**Table 3.1.:** Some peculiar features for water jet system, taken from the website of different companies.

| | **Focuser diameter** [mm] | **Cutting Area** [mm x mm] | **Positioning Accuracy** [mm] | **Repeatability** [mm] | **Transverse Speed** [m/min] |
|---|---|---|---|---|---|
| **WARICUT** HWE Series | 0,7 - 2 | 1200 x 1200 | $< \pm$ 0,02 | not available | up to 30 |
| **OMAX** 60120 | 0,7 - 2 | 3200 x 1575 | not available | $\pm$ 0,051 | not available |
| **FLOW** Mach 4c | 0,7 - 2 | 3000 x 2000 | 0,02 | 0,025 | up to 55 |
| **TECNOCUT** Milestone | 0,7 - 2 | 2000 x 1700 | not available | not available | up tp 40 |
| **BYSTRONIC** ByJet Smart | 0,7 - 2 | 3084 x 1524 | $\pm$ 0,08 | $\pm$ 0,025 | up to 60 |

For typical abrasive water jet cutting applications, the water pressure is between 200 and 600 MPa, the jet diameter is roughly between 0,7 - 2 mm, and the abrasive particle size between mesh number #80 and #200 (0,18 - 0,08 mm). The most common machines that are used for abrasive water jet applications are characterized by a positioning accuracy of 0,02 mm with a repeatability between 0,025 – 0,05 mm.

## 3.1.2. The state of the art of micro abrasive water jet

In order to make abrasive water jet technology more suitable for micro manufacturing, the first step is to minimize the jet diameter by downsizing the nozzles and the cutting-head components, which implies the reduction of the abrasive particle size as well. The reduction of the particles size calls for an increased velocity of the fluid jet (higher water pressures) in order to maintain a high erosive power. Moreover the movement of the cutting head and the switching on/off of the jet have to be more

precisely controlled. The control of the movement can be easily achieved by using more accurate handling systems. Jet on/off control, however, is more complicated as it depends on the abrasive water jet generation system. As a matter of fact, the injection system develops problems due to the delay in mixing of water and abrasive when the water jet is turned on, and the same when it is turned off. Moreover, the process of entraining abrasive becomes increasingly ineffective at jet diameters down to 500 µm and ceases to operate at jet diameters of 300 µm [20]. To overcome such criticism, experience suggests using suspension abrasive water jet where this control is almost instantaneous. This system can also achieve smaller diameters of jets (down to 50 µm), but there's a greater wear of parts, which usually have to be made in diamond.
Practical limits on how small abrasive water jet can be performed are due to:

- as nozzle diameters are decreased water flows in fluid circuits becomes laminar, rather than turbulent. At present it is not known what limitations these physical phenomena will place on minimum jet. Down to 50 µm diameter jets, the Reynolds number (ratio of inertia to viscous forces) is sufficiently high to maintain turbulent flow in critical components [3];

- to a given water pressure and abrasive concentration, the cut surface varies linearly with jet diameter, so does the thickness of material to be cut. This linear relationship is known to apply for jet diameters from 2 mm down to 200 µm but there are indication of nonlinear effects, probably due to viscosity, surface tension, particle size and other physical phenomena, by a 50 µm jet diameter [3];

Nowadays, some manufactures of abrasive water jet machines offer dedicated micro abrasive water jet systems able, on average, to reach a roughness value of about Ra = 0,8 µm (depending on material and thickness) and tolerances on parts about ± 0,01 mm.

The performances of these commercial systems are shown in **Table 3.2**.

## 3.2. Conventional water jet system and miniaturized cutting head

Water jet technology is characterized by a great versatility: it is possible to use a miniaturized cutting head with a conventional water jet system to improve its quality. The aim of this section is to evaluate the limits and the weakness points of the cutting head.
This brief investigation, carried out at Tecnalia R&I (San Sebastian, Spain) is a first comparison between machining with traditional system with conventional cutting head and with miniaturized cutting head. By definition, fine abrasive water jet is an abrasive water jet in a diameter range between 0,3 to 0,5 mm. The fine abrasive

**Table 3.2.:** Some peculiar features of water jet system for micro manufacturing, taken from the website of different companies.

| | **Focuser diameter** [mm] | **Cutting Area** [mm x mm] | **Positioning Accuracy** [mm] | **Repeatability** [mm] | **Transverse Speed** [m/min] |
|---|---|---|---|---|---|
| **Standard AWJ** | 0,7 - 2 | any | ± 0,02 | ± 0,025 - 0,05 | ~ 40 |
| **WARICUT** MicroMax | 0,2 | 750 x 750 | ± 0,01 | ± 0,005 | 20 |
| **OMAX** 2626xp | 0,38 | 737 x 635 | ± 0,02 | not available | 22 |
| **MICRO WJ** LLC AWJMM | ~ 0,3 | not available | ± 0,01 | ± 0,003 | not available |
| **FINE CUT** | 0,2 | not available | not available | not available | not available |
| **R&D Nozzle** | < 0,2 | not available | not available | not available | not available |

water jet system used for this comparison is the same used for the experimentation: it is fully presented in **Section 6.1**.
With the aim to start studying these topics, the miniaturized cutting head has the internal geometry which is equal to the half of a standard system components dimensions, the diameter of orifice is 0,15 mm and the focuser is characterized by a diameter of 0,5 mm and a length of 76,2 mm. The jet produced is then about of 0,6 mm wide and the size of the abrasive used is #200. The feed rate is 200 mm/min and the abrasive flow rate is 80 g/min.
For the conventional cutting head, the diameter of orifice is 0,35 mm and the focuser is characterized by a diameter of 0,91 mm and a length of 76,2 mm. The feed rate is 1500 mm/min and the abrasive flow rate is 350 g/min. The specimen is aluminum with a thickness of 2 mm: the special geometry is studied for this kind of comparison, with small features to underline the differences between the two cutting heads. Moreover, the cutting parameters are optimal for macro cutting head, so a comparison of the quality of the kerf, in terms of roughness, is not meaningful.
The geometry of the specimen is shown in **Figure 3.1**.

In **Table 3.3** the parameters of macro and fine abrasive water jet are presented.

With a qualitative analysis, it's clear that the miniaturized cutting head allows to achieve a better definition of the fine features, as shown in **Figure 3.2**.

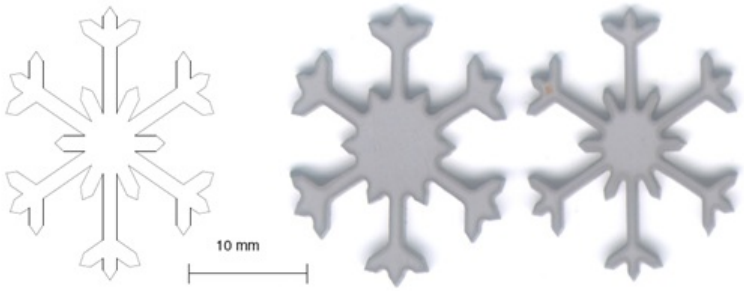


**Figure 3.1.:** The special specimen studied for the comparison between macro and miniaturized cutting head on a traditional water jet system

**Table 3.3.:** Parameters of macro AWJ and fine AWJ used for the comparison.

| Parameters | Macro AWJ | Fine AWJ |
|---|---|---|
| orifice diameter [mm] | 0,35 | 0,15 |
| focuser diameter [mm] | 0,91 | 0,50 |
| focuser length [mm] | 76,2 | 76,2 |
| kind of abrasive | Garnet#80 | Garnet#200 |
| abrasive flow rate [g/min] | 350 | 150 |
| pressure [MPa] | 200 | 200 |
| feed rate [mm/min] | 1500 | 500 |

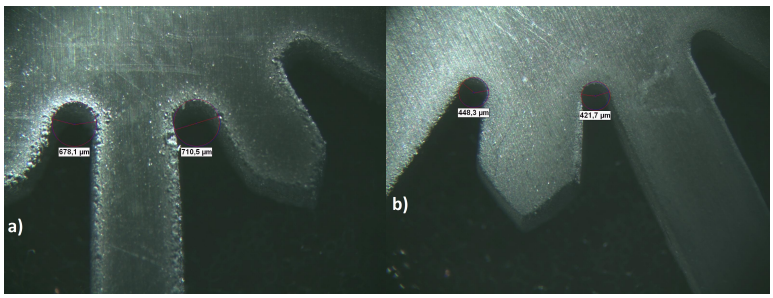


**Figure 3.2.:** The minimum radius with conventional cutting head is around 700 µm, while with miniaturized cutting head is around 430 µm.

## 3.3. Applications of fine water jet

A key characteristic of the current "industrial revolution" is the miniaturization of products and processes. Device and component manufacturers require smaller and smaller features to be machined, with increasingly tighter tolerances, on a growing

range of difficult-to-machine materials. The need to fabricate micro scale systems for different purposes in the fields of engineering, medicine, energy, robotics and informatics has encouraged the development of new manufacturing processes capable to machine properly miniaturized geometric features.
These features must offer different functionalities to the integration of mechanical and electronic elements, sensors, actuators, pumps and other micro systems used in different application such as optical switches, micro conveyors, micro fluidic devices, micro turbines, micro cantilevers, and so on. Furthermore, there has been a considerable demand for a cost-effective and fast turnaround machine tool for various industrial applications from art and craft, jewel and watch making, to semiconductor singulation.
Anyway, applications where micro abrasive water jet can be more appropriate and profitable than any other technology regard the fields of non-conventional materials which are typically hard to machine with other technologies; among the others, ceramics and piezoelectric materials, composites and compound materials like fiber reinforced plastics, metal matrix composites and sandwich materials. Single crystalline materials like silicon and sapphire can be cut as well.
In addition, due to the miniaturization of kerf, the fine abrasive water jet process produces very little scrap and this is profitable in case of machining very expensive materials such as copper, titanium, inconel, gold, silver, platinum and so on.
A complete summary is shown in **Table 3.4**. In **Figure 3.3** ([21]) different materials machined by micro abrasive water jet are shown.

**Table 3.4.:** A complete summary of the materials that can be cut with water jet.

| **ALLUMINIUM / NON FERROUS METALS** | | |
|---|---|---|
| Aluminium and alloy | Bronze | Copper and alloy |
| Aluminium cast materials | Brass | |
| **SOFT MATERIALS** | | |
| Soft foam | Wood | Leather |
| Hard foam | Paper | |
| **GLASS** | | |
| Bullet proof glass | VSG | Mirror |
| Glass | | |
| **PLASTICS** | | |
| Thermoplastic | Graphite | Elastomer |
| Curable plastic | | |
| **OTHER MATERIALS** | | |
| Sandwich materials | Composites | Perfored sheets |
| Structured materials | Piezoelectric | Layered materials |

The former applications are mainly potential, since up to now, they still have not

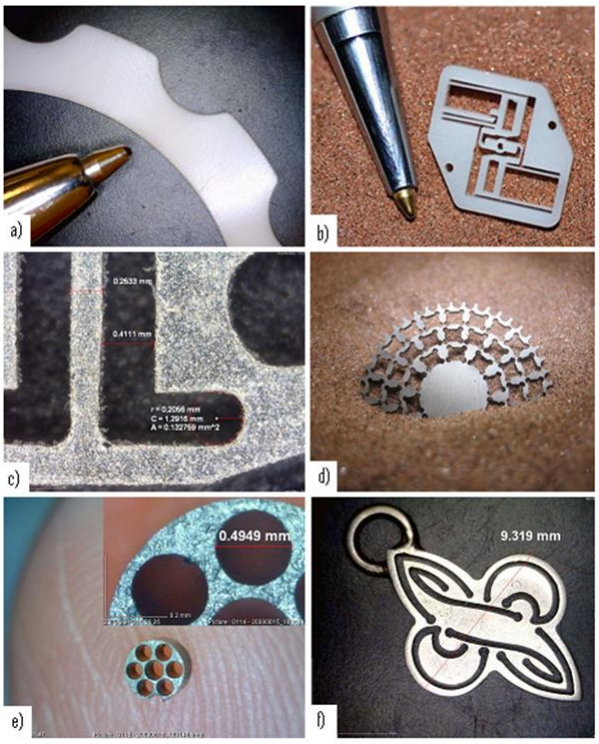


**Figure 3.3.:** Some micro features machining with micro water jet of different materials: a) Teflon; b) Delrin; c) Carbon steel; d) Stainless steel; e) Nitinol; f) Sterling silver

been industrializd. With the advent of research and development in micro / nano technology, industrial and consumer products derived from this technology are expected to become commercially available in 5 to 10 years.
In literature, there are a lot of examples of samples machined by fine water jet, underling the feasibility of this process.
In [5], the authors suggest an alternative process chain consisting in producing the electrode for MEDM with micro abrasive water jet: the final tool has to be used for replication processes and is produced by MEDM, as shown in **Figure 3.4**.

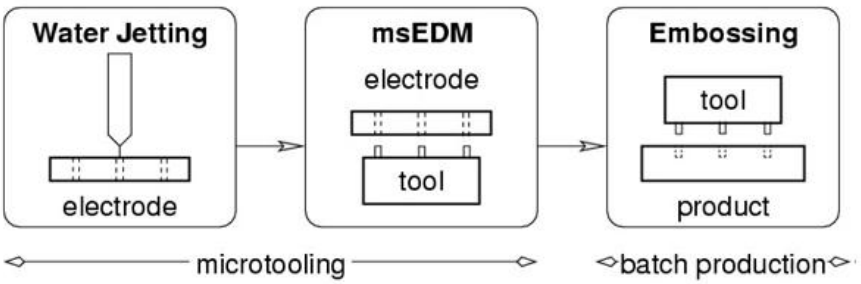


**Figure 3.4.:** Process chain for micro-tool manufacturing.

In [4], the author investigates the same application, delving into the specific aspects of the process: the first results are very promising and the proposed tooling strategy, which involves water jet technology besides MEDM, shows a lot of potential notably in the design and developing phase of micro-fluidic devices. **Figure 3.5** shows his investigation.

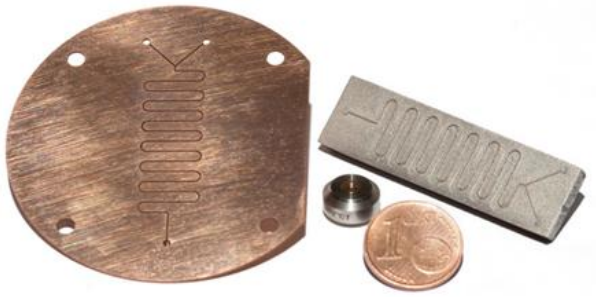

**Figure 3.5.:** Copper electrode sheet machined by WJ, 80 µm WJ nozzle and the final tool produced by MEDM.

In [20], D.Miller presents profiling and drilling studies directed to demonstrating the capability of micro abrasive water jet and to the development of components and systems, as shown in Figure **3.6-3.7-3.8**.

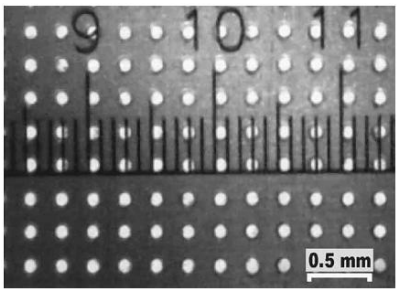


**Figure 3.6.:** Eighty-five micron diameter holes on 250 µm pitch through 50 µm stainless steel.

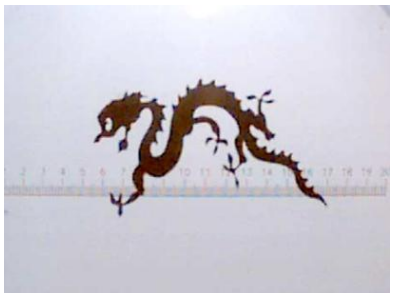

**Figure 3.7.:** Profile from 50 µm thick stainless steel, cut with 300 nm abrasive.

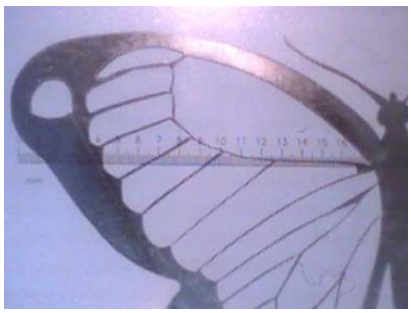

**Figure 3.8.:** An example of profiling with thin sections (smallest division 100 µm)

In [22] the authors make a comparison between microend milling, wire EDM/sandblasting and micro abrasive water jet: their capabilities are compared with lithography capabilities, which is the conventional process for microchannel manufacturing, as shown in **Figure 3.9**. Micro abrasive water jet doesn't compete with lithography in terms of achieving acceptable levels of product quality, but shows superior productivity.

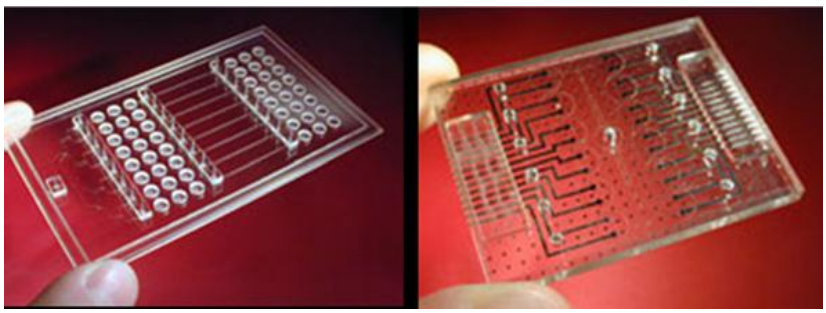

**Figure 3.9.:** Microfluidic devices for biological analysis, fabricated by Epigem

Professional market research has indicated that market conditions appear favourable for advanced micromachining technology due to the fact that medical devices are continually becoming smaller and more intricate in terms of size, shape, and material.
In [23], the authors report a comparison between water jet and micro machining on the machining of small structures into binary NiTi sheets, which are used for a variety of applications including medical implants and tools as well as actuators, as shown in **Figure 3.10**.
Another example of medical application (**Figure 3.11**) is presented by Miller in [24]: the author upholds that the heart patch reinforcement machined by micro abrasive water jet will be commercially available for one year.

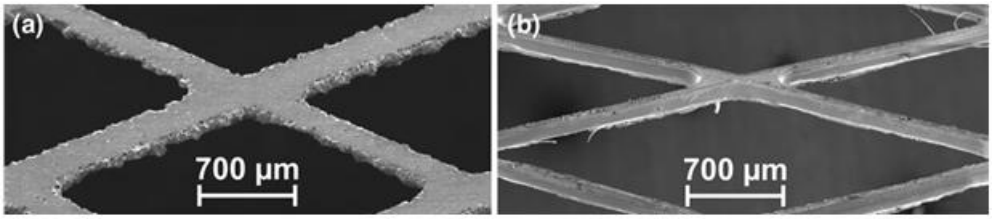


**Figure 3.10.:** Upper side of a stent-like structure machined by (a) pure water jet and (b) by micro milling

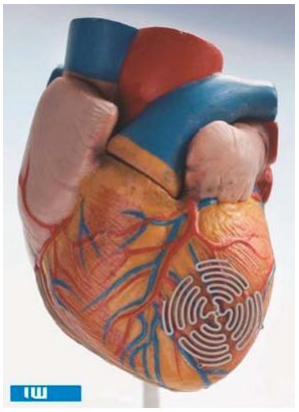

**Figure 3.11.:** Heart patch Reinforcement (Institute Material Science – University Hannover

Miniplates and microplates for orthopedic implants (**Figure 3.12**) to repair/reconstruct bone and skull fractures are one of the strong candidates to take full advantage (scalability, setup simplicity and no tooling requirement) of micro abrasive water jet technology. Titanium is used most often for these plates because of its biocompatibility. While conventional machine tools have difficulty in machining titanium, abrasive water jets cut it quickly at considerably low costs [25].

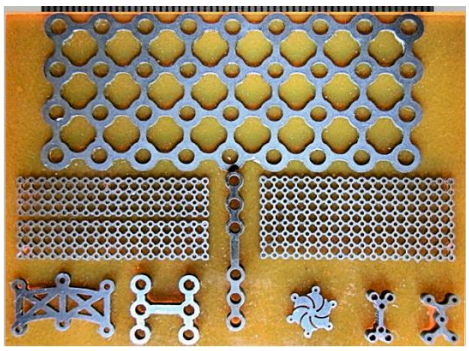

**Figure 3.12.:** AWJ-machined orthopaedic components – scale in mm

A study for feasibility of a piezoelectric ceramic machining is carried out at Dipartimento di Meccanica of Politecnico di Milano in close cooperation with Dipartimento di Ingegneria Meccanica Nucleare e della Produzione of Università di Pisa.
The piezoelectric ceramic is lead zirconate titanate $Pb(Zr_{0.54}Ti_{0.46})O_3$, also called PZT, a ceramic perovskite material that shows a marked piezoelectric effect. PZT-based compounds are composed of the chemical elements lead and zirconium and the chemical compound titanate which are combined under extremely high temperatures.
This piezoelectric ceramic is used as micro actuators (**Figure 3.13**), the case study of this work. In this field of application is very important not to have heat affected zone which reduces the section of piezoelectric materials, so micro water jet is a very appealing technology. Moreover, in behalf of water jet technology, there is a high feed rate, although the roughness reachable with other technologies such as laser and diamond disc is better ($R_a$ =2,1 µm for water jet, $R_a$ = 1,8 µm for lasers and $R_a$ = 0,26 for diamond disc).
This investigation is deepened in **Section 5.3**, describing the feasibility experiments, aimed to optimizing cutting parameters.

**Figure 3.13.:** The 2-degree-of-freedom actuators developed by Dipartimento di Ingegneria Nucleare, Università di Pisa

This material is also used in microfludic devices (**Figure 3.14**), as shown in [26].

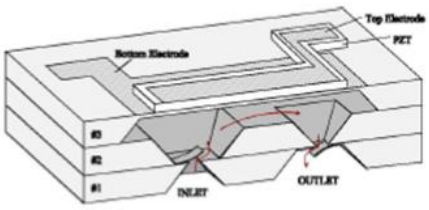


**Figure 3.14.:** In this picture is shown a PZT pump.

# 4. PIEZOCERAMICS: PROPERTIES AND APPLICATIONS

Advanced ceramics have been increasingly applied in the optical, electronic, mechanical and biological industries due to their inherent high temperature strength, hardness, corrosion resistance and electromagnetic response. While the limits of traditional mechanical cutting methods are being approached, the cutting performance is also becoming more demanding in terms of speed and accuracy. In such field abrasive water jet cutting technology offers many advantages when compared to many traditional and other non-traditional machining technologies: no thermal distortion, high flexibility, high machining versatility and small machining force [27].
In this section a brief introduction about piezoelectric materials and piezoelectric actuators is presented; then the material removal mechanism of piezoceramics with abrasive water jet is analyzed.

## 4.1. Piezoelectric materials

The piezoelectric ceramics are some particular ceramic materials which are characterized by a close correlation between their electrical and mechanical behaviour. This property was discovered by the Curie brothers in 1880 and has found applications in many fields of science and technology.
Ferroelectricity is a subgroup of piezoelectricity, where a spontaneous polarization exists that can be reoriented by application of an AC electric field. Piezoelectric ceramics are ferroelectric materials characterized by electric and mechanical properties, which are strictly correlated.

The **Figure 4.1** shows a brief scheme about piezoelectric materials.

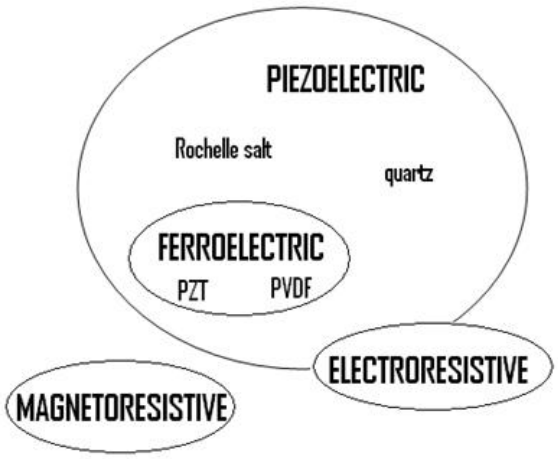


**Figure 4.1.:** A scheme of the main family of electro-sensible materials.

If a piezoelectric material is subjected to a mechanical strain, an electrical polarization will appear within it: this effect is called direct piezoelectric effect, as shown in **Figure 4.2** ([26])and **Figure 4.3** [28]. On the contrary, if the material is exposed to an external electric field, it reacts with a mechanical deformation: this is called inverse piezoelectric effect. Therefore, these materials are used to convert electric in mechanical energy and vice versa and thanks to their properties are perfect to be employed as actuators or sensors.
The microscopic origin of the piezoelectric effect is the displacement of ionic charges within a crystal structure. In the absence of external strain, the charge distribution within the crystal is symmetric and the net electric dipole moment is zero. However when an external stress is applied, the charges are displaced and the charge distribution is no longer symmetric.

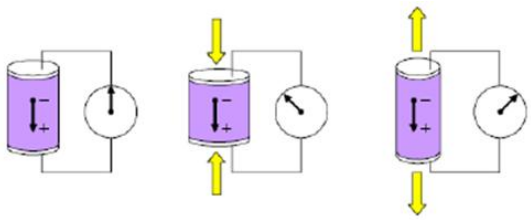

**Figure 4.2.:** A scheme of the direct piezoelectric effect.

Some materials show naturally a piezoelectric behaviour such as quartz, topaz, and tourmaline; while nowadays the most used piezoelectric materials are artificially

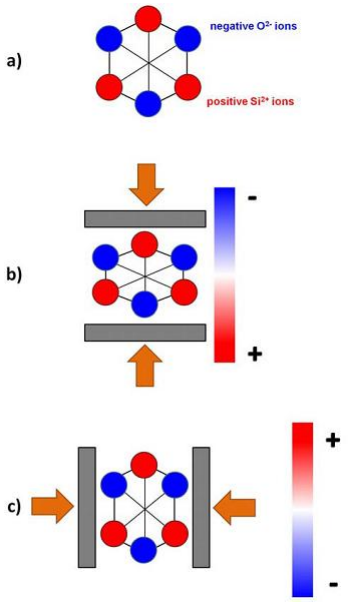


**Figure 4.3.:** Graphical representation of the direct piezoelectric effect, in case of a single cell of quartz crystal; (a) undeformed cell, with no electric polarization; (b) longitudinal piezoelectric effect: the polarization arises in the same direction of the external load; (c) transverse piezoelectric effect: the polarization is normal to the load axis.

made, as quartz analogical crystals, ceramics Perovskit structures (such as polycrystalline piezoceramics, that are described deeply in **Section 4.1.1**) and special polymers (such as polyvinylidene fluoride, which has not a crystalline structure).

### 4.1.1. Polycrystalline piezoceramics

The crystalline structure influences the piezoelectric properties. The original crystalline structure is composed by an elementary cubic cell with a central atom of titan or zirconium, as shown in **Figure 4.4** ([29]).

The first piezoelectric ceramic with piezoelectric properties that has been discovered was the barium titanate ($BaTiO_3$). Nowadays, the most commonly used piezoelectric materials are the lead titanate ($PbTiO_3$) and the lead zirconate titanate, also called PZT ($Pb[Zr_xTi_{1-x}]O_3$). All these materials have a particular crystalline structure, called Perovskit tetragonal structure: each elementary cell of the crystal has an asymmetric structure, with a single positive ion constrained in a non-centred position: this fact causes a dipole moment PS along the direction of the cell's major extension, as shown in **Figure 4.5**.

If the cell is subjected to external electric field or a mechanical strength, an additional polarization effect is induced, causing an additional displacement of ions that

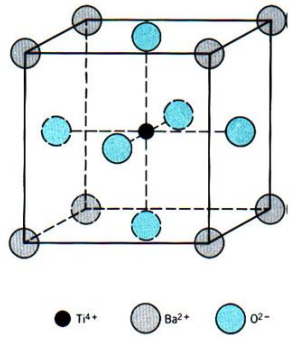


**Figure 4.4.:** The picture shows the crystalline structure of barium titanate ($BaTiO_3$).

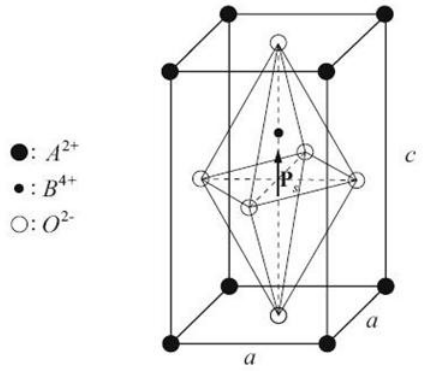


**Figure 4.5.:** Perovskit tetragonal structure of a PZT crystal

determinate a deformation of the crystal. All these characteristics are manifested only below a Curie temperature (Tc): above Tc, the crystalline structure becomes cubic and symmetric, losing all piezoelectric properties (forever, even when temperature returns below Tc) and acquiring a paraelectric behaviour.
Polarization consists in the orientation of the electric dipoles in the material, as shown in **Figure 4.6**:
1. the material is worm up to Tc;
2. an electric field is applied in order to align all the domains of polarization;
3. the orientation of the domains is stopped with the cooling-off period and it hangs when the electric field is removed.

Usually, the piezoceramic structures used in mechanical applications are not a single crystal, but they have a polycrystalline structure formed by various grains. In general, the polarization of grains in a polycrystalline body is statistically distributed in all directions: therefore, the global polarization is zero. However, by adopting special expedients during the production process, it is possible to induce individual crystals to partially align their polarization direction, obtaining pieces with a certain global polarization.

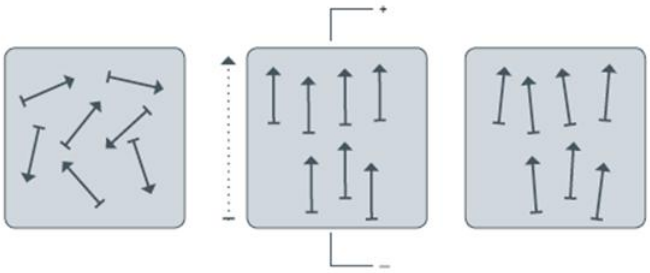

**Figure 4.6.:** Electric dipoles in piezoelectric materials before, during and after poling .

The great diffusion of PZT is primarily due to the low manufacturing cost, the relatively high TC, and a high efficiency in the electrical to mechanical transformation (and vice versa). On the other hand, its toxicity can cause environmental problems, and depolarization, caused by ageing of material.

### 4.1.2. Linear theory of piezoelectricity

Generally, ferroelectric materials are characterized by the existence of the P-E loop (**Figure 4.7** [30]).

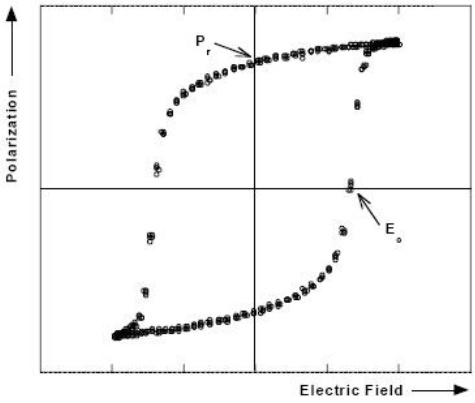


**Figure 4.7.:** Hysteresis loop of a poled piezoelectric ceramic.

In addition to the P-E loop, a polarization switch leads to strain-electric field hysteresis: a typical strain-field response curve is shown in **Figure 4.8** ([30]). The shape resembles that of a butterfly, and it is often referred to as the "butterfly loop". As the electric field is applied, the converse piezoelectric effect dictates that a strain results. As the field is increased, the strain is no longer linear with the field as domain walls start switching.

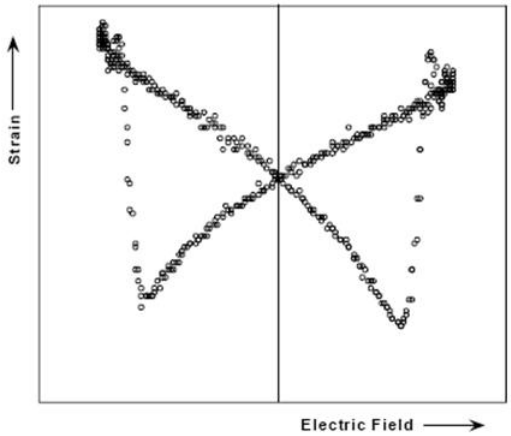


**Figure 4.8.:** Tyipical PZT butterfly loop; over a value of tension, piezoelectric material change the direction of deformation.

For high value of applied electric field, the relationship between the electric field and the polarization is non-linear and the polarization doesn't reset to zero when the electric field is removed. On the contrary, for low value of applied electric field, the residual polarization is very low and the piezoelectric ceramic response is linear, as shown in **Figure 4.9** ([26]).

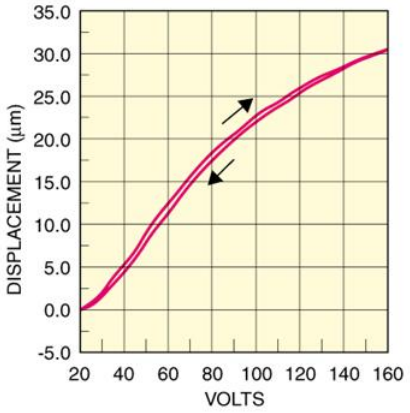


**Figure 4.9.:** The variation of strain caused by hysteresis is minimal for low value of applied electric field.

The simplest mathematical description of the piezoelectric effect is the linear theory of piezoelectricity: it's possible to read an extensive discussion about these topics in [28].
Piezoelectricity is the combined effect of electrical behaviour of the material and Hooke's Law.

$$D = P \cdot E \tag{4.1}$$

where D is the electric charge density displacement, P is the permittivity and E is the electric field strength.

$$\varepsilon = C \cdot \sigma \tag{4.2}$$

where ε is the strain, C is compliance and σ is stress.
These may be combined into so-called coupled equations, of which the strain-charge form is:

$$\begin{cases} \{\varepsilon\} = [C]\{\sigma\} + \left[M^T\right]\{E\} \\ \{D\} = [M]\{\sigma\} + [P]\{E\} \end{cases} \tag{4.3}$$

where the first equation represents the relationship for the converse piezoelectric effect and the latter for the direct piezoelectric effect.
Due to the intrinsic symmetries of the crystal the constitutive model of the PZT is quite simple and requires only 5 elastic constants, 2 permittivity constants and 3 piezoelectric coefficients, provided that the Cartesian axes of the reference system are oriented along the principal directions of the crystalline structure, as shown in **Figure 4.10**.

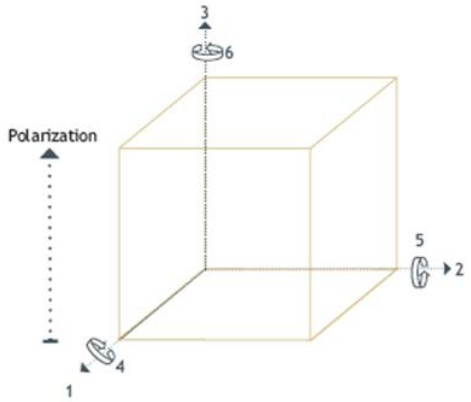


**Figure 4.10.:** Designation of axis in piezoelectric material.

The reference axis, called axis 3, is taken parallel to the polarizing direction. Axis 1 and 2 are defined arbitrarily in order to form a cartesian coordinate system with axis 3. 4, 5 and 6 represent shear movements around axes 1,2 and 3 respectively. In this case, the compliance matrix C (which contains the coefficients relating stresses to

strains), the permittivity matrix P (which contains the relationship between electric field and electric displacement into the body) and the piezoelectric coefficient matrix M (which contains the relationship between mechanical variables and electrical variables) can be expressed as follows:

$$C = \begin{bmatrix} \frac{1}{E_x} & -\frac{\nu_{xy}}{E_x} & -\frac{\nu_{xz}}{E_z} & 0 & 0 & 0 \\ -\frac{\nu_{xy}}{E_x} & \frac{1}{E_x} & -\frac{\nu_{xz}}{E_z} & 0 & 0 & 0 \\ -\frac{\nu_{xz}}{E_z} & -\frac{\nu_{xz}}{E_z} & \frac{1}{E_z} & 0 & 0 & 0 \\ 0 & 0 & 0 & \frac{1}{G_{yz}} & 0 & 0 \\ 0 & 0 & 0 & 0 & \frac{1}{G_{yz}} & 0 \\ 0 & 0 & 0 & 0 & 0 & 2\left(\frac{1+\nu_{xy}}{E_x}\right) \end{bmatrix}$$

$$P = \begin{bmatrix} g_{11} & 0 & 0 \\ 0 & g_{11} & 0 \\ 0 & 0 & g_{33} \end{bmatrix}$$

$$M = \begin{bmatrix} 0 & 0 & 0 & 0 & d_{15} & 0 \\ 0 & 0 & 0 & d_{15} & 0 & 0 \\ d_{31} & d_{31} & d_{33} & 0 & 0 & 0 \end{bmatrix}$$

A complete summary is shown in **Table 4.1**.

**Table 4.1.:** A summary of the mechanical and electric properties of lead zirconate titanate ceramic (PZT ceramic)

| data | unite of measurement | Lead Zirconate Titanate | |
|---|---|---|---|
| **MECHANICAL PROPERTIES** | | | |
| $\rho$ | $kg/m^3$ | 7800 | $\frac{mass}{volume}$ |
| $E_x$ | $MPa$ | $66 \cdot 10^3$ | $\frac{stress}{strain}$ |
| $E_z$ | $MPa$ | $52 \cdot 10^3$ | $\frac{stress}{strain}$ |
| $G_{yz}$ | $MPa$ | $21 \cdot 10^3$ | $\frac{stress}{strain}$ |
| $\nu_{xy}$ | - | $0,35$ | $\frac{strain\,x}{strain\,y}$ |
| $\nu_{xz}$ | - | $0,38$ | $\frac{strain\,x}{strain\,z}$ |
| **PIEZOELECTRIC VOLTAGE CONSTANTS** | | | |
| $d_{31}$ | $m/V$ | $-1,9 \cdot 10^{-10}$ | $\frac{strain\,developed}{applied\,field}$ |
| $d_{33}$ | $m/V$ | $3,9 \cdot 10^{-10}$ | $\frac{strain\,developed}{applied\,field}$ |
| $d_{15}$ | $m/V$ | $5,9 \cdot 10^{-10}$ | $\frac{strain\,developed}{applied\,field}$ |
| **PIEZOELECTRIC VOLTAGE CONSTANTS** | | | |
| $g_{11}$ | $V \cdot m/N$ | $-1,2 \cdot 10^{-2}$ | $\frac{open\,circuit\,field}{applied\,stress}$ |
| $g_{15}$ | $V \cdot m/N$ | $2,4 \cdot 10^{-2}$ | $\frac{open\,circuit\,field}{applied\,stress}$ |
| **COUPLING COEFFICIENT** | | | |
| $k_{11}$ | – | $0,72$ | $\frac{permettivity\,of\,material}{permettivity\,of\,space}$ |
| $k_{33}$ | – | $0,35$ | $\frac{permettivity\,of\,material}{permettivity\,of\,space}$ |
| **THERMAL PROPERTIES** | | | |
| $T_C$ | ° C | 350 | $Curie's\,temperature$ |

### 4.1.3. Soft and hard piezoceramics

Piezoelectric ceramics are perovskite varieties in which the linear piezoelectric response dominates. At low electric fields, piezoelectric ceramics are well described by the linear piezoelectric equations. When classifying piezoceramics according to their coercive field during field-induced strain actuation, two main categories emerge: if the coercive field is large (approximately greater than 1 kV/mm) the piezoceramic is hard, while if the coercive field is moderate (between 0,1 and 1 kV/mm) the piezoceramic is classified as soft. A hard piezoceramic shows an extensive linear drive region, but a relatively small strain magnitude; a soft piezoceramic shows a large field induced strain, but relatively large hysteresis. The hard and soft behaviour is also related to the Curie temperature: hard piezoceramics tend to have a higher Curie point, 250º<TC, whereas soft piezoceramics have a moderate Curie point, 150º<TC<250ºC.
Hard piezoelectric materials can be subjected to high electrical and mechanical stresses. Their properties change only little under these conditions and this makes them particularly ideal for high-power applications (high d33 constant). Many new applications often require not only a high stroke, but sometimes that they should

work at high temperature, e.g. in fuel injection up to 200 °C, or should work at high frequency without significant heat generation, e.g. in ultrasonic motors operating at 20 – 30 kHz [30].
The advantages of these PZT materials are the moderate permittivity, large piezoelectric coupling factors, high qualities and very good stability under high mechanical loads and operating fields. Low dielectric losses facilitate their continuous use in resonance mode with only low intrinsic warming of the component. These piezo elements are used for example in ultrasonic cleaning (typically kHz frequency range), in the machining of materials (ultrasonic welding, bonding and drilling), for ultrasonic processors, in the medical field (ultrasonic tartar removal and surgical instruments) and also in sonar technology.
Several PZT formulation are commercially available, as shown in **Table 4.2** (data are taken from American Piezo Ceramics, Inc).

**Table 4.2.:** Table of mechanical and electric characteristic of different piezoelectric materials: in the red column the soft piezoelectric used in this experimentation, in the blue column a hard piezoelectric

| **properties** | **APC 840** | **APC 841** | **APC 850** | **APC 855** | **APC 856** | **APC 880** |
|---|---|---|---|---|---|---|
| $\rho[kg/m^3]$ | 7600 | 7600 | **7700** | **7500** | 7500 | 7500 |
| $d_{31}[\cdot 10^{-12} m/V]$ | -125 | 109 | **-175** | **270** | 260 | -95 |
| $d_{33}[\cdot 10^{-12} m/V]$ | 290 | 275 | **400** | **580** | 620 | 215 |
| $d_{15}[\cdot 10^{-12} m/V]$ | 480 | 450 | **590** | **720** | 710 | 330 |
| $g_{11}[\cdot 10^{-3} Vm/N]$ | -11 | 10,5 | **-12,4** | **8,8** | 8,1 | -10 |
| $g_{15}[\cdot 10^{-3} Vm/N]$ | 26,5 | 25,5 | **26** | **19,5** | 18,5 | 25 |
| $k_{11}[-]$ | 0,72 | 0,68 | **0,72** | **0,74** | 0,73 | 0,62 |
| $k_{33}[-]$ | 0,35 | 0,33 | **0,36** | **0,38** | 0,36 | 0,30 |
| $E_x[GPa]$ | 80 | 76 | **63** | **61** | 58 | 90 |
| $E_z[GPa]$ | 68 | 63 | **54** | **48** | 45 | 72 |
| $T_C$[°C] | 325 | 320 | **360** | **195** | 150 | 310 |
| $Q_M[-]$ | 500 | 1400 | **80** | **75** | 75 | 1000 |

Hard piezoelectric materials have better properties than soft piezoelectric materials, but they are usually much more difficult to machine: in fact, significant changes in their piezoelectric properties starts at around 100°C and their Curie temperature is relatively low, around 150°C. Because of this reason, thermal processes such as laser or EDM machining are not suitable (see **Section 4.3**), while water jet represents a perfect alternative technology able to machine hard piezoelectric materials without altering thermally or chemically the materials often used in the field of micro applications.

## 4.2. Piezoceramic actuators

Nowadays, there are lots of industrial applications for piezoelectric materials. The fields of applications are mainly three: as electric power sources, as sensors and as actuators.
As electric power sources, it is possible to induce in a piezoelectric body a very large voltage through the application of a force (the direct piezoelectric effect is used). This principle is frequently used to generate a single electric discharge, for example in cigarette lighters and other ignition systems, as shown in **Figure 4.11**.

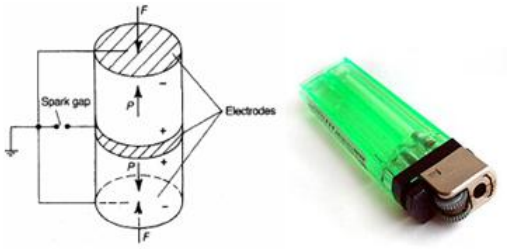


**Figure 4.11.:** The typical application of piezoelectric ceramic as electric power source is in cigarette lighters.

As sensors and transducers, there are also many applications, thanks to the capability of piezoelectric materials of transforming mechanical stimuli in electric signals: as instance they are employed to make force transducers, microphones and microbalances and also in industrial nondestructive testing. Detection of pressure variation in the form of sound is the most common sensor application, for example in piezoelectric microphones, where sound waves bend the piezoelectric material, changing voltage, and piezoelectric pickups for acoustic-electric guitars, as shown in **Figure 4.12**.

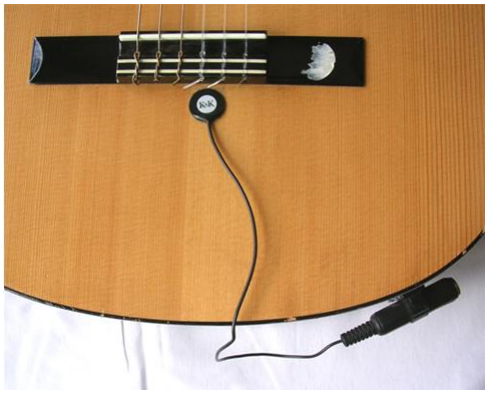

**Figure 4.12.:** Piezoelectric disk used as guitar pickup.

For many sensing techniques, the sensors can act as both sensors and actuators, so they are called transducers. Ultrasonic transducers, for example, can inject ultrasound waves into the body, receive the returned wave, and convert it to an electrical signal (typically a voltage). An example of ultrasonic transducers is shown in **Figure 4.13**.


**Figure 4.13.:** An ultrasound probe for nondestructive testing: the probe uses a piezoelectric crystal to send out ultra-sounding signals.

The final applications of piezoelectric ceramics are the piezoelectric actuators. There's a growing demand for actuators with a micro-scale design. This need has been reported across the micro-robotics industry and the most recent medical applications. Despite such different fields of use, the core characteristics required by millimeter and sub-millimetre scales actuators are basically the same: actuators at these scales are widely used in smart structure applications due to their high bandwidth, high output force, compact size, low response times, a simple design and simple operation [15].
For example, they can be used to move optical elements into microscopes and similar instruments. Such reasons make them very appealing for mobile micro-robotic applications such as the "Micromechanical Flying Insect" where smart structures capable of both actuating and sensing are preferred because of strict size/weight constraints [31].
In this section the cutting of piezoelectric actuators by means of abrasive water jet technology is presented as final application and case-study. Piezoelectric actuators are based on the inverse piezoelectric effect, such as piezoelectric sensors and transducers: an external voltage is applied causing a displacement. Since very high electric fields correspond only to little changes in the crystal dimensions, these can be changed with better-than-µm precision: this makes piezocrystals the most important tool for positioning objects with extreme accuracy, high force capability, and no gears (or any other mechanical transmissions).
There are three principal typologies of piezoelectric actuators: direct actuators, amplified actuators, and dynamic actuators (or piezoelectric motors).

### Direct actuators

In a direct actuator, the extension or contraction of a piezoelectric body is directly transmitted to the active surface: for this reason, direct actuators are characterized by a very small stroke (in general, some tenths of microns), but they can move a relatively high mass with a better-than-micrometer precision. They are used in medical applications, in laser mirror alignment, in atomic force microscopy and in other high-precision technology applications. An example of direct actuators is shown in **Figure 4.14**.

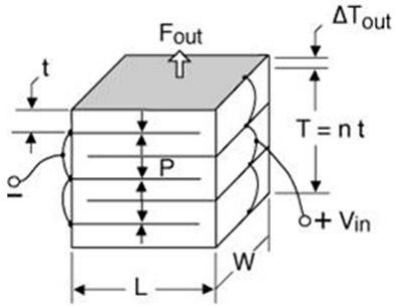


**Figure 4.14.:** Constructive diagram of a stack linear actuator.

### Amplified actuators

In an amplified actuator, the small deformation of the piezoelectric body is transmitted to a mechanical system (often a passive elastic element) to amplify it. These actuators can reach a stroke of some millimeters. The most classical design of amplified piezoelectric actuators is the bending beam actuators, as shown in **Figure 4.15**. They consist of one active piezoceramic layer and one passive elastic layer (usually made of steel). One of the edges is fully constrained, while the other is kept free to move. When an external voltage is applied, the active layer tends to expand or contract, but this motion is constrained by the other layer: the consequence is the arising of a flexional deformation.

The essential advantage of the beam bending actuators is the fact that a voltage which will be capable to induce a micrometric extension in the piezoelectric layer can provoke a large displacement (even some millimeters) by inlfecting the system's free edge.

### Dynamic actuators

In dynamic actuators, the piezoelectric body is subjected to a controlled vibration in order to transmit a motion to another object. These systems are also called

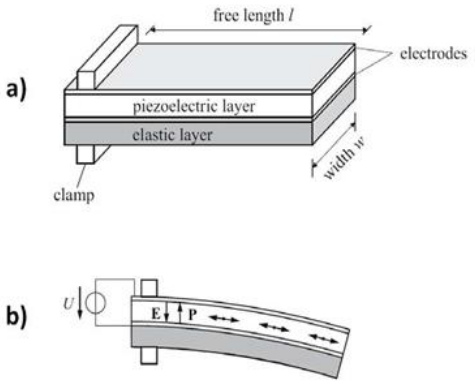


**Figure 4.15.:** Monomorph bending beam actuator; (a) general design; (b) deformed shape when an external voltage is applied.

piezoelectric motors: an example is shown in **Figure 4.16**. Depending on their design, they can perform either rotational motions or translational motions,. A great variety of solutions has been conceived, but as first approximation we can distinguish three types of dynamic piezoelectric actuators: stick-slip motors, traveling-wave motors and elliptical path motors.

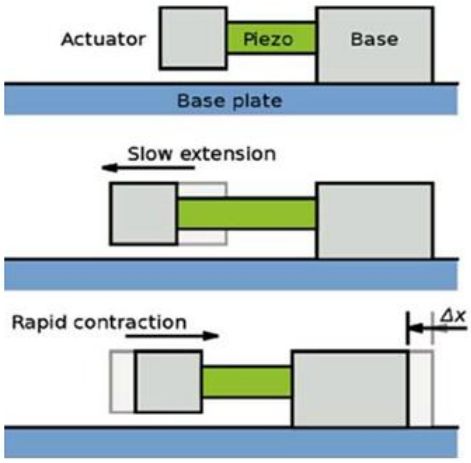


**Figure 4.16.:** Stick-slip piezoelectric motor.

All these motors, except the stepping stick-slip motor, work on the same principle. Driven by dual orthogonal vibration modes with a phase difference of 90°, the contact point between two surfaces vibrates in an elliptical path, producing a frictional force between the surfaces. Usually, one surface is fixed causing the other to move. In most piezoelectric motors the piezoelectric crystal is excited by a sine wave signal at the resonant frequency of the motor. Using the resonance effect, a much lower voltage can be used to produce high vibration amplitude. Stick-slip motor works

using the inertia of a mass and the friction of a clamp: such motors can be very small.

## 4.3. The key study: the bending actuators

The study of a machining process capable to cut piezoelectric ceramics heads towards the new demands: the key study is a micro actuator developed by Universita' di Pisa.

### 4.3.1. General description

The device called S-bender, developed by Università di Pisa, is a piezoelectric linear motor, has only one degree of freedom. It is based on the S-bending motion, whose main principles will be pointed out in this section.
The S-bender actuator is composed by the following parts, as shown in **Figure 4.17** ([28]):

a) an active layer made of lead zircon titanate (or PZT) whose properties are illustrated in **Section 4.1** and two electrodes with negligible thickness which are deposed on the upper surface of the PZT, in order to excite the two halves of the beam with two different voltages;

b) a passive layer made of high-strength steel (AISI 304) symmetrically divided in two parts, in order to avoid any electrical coupling between the two halves of the system;

c) a rigid base made of steel, covered with a dielectric paint;

d) a hemisphere made of synthetic zircon which acts as contact between the actuated surface.

The PZT is glued to the steel layer, and the hemisphere is glued to the PZT. The four metal protrusions that connect the steel layer to the base are glued with cyanoacrylate (a vitreous polymer) to the base as well.

### 4.3.2. Functioning principles

An external voltage, applied through the electrodes, causes a longitudinal deformation in the PZT layer. The direction of deformation, that is an elongation or a contraction, depends on the voltage sign. However, due to the opposition of the passive steel layer, a flexional deformation arises in the system.
When the same external voltage is applied to the PZT layer with a symmetric input, the actuator reacts with a "U-bending" (**Figure 4.18-a**). On the contrary, if the

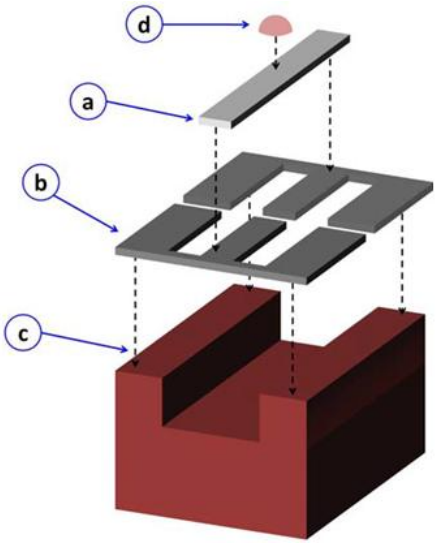


**Figure 4.17.:** General architecture of the S-bender; (a) PZT layer, (b) steel layer, (c) rigid base, (d) zircon hemisphere.

voltage applied to the left half has the opposite sign to the voltage applied to the right half (antisymmetric input) the actuator warps is a "S-bending" shape (**Figure 4.18-b**).

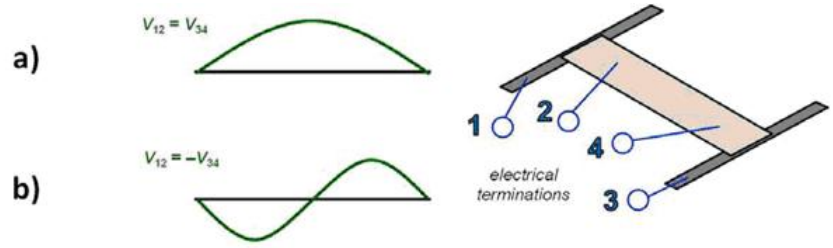


**Figure 4.18.:** U-bending (a) and S-bending (b) deformed shapes.

Unlike the U-bending deformation, the S-bending deformation causes a rotation of the zircon hemisphere. As a consequence of this, the contact point between the actuator and a hypothetical target surface is subjected to a small translation. This is the principle used as the basis for a stick-slip actuation, as shown in **Figure 4.19** ([28]): by exciting the device with a saw-tooth voltage at high frequency, we can transmit a great number of micro-displacements to the target each second. The result, from a practical point of view, is that the actuator imposes a speed to the target.

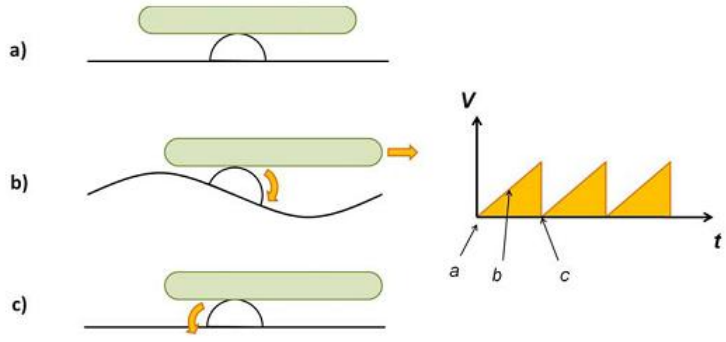


**Figure 4.19.:** Stick-slip control of the S-bender actuator; (a) starting condition, (b) stick condition, (c) slip condition.

However, another type of actuation is possible, using both U-bending and S-bending deformation (**Figure 4.20** [15]). A sinusoidal symmetric voltage compels the system to vibrate with a U-bending deformed shape, while a sinusoidal antisymmetric voltage forces an S-bending vibration. If the two different inputs are applied together with a 90° phase difference, the overlapping of the two motions causes the contact point to move along an elliptical path (**Figure 4.21** [15]).

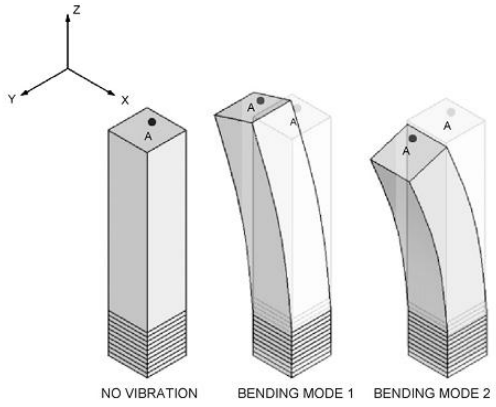


**Figure 4.20.:** Orthogonal bending modes excited during the operation of a bending mode actuators.

In this way, the actuator can apply micro-pushes to the target without have recourse to the stick-slip principle, which is characterized by a low reliability and high energy losses. The amplitude of the system's vibration can be strongly increased if the input frequency is close to a resonant frequency of the actuator which has the same profile of the desired deformed shape.
The first eigenmode of the system has approximately the same shape shown in **Figure 4.18-a**, while the second eigenmode has a shape similar to the one in **Figure**

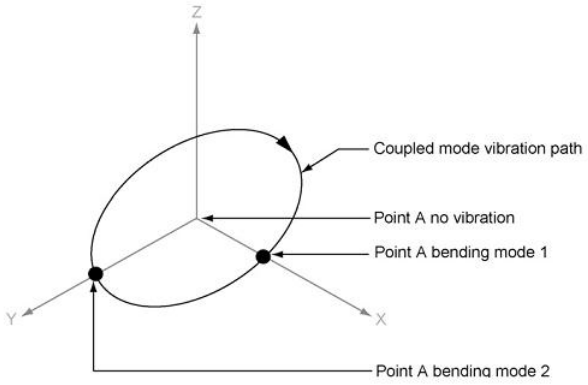


**Figure 4.21.:** The theoretical trace of a bending mode actuator for one period: the elliptical motion is achieved by coupling orthogonal first-order bending modes.

**4.18-b**, while the two corresponding eigenfrequencies are, in theory, very different. Therefore, it is possible to activate a resonant S-bending during stick-slip actuation, exciting the second eigenfrequency, but the employ of an elliptical motion in resonant condition is very difficult with this kind of actuators. The prototype of the S-bender developed and built by Università di Pisa is shown in **Figure 4.22** ([28]), while its main geometrical data are given in **Table 4.3**.

**Table 4.3.:** A summary of 1-DOF actuator dimensions

| | |
|---|---|
| $l$ | 30 mm |
| $b$ | 5 mm |
| $a$ | 0,8 mm |
| $hp$ | 0,5 mm |
| $hm$ | 0,3 mm |
| $s$ | 5 mm |
| $c$ | 2 mm |
| $t$ | 1,5 mm |

### 4.3.3. The case study: new design of piezoelectric actuators

As above mentioned, it's more desirable to have an elliptical motion than an S-bending or U-bending vibration. In order to obtain it, it's necessary to reduce the distance between the first and the second eigenfrequency (ideally the two eigenfrequencies should be overlapped). In this case it will be possible to activate a resonant elliptical motion, controlling the system with an input frequency located in the middle between the U-bending eigenmode and the S-bending eigenmode.

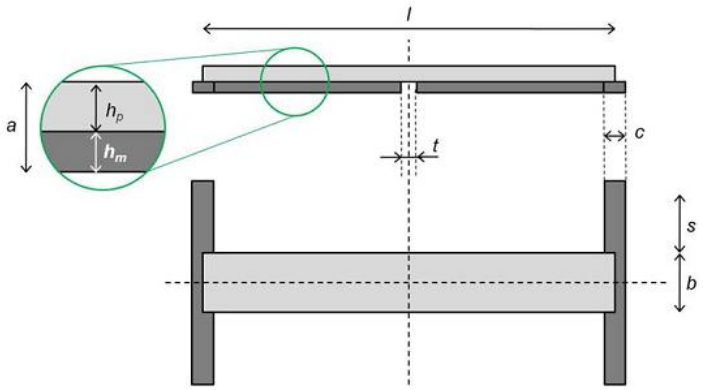


**Figure 4.22.:** Drawing of the existing prototype of the S-bender.

After an experimental analysis, the prototype of S-bender previous presented has been re-designed. The beam bender's length is reduced (from 30 mm to 24 mm), in order to obtain a general increment of eigenfrequencies, as shown in **Figure 4.23** ([28]).

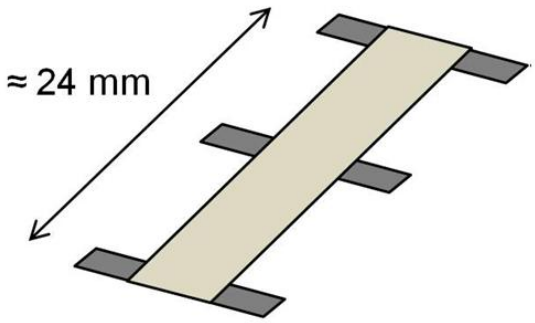


**Figure 4.23.:** Architecture of the new 1-DOF actuator.

Furthermore, a 2-DOF version of the actuator has been designed: it is a linear piezoelectric motor with two orthogonal S-bending modes that can be controlled separately, in order to move the target along an arbitrary line. In order to obtain a 2-DOF configuration, two piezo-metallic beams are combined in a "cross-form" structure, as shown in **Figure 4.24** ([28]).

In this way the system has a first mode of simple bending, with maximum displacement in correspondence of the centre, while the second and the third mode are orthogonal S-bending modes with the same frequency. In order to reduce the distance between the first mode and the second/third mode, an additional spring in the centre is used; that spring is composed by eight radial protrusions, as shown in **Figure 4.25** ([28]). Furthermore, four additional masses are situated at the four

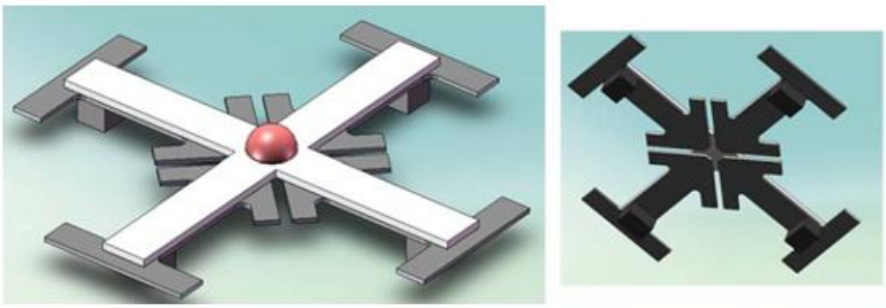

**Figure 4.24.:** Preliminary CAD model of the 2-DOF actuator.

edges of the cross.
The dimensions are given in **Table 4.4**.

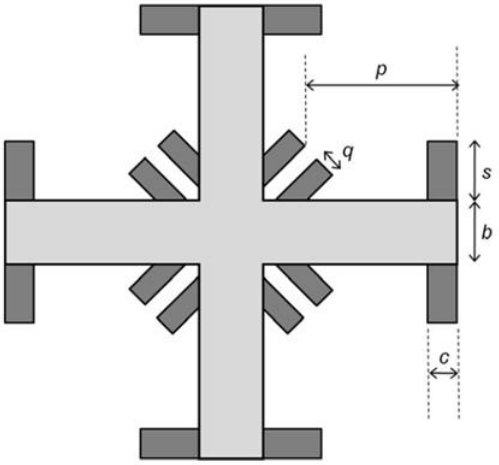


**Figure 4.25.:** Geometrical parameters of the 2-DOF actuator.

**Table 4.4.:** A summary of 2-DOF actuator dimensions

| | |
|---|---|
| $l$ | 30 mm |
| $b$ | 5 mm |
| $s$ | 2,7 mm |
| $c$ | 2 mm |
| $p$ | 8 mm |
| q | 1,5 mm |

## 4.4. Fine abrasive water jet of piezoelectric ceramics against competitors

In the field of micro application, the most appealing technologies are laser, wire EDM, micro milling and fine abrasive water jet : particularly, laser and wire EDM have a great attraction in terms of precision machining, assuring very strict tolerances. A comparison between laser and water jet technology is shown in **Figure 4.26** ([32]), in terms of beam diameters: for the fine AWJ used in this work, the diameter of the jet is around of 600 µm.

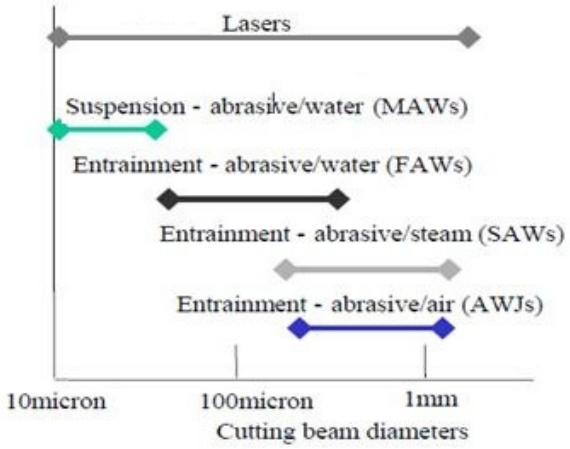


**Figure 4.26.:** Cutting beam diameters for abrasive water jets and lasers.

Water jet is a very attractive technology in the field of micro applications of piezoceramics, because it is basically a cold cutting: in fact, water jet not only transfers its kinetic energy to abrasive particles but acts also as a coolant to carry away the heat generated by the machining process of abrasion and erosion. Then, as a result, there is no heat affected zone in the material, which might induce thermal damage, localized modification of the chemical properties of the parent material and changes of piezoelectric behaviour. For these reasons, the competitors in the field of micro application as laser technology and wire EDM are not desirable in the machining of piezoelectric ceramic. Moreover, the piercing process for wire EDM has to be done by a separate process, requiring additional fixture and machining.
The water jet cutting causes no mechanical stresses on the machined material: as a matter of fact, it induces light compressive stresses, abrasion and erosion into the material, but the machined surface doesn't show any residual stresses and the toughness is quite well. In this case, micro milling is not desirable because of the high stresses that are needed to machine the brittle piezoelectric material. In addition, piezoelectric ceramics are characterized by anisotropy which is not a problem for water jet since it is not sensible to material anisotropy.

A possible competitor could be the ultrasonic machining, that is a non-thermal, non-chemical and non-electrical machining process that leaves unchanged the workpiece chemical composition, material microstructure and physical properties. The main drawback of this technology is that the material removal rates is lower than water jet's one when machining materials with high hardness and fracture toughness, as piezoelectric ceramic.

### 4.4.1. The case study: water jet against laser machining

The 2-DoF actuator, described in **Section 4.2** is machined by both laser and fine water jet. A comparison in this field of applications between these two technologies is necessary. With a qualitative analysis, the result obtained with laser machining is good, in terms of roughness, even if there is a heat affected zone. Two attempts of 2-DoF actuator is shown in **Figure 4.27**.

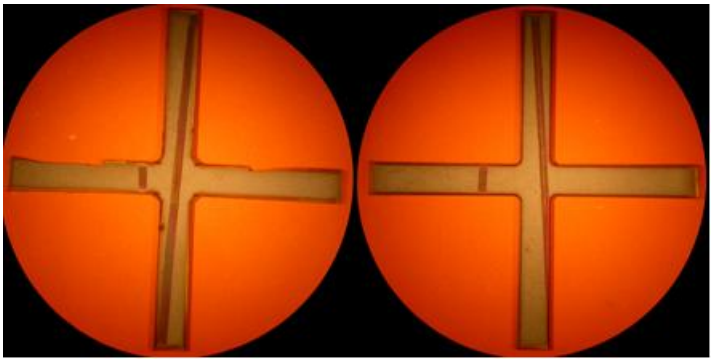

**Figure 4.27.:** 2-DoF actuator machined at Università degli Studi Federico II di Napoli.

Analyzing the enlargement in **Figure 4.28**, the heat affected zone is evident and so the piezoelectric properties are not the same in the whole section. This zone is particularly pronounced in non-linear cutting zone: this is due to the fact that in bends there's a major amount of heat.

The PZT material machined with laser is the same described in Sect.4.1, characterized by a TC = 350° C, so the extension of heat affected zone is quite small. This kind of piezoelectric materials are also called "soft" piezoceramics: it's impossible to machine "hard" piezoceramics with laser because the TC is lower (around 150° C), so the extension of the heat affected zone would be bigger. Nowadays this kind of actuators is made by soft piezoceramics, even if hard piezoceramics have better properties: this is due to the fact there was no alternative to laser machining. Fine water jet machining gives the opportunities to work also with hard piezoceramics, opening new researches opportunities in this field.

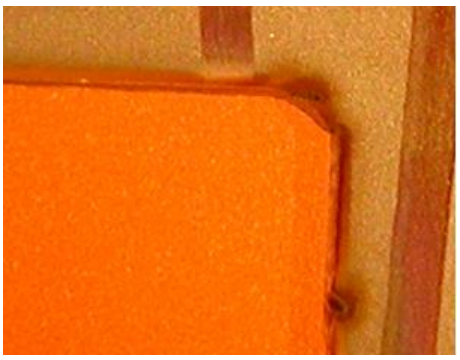

**Figure 4.28.:** An enlargement of 2-DoF actuator that shows clearly the heat affected zone.

## 4.5. Material removal mechanism

The impact of a single solid-particle is the basic event in the material removal mechanism by abrasive water jet. Therefore, a brief review on the material erosion mechanism by solid –particles is given in this paragraph.
The literature about solid-particles erosion is extensive. In [33] the authors present two cutting models based on fracture mechanics, in order to develop an abrasive water jet model for cutting brittle materials. In [34] the authors identify four steps in the material removal mechanism in abrasive water jet machining: plastic deformation and crack initiation, stress wave propagation, micropits, intergranular cracking and interlamellar/translamellar fracture. In [35] tthe authors inspect change of removal mechanism as a function of cutting depth and material properties. In [36]the authors determine the dominant erosion mode for polycrystalline ceramics is intergranular cracking. In [37] the authors investigate the material removal process in refractory ceramics, in particular bauxite, sintered magnesia and magnesia chromite. In [38] intergranular cracking and plastic flow are recognized as the dominant material removal mechanism in polycrystalline ceramics. In [39] tthe authors develop an analytical model for material removal in abrasive water jet machining of brittle materials. In [2] the authors make a summary of material removal mechanism both for ductile and brittle material.
There are four removal main mechanisms, as shown in **Figure 4.29** ([2]): cutting, fatigue, melting and brittle fracture.

These mechanisms generally do not act separately, but in combination, as shown in **Figure 4.30** ([2]). Their importance for the particular erosion process depends on several factors, such as the impact angle, the particle kinetic energy, the particle shape, target-material properties and environmental condition.

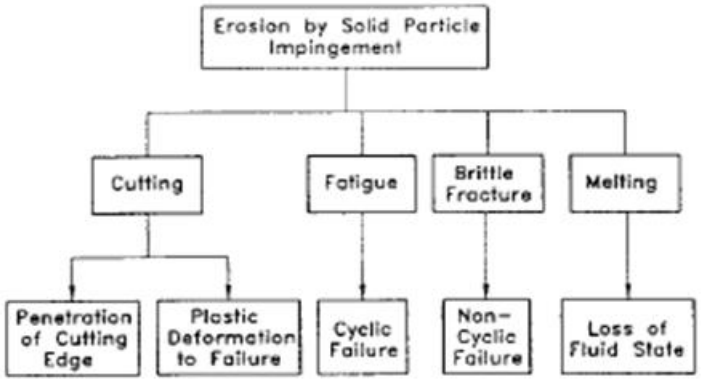


**Figure 4.29.:** Mechanism of material removal by solid-particle erosion .

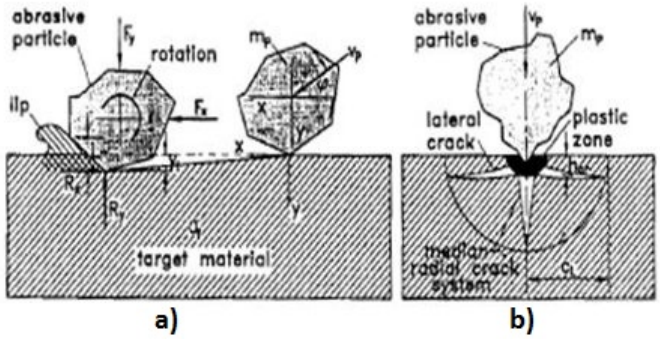


**Figure 4.30.:** Solid-particle material removal characteristics: a ) Micro-cutting; b) Lateral cracking.

### 4.5.1. Erosion mechanism of a polycrystalline ceramic

In [38] there is an analysis on brittle-behaving materials, particularly on polycrystalline ceramics, such as piezoelectric ceramics.
In an abrasive water jet cutting process, abrasive particles are entrained into a supersonic water stream to form an extremely erosive jet. When such an abrasive water jet is focused on a workpiece, the entrained abrasive particles erode the target rapidly and a kerf is formed. Due to the energy dissipation, the cutting power of the jet decreases along its path: this phenomenon is shown in **Figure 4.31** ([38]).

Through grooving, sweeping and cutting experiments by an abrasive water jet under low and perpendicular impact angles, a mixed material removal mechanism that consists of brittle/fracture phenomena and plastic deformation is identified. For the low impact angle, they mainly indicate scratching marks by single abrasive grains but also some inter-granular cracking. In contrast, inter-granular fracture dominates the material removal mode at perpendicular impact angles, as shown in **Figure 4.32** ([39]). Under this condition, it is observed that some material grains undergo den-

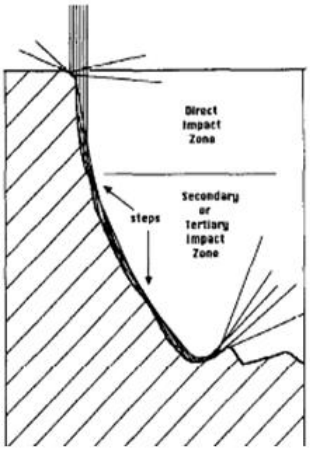


**Figure 4.31.:** Steps impacted by deflected jet.

sification, which indicates the effects of plastic deformation. Traces of plastic flow are present but considerably smaller and shorter than those for low impact angles.

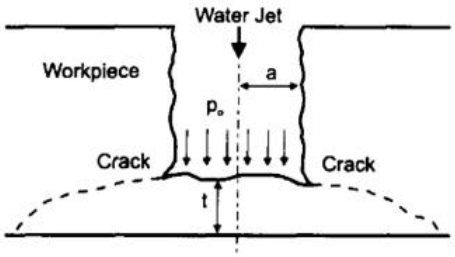


**Figure 4.32.:** Model of crack formed as jet exits from workpiece.

The erosion mechanisms of polycrystalline ceramics under abrasive water jet conditions include intergranular cracking, as shown in **Figure 4.33** ([40]) and plastic flow, as shown in **Figure 4.34** ([39]).Typically, ceramics have higher resistance to plastic deformation than most of the metals due to the very high stresses needed for dislocations to be moved. However, in the event of a high velocity impact, the localized stresses at the impact site are so high that even a ceramic can show a certain degree of plasticity.

### 4.5.2. Preliminiary experiments in Politecnico di Milano

The experiments are carried out in Politecnico di Milano were designed to analyze the material removal mechanism of the piezoelectric ceramic and consist in a single

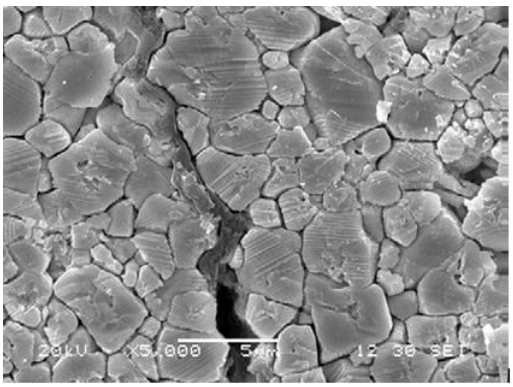

**Figure 4.33.:** Domain structure around cracks visualized by SEM microscopy: it's possible to see the typical intergranular cracking.

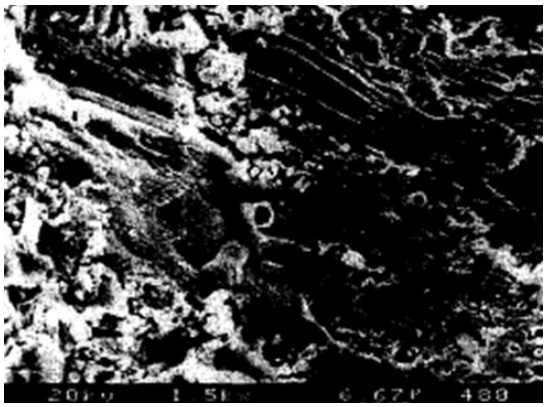

**Figure 4.34.:** Evidence of plastic flow and melting on an impact site of alumina ceramic sample (jet direction from right to left)

cutting of the material with the following parameters:
- perpendicular angle of impact
- standoff distance 3 mm
- pressure 300 MPa
- feed rate 200 mm/min

The following analysis is developed in collaboration with Universita' di Pisa. The aim of the analysis is to observe the behaviour of a polycrystalline ceramic machined with fine water jet: with a quick analysis is possible to have a first feeling on the characteristics of the erosion mode of this piezoelectric ceramic. Other considerations are pointed out in **Section 5.2**, where an accurate analysis of the kerf is developed.
As a matter of fact, the cutting surface is quite irregular, presenting the typical crater of brittle materials, as shown in **Figure 4.35**.
**Figure 4.36 − 4.37 − 4.38** show three additional enlargement of the cutting surface, where it is possible to see clearly the typical microchipping of erosion mode for

polycrystalline ceramics.

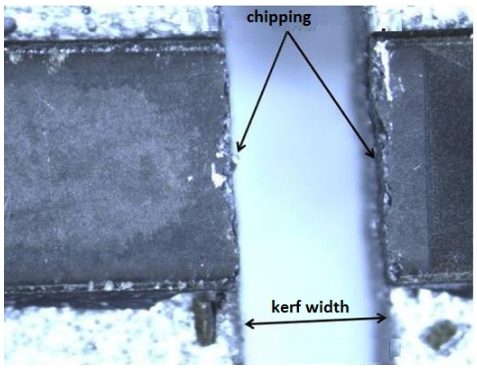


**Figure 4.35.:** Enlargement of cutting surface with optical microscope.

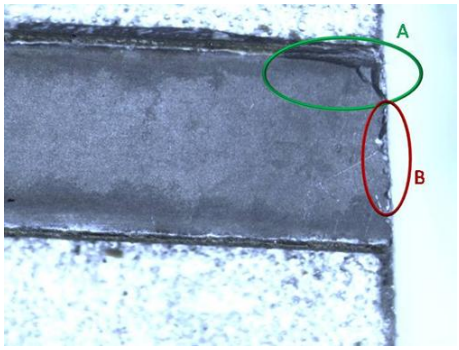


**Figure 4.36.:** Picture that shows the cutting surface: the circled zone A and B are enlarged furtherly.

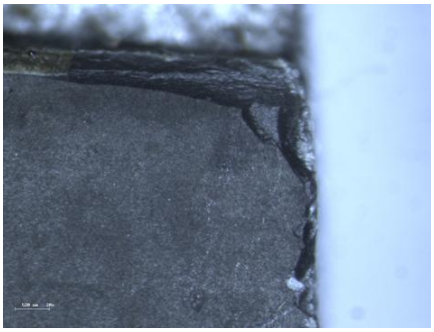

**Figure 4.37.:** Enlargement of 20x of zone A of previous picture.

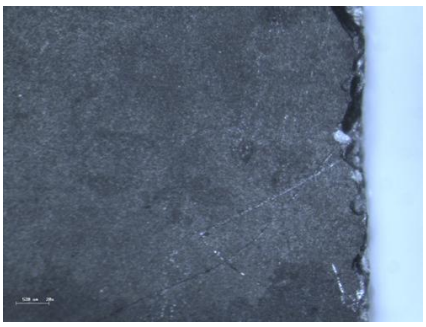

**Figure 4.38.:** Enlargement of 20x of zone B of previous picture.

A better analysis on the kerf produced by Fine AWJ will be presented in **Section 6.3**.

# 5. INTRODUCTION TO THE EXPERIMENTAL WORK

In this section, a literature review of the kerf quality attributes and the optimization of water jet cutting is pointed out; the first experimentation, carried out at Politecnico di Milano, is presented.

## 5.1. Optimization of water jet cutting: the state of the art

One of the fundamental aspects of any technology is the analysis of its total costs: **Figure 5.1** shows the analysis chart regarding AWJ.([41]).

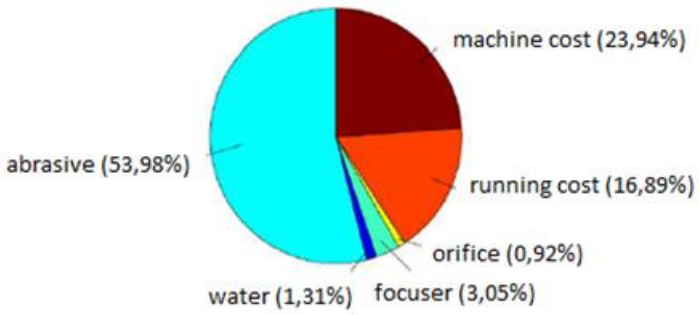


**Figure 5.1.:** Analysis of the costs in a water jet process.

The optimization of abrasive water jet technology can be divided into two categories: technical and economic.

In this work, the aim is the process technical optimization, based on physical relations between process parameters and their influence on kerf quality. Material removal mechanism, kerf quality and cutting performances are influenced by machining parameters (standoff distance, feed rate, impact angle, number of passes), process parameters (water pressure, orifice diameter, focuser diameter and length, abrasive type and mesh #, abrasive mass flow rate,) and the material properties.
There are also other parameters, which are very important for the cutting quality of the kerf: it is not possible to control them, but only to monitorize:

- fluctuations of pressure, caused by pumping system;

- fluctuations of abrasive flow rate, caused by the fluctuation of suction effect;

- influence of focuser wear on the mixing process;

- vibrations of workpiece caused by fixturing system;

- vibrations of cutting head, caused by motion system;

- statistical distribution of mesh #.

In literature, it is possible to find a lot of scientific papers, whose aim is to find the optimized parameters for water jet machining and employed in specific applications. In [2] the authors make a complete summary of the influence of cutting and working parameters on depth of cut. In [41] the author investigates the influence of parameters on machining of metal foam, making a comparison between technical and economic optimization. In [10] the authors study the influence of the process parameters on the depth of cut and kerf width of glass. In [42] the authors investigate the influence of process parameters on ductile materials, in order to optimized cutting quality, using a full factorial design of experiments. In [11] the authors make a research for modeling and optimizing the process parameters for ductile materials. Starting from literature, considering the cutting performance and material removal mechanism, the author of this work decided to investigate the influence of process parameters in the way is shown in the **Table 5.1**.

## 5.2. Kerf quality attributes

The precision of a water jet process is determined by the accuracy resulting from the machine handling system, the geometrical and technological process parameters and variables and the workpiece mechanical properties. The cut geometry, the topography and the integrity of the generated kerf surfaces are the parameters used to define the kerf quality attributes.
The possibility of achieving acceptable quality of the surface finish depends on the thorough understanding of the cutting mechanism and the process parameters influence.

**Table 5.1.:** The parameters investigated by the experimenter

| **Process parameters** | |
|---|---|
| Pressure | 3 levels |
| Feed rate | 3 levels |
| Abrasive flow rate | 2 levels |
| Diameter of orifices | 2 levels |
| **Constant parameters** | |
| Kind of abrasive | Garnet#200 |
| Angle of impacte | 90° |
| Diameter of focuser | 0,5 mm |
| Standoff distance | 1 mm |
| **Observed variables** | |
| Roughness | |
| Width on top of the cut | |
| Width on bottom of the cut | |
| Inclination of the kerf | |

### 5.2.1. Cut geometry

The **Figure 5.2** defines the parameters that characterize the geometry of a cut generated by abrasive water jet cutting.
These parameters are:

- top width of the cut ($b_T$)

- bottom width of the cut ($b_B$)

- taper of the cut ($T_R$)

- flank angle ($\varphi_F$)

- initial-damage width ($b_{IDZ}$)

- initial-damage depth ($h_{IDZ}$)

- smooth-cutting zone depth ($h_{ISC}$)

- rough-cutting zone depth ($h_{RC}$)

Abrasive water jet cutting introduces a roughening on the top surface along the kerf profile and produces a rounding at the entrance edge of the kerf. These are typical characteristics of abrasive water jet cutting and are attributed mainly to the abrasive particles at the jet periphery. These particles have low energy content, thus are unable to carry out cutting action. In fact the volume loss per individual particle collision is a function of the particle kinetic energy and it has been also noted that the active or cutting diameter is smaller than the jet real diameter and the more

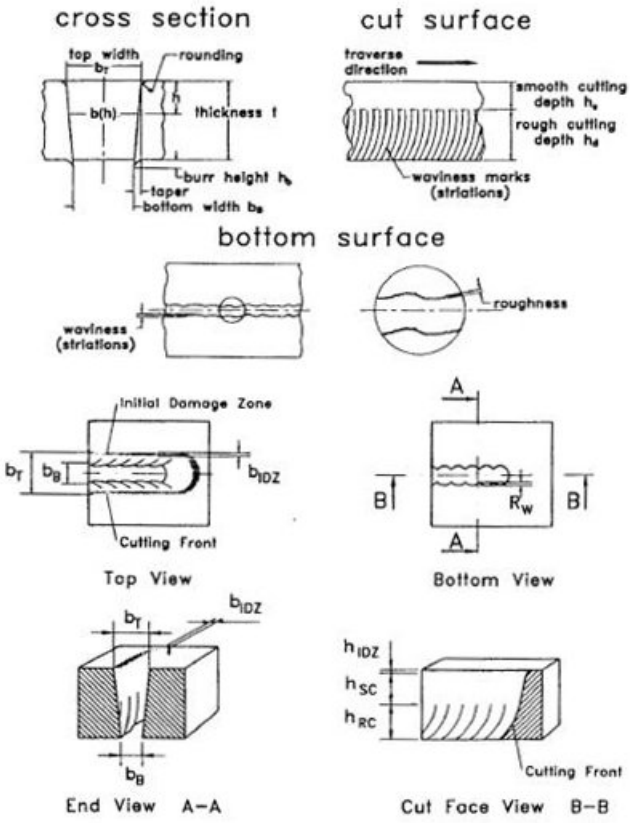


**Figure 5.2.:** Enlargement Geometry of a cut generated by abrasive water jet cutting.

external portion of the jet has to be considered as a boundary layer without enough cutting power. The energy distribution has been demonstrated to be high at the core and gradually decreasing towards the periphery. Such effect it is the cause for the damage at the entrance zone [43].

### Top kerf width

The influence of parameters, such as pressure, feed rate and abrasive flow rate, is shown in **Figure 5.3** ([2]). From **Figure 5.3a**, no general relation exists between the pump pressure and the top width of the cut in ceramics. The **Figure 5.3b** illustrates that the top cut width linearly decreases as the traverse rate increases. The **Figure 5.3c** shows that it is possible to observe a noticeable influence of the abrasive-mass flow rate on the top cut width: a larger top cut width corresponds to a larger abrasive-mass flow rate. This effect is of course more pronounced for low traverse rates.

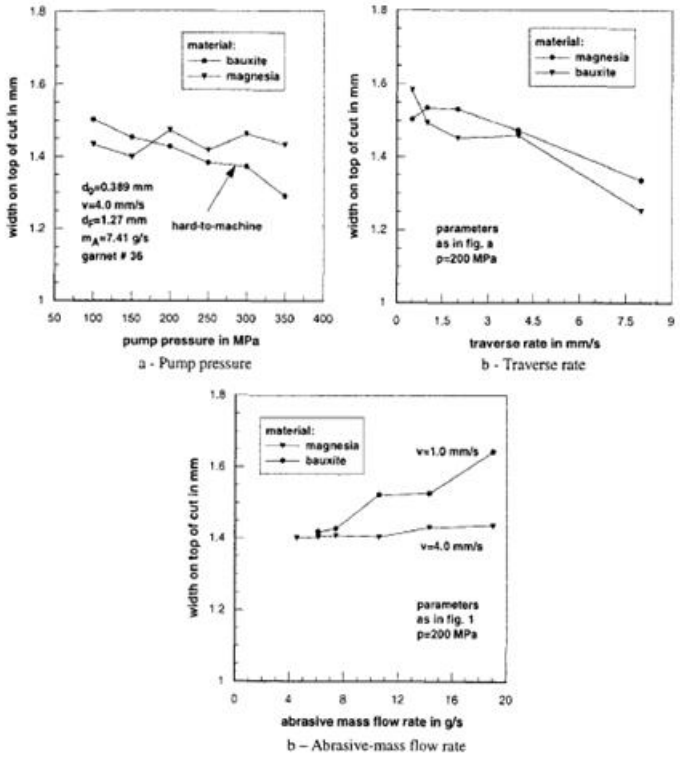


**Figure 5.3.:** Parameter influence on the top cut width in brittle materials

### Bottom kerf width

The influence of parameters, such as pressure, feed rate and abrasive flow rate, is shown in **Figure 5.4** ([2]). **Figure 5.4a** shows a general increase in the bottom width at high pump pressure. **Figure 5.4b** shows that the bottom cut-width decreases with higher traverse rates. This tendency is more pronounced with low-resistant ceramics. **Figure 5.4c** illustrateS that the width on bottom of the cut increase linearly with abrasive-mass flow rate. In **Figure 5.4d** it is possible to observe that a smaller width on the bottom of the cut corresponds to a high traverse speed.

### Kerf taper and flank angle

In **Figure 5.5** ([2]), the taper linearly increases with an increase in the traverse rate. For lower pump pressures and reduced abrasive-mass flow rates, the cut taper generally increases. At slow traverse rates, the taper switches from convergent to divergent: it is explained by the relative long exposure time at low traverse rate.

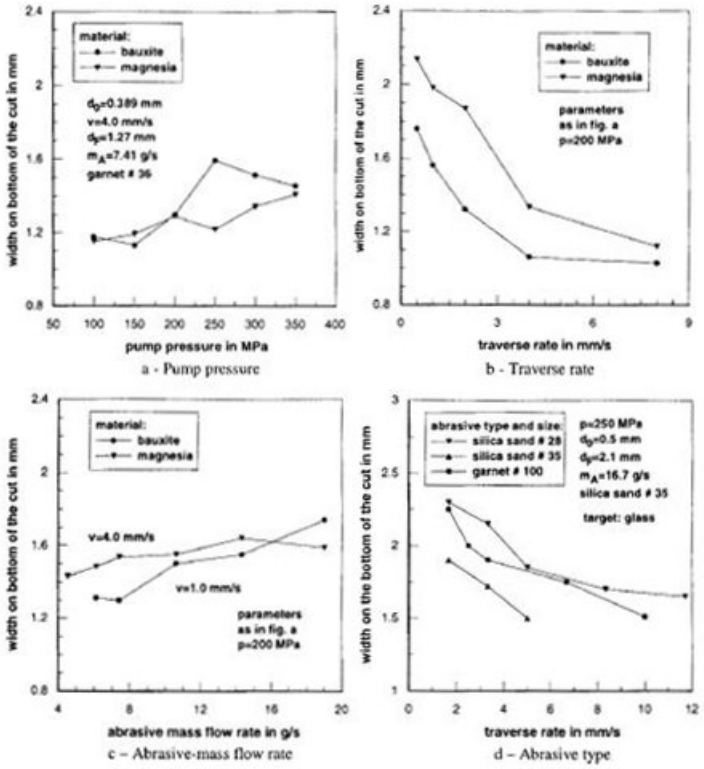


**Figure 5.4.:** Parameter influence on the bottom cut width in brittle materials

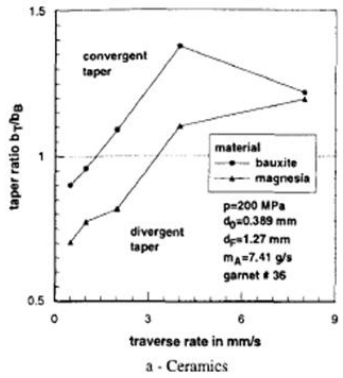


**Figure 5.5.:** Cut taper-formation in difficult-to-machine materials

**Figure 5.6** ([2]) shows results of flank-angle measurements in ceramics. The flank angle decreases as the pump pressure increases. At very high pump pressures, the flank angle tends to zero. The influence of the traverse rate is very pronounced. Also, a high traverse rate generates almost parallel kerf walls in all investigated material. The high-resistant ceramic predominantly shows divergent tapers. Low abrasive-mass flow rates generate almost untapered cuts except for the high-resistant

materials. The taper is much lower at high abrasive-mass flow rates when compared to the other materials.

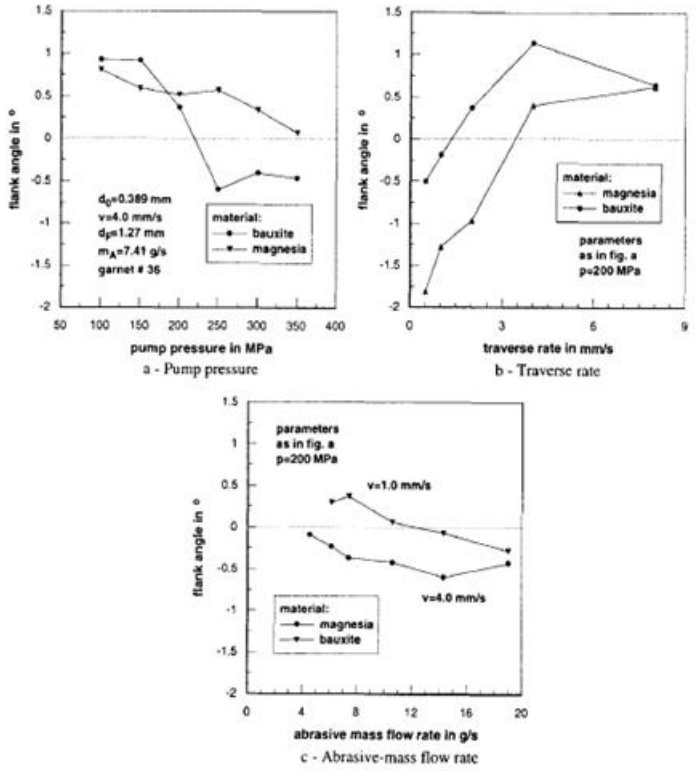


**Figure 5.6.:** Flank-angle formation in ceramic material

## 5.2.2. Topography of generated surface

The modification of surface integrity parameters is caused by the the material removal mechanism that causes complex phenomena involving shear, plastic deformation, wear, crack propagation and particles embrittlement. Due to the impingement of the jet on the workpiece surface, the stream of abrasive particles contacts metal surface, causes plastic flow of the surface material and removes microchips.
Abrasive water jet cutting process consists of two cutting modes, as shown in **Figure 5.7**: a cutting wear mode which occurs towards the entrance side of the kerf and a deformation wear mode which occurs deeper in the kerf towards the jet exit side. The two mechanism provide two different surface zones, the upper surface characterised only by roughness (smooth cutting zone), and the lower one characterised by roughness and waviness or striations (rough cutting zone). [43].

The analysis of surface profiles generated under different abrasive water jet cutting conditions is carried out qualitatively in terms of static characteristics, including the

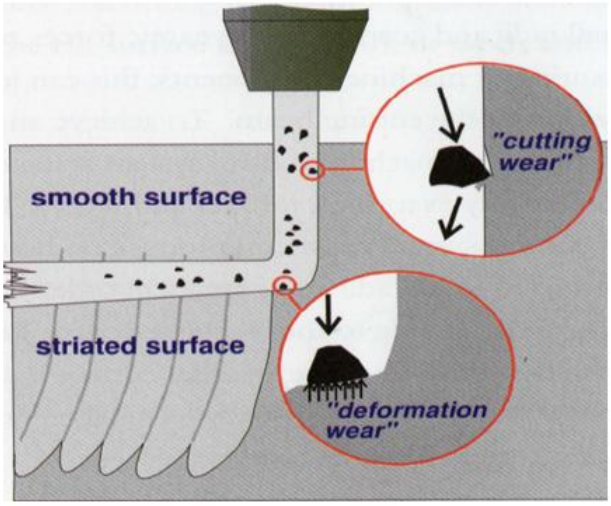


**Figure 5.7.:** Mechanism of water jet cutting.

roughness average (Ra), the peak-to-valley height (Rz) and the root mean square roughness (Rq).
An increase in the pressure, in general, improves the surface quality, as shown in **Figure 5.8a** ([2]). These results are due to the increased fragmentation probability of the abrasive particles as their velocity increases. This fragmentation reduces the size of the impacting abrasive particles. **Figure 5.8b** illustrates the influence of the orifice diameter on the surface finish: the differences in the roughness are not large, despite about a 100% difference in the orifice diameter. **Figure 5.8b** also plots typical relations between the traverse rate and the surface roughness: it significantly increases as the traverse rate increases. **Figure 5.8c** shows that focus length dos not influence the surface roughness. **Figure 5.8d** illustrates that surface roughness increases with an increase in the focus diameter.
**Figure 5.9a** illustrates the influence of the abrasive-mass flow rate on the surface roughness: it decreases with an increase in the abrasive-mass flow rate. **Figure 5.9b** shows the relation between the surface roughness and abrasive-particle diameter. In the range of small diameters, the roughness almost linearly decreases as the particle diameter increases. **Figure 5.9c** shows the influence of the abrasive type on the surface roughness. The use of the harder aluminium-oxide substantially reduces the surface roughness of the ceramic material being cut. The relation between the traverse rate and surface roughness depends on the abrasive type. In **Figure 5.9d** the author finds that the surface roughness substantially improves by selecting an appropriate abrasive-particle size distribution [2].

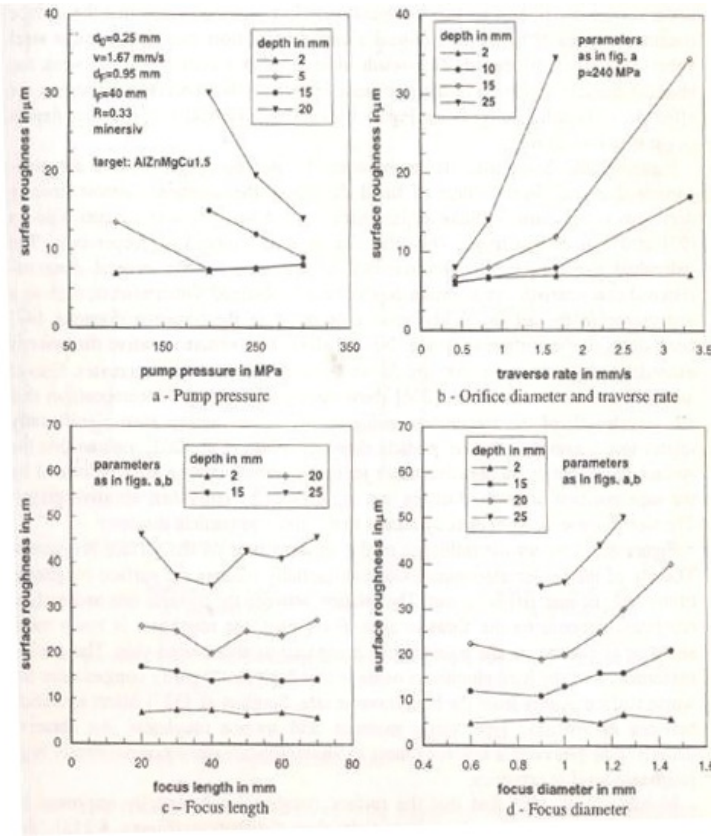


**Figure 5.8.:** Parameters influence on the surface roughness

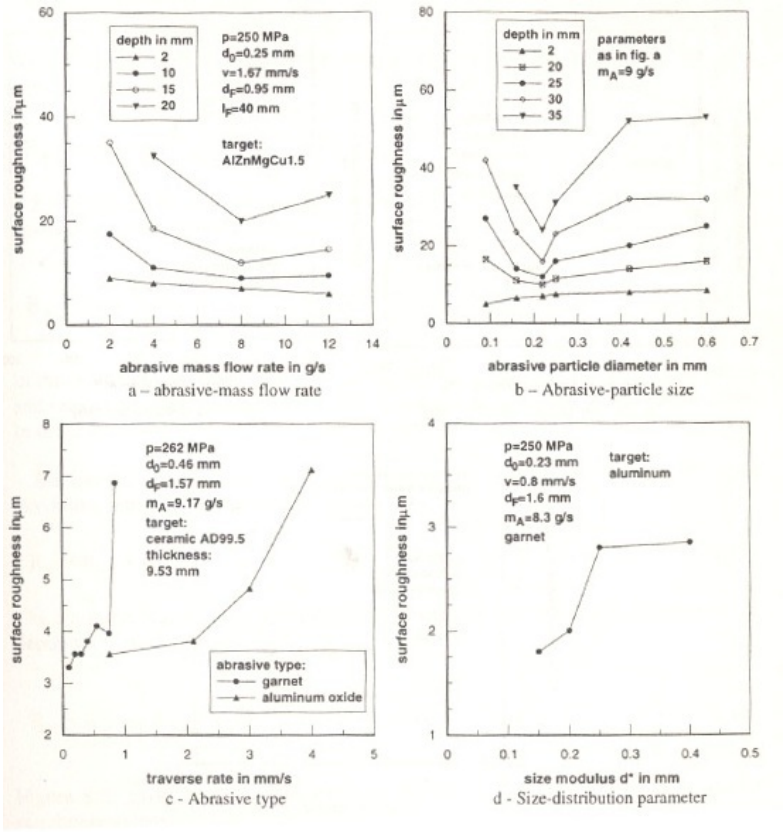




**Figure 5.9.:** Abrasive-parameters influence on the surface roughness

### 5.2.3. Integrity of generated surface

Kerf surface integrity is concerned primarily with the effects that a machining process introduces in the near surface layer below the visible surface of a component. Each process may produce a characteristic surface alteration that can be caused by the material removal mechanism and may affect both the physical and mechanical properties of the material. The main surface integrity parameters that can be relevant in abrasive water jet cutting are microhardness, residual stresses and material microstructure. In this work, these analyses are not carried out.

## 5.3. Feasibility experiments in Politecnico di Milano

The aim of the first experimentation is to show the feasibility of piezoelectric ceramic machining with abrasive water jet technology. The experimentation is made at Dipartimento di Meccanica of Politecnico di Milano, while the quality of the cutting kerf is analysed in Dipartimento di Ingegneria Meccanica Nucleare e della Produzione of Università di Pisa.
The first part of the experimental work is the fixing of the material: the resulting solution is characterized by biadhesive tape and three mass. The forces caused by cutting process are very weak, so it is possible to have this kind of fixturing system, as shown in as shown in **Figure 5.10**.

**Figure 5.10.:** The fixturing system used during the feasibility experiments.

Since the scarcity of piezoelectric material, a little DOE is designed: in these running experiments the only two parameters considered are pressure and feed rate. The values of pressure are 200 MPa and 300 MPa, while the values of feed rate are 30 mm/min and 60mm/min.
The experiments have been carried out according to the principle of random order to minimize the experimental error and with 3 replicates. **Figure 5.11** shows the experimentations carried out at Politecnico di Milano, **Figure 5.12** shows the specimen characterized by 12 cut with different conditions.

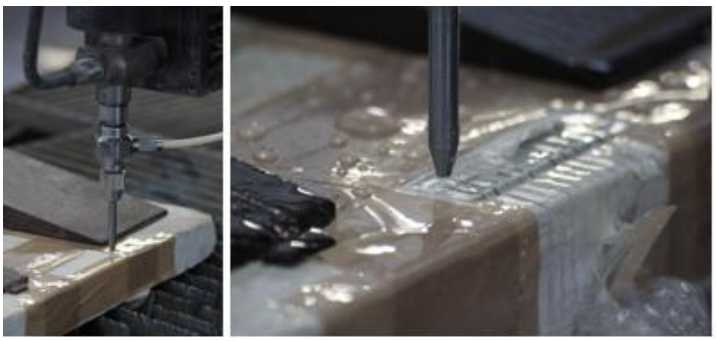

**Figure 5.11.:** Two pictures taken during the experiments

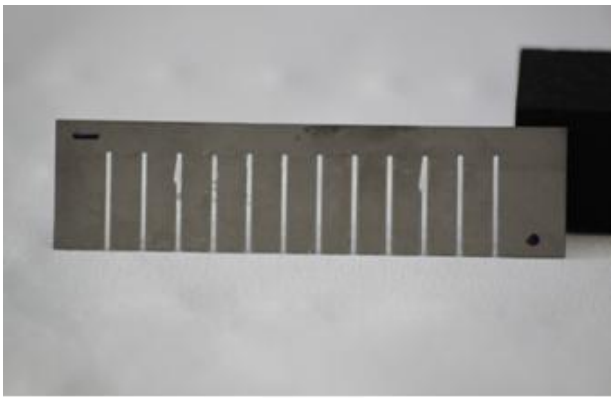

**Figure 5.12.:** The specimen after the feasibility experimentation.

After a qualitative analysis of the kerf, the best parameters chosen are 200 MPa as pressure and 30 mm/min as feed rate. These results are confirmed by a deepened analysis, made by Università di Pisa.

### 5.3.1. Quality of the cutting surface of feasibility experiments by Università di Pisa

Following the considerations in **Section 5.1** about the analysis of kerf quality attributes, it is possible to analyze the cutting surface of piezoelectric ceramic, in order to geometrically characterize the generated surface.
In microcutting of low-thickness piezoelectric ceramics only the cutting wear mechanism takes place and so it is possible to characterize the surface only by the definition of roughness, not taking into account for the waviness which is typical of the deformation wear mode. Moreover, it is possible to notice a rounding at the entrance edge of the kerf which is a typical feature of water jet cutting.
**Figure 5.13** shows an enlargement of transversal section: it is possible to notice that the whole section is irregular.

The analysis of the kerf quality of the first experimentation is made by Universita' di

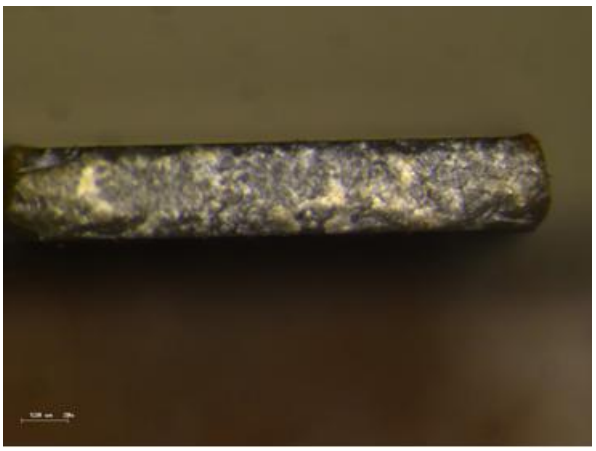

**Figure 5.13.:** Enlargement 20x of transversal section

Pisa. The most important effect to investigate is the roughness, with the profilometer shown in **Figure 5.14**, that markedly influences mechanical strength. It's clear that a high roughness is a possible start of cracks. Given the small dimension of the piezoelectric ceramic, the cut off value is $\lambda = 0.25$mm for a total length of $7 \cdot \lambda = 1{,}75$mm (a brief explication is shown in **Section 6.3**. The results of measuring are shown in **Table 5.2**, that reports the mean roughness Ra and the standard deviation.

**Figure 5.14.:** Profilometer used to make roughness measurements

Analysing these data, it seems that the pressure is not so important, while the feed rate has a differen rilevance. The best parameter of feed rate, in terms of roughness, is f = 60 mm/min. The reliability of this conclusion is low for the high level of the

**Table 5.2.:** The measurement of roughness

| Parameters | $\mu_{Ra}$ | $\sigma_{Ra}$ |
|---|---|---|
| f=60mm/min p=200MPa | 3,46 | 0,22 |
| f=30mm/min p=200MPa | 3,99 | 0,61 |
| f=60mm/min p=300MPa | 3,65 | 0,27 |
| f=30mm/min p=300MPa | 3,50 | 0,32 |

standard deviation.
A further analysis is made with SEM (**Figure 5.15**), that shows an interesting aspect for all the specimens: at the entrance of the jet, the machined surface is better than the outbound side, characterized by craters and chips.

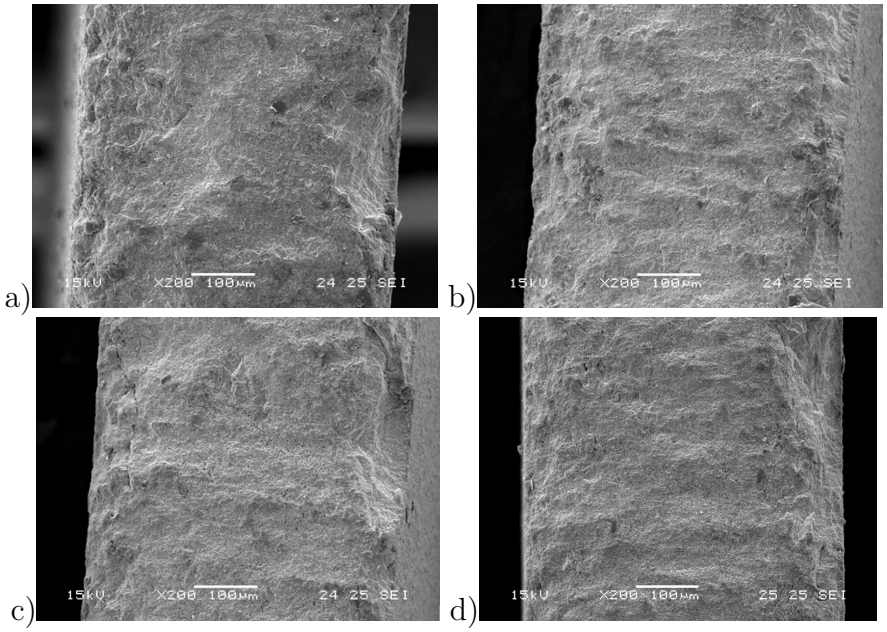


**Figure 5.15.:** The machined surface with a SEM analysis in different conditions (the entrance of the jet is on the left side): a) f=60 mm/min p=200 Mpa; b) f = 30 mm/min p=200 Mpa; c) f = 60 mm/min p = 300 Mpa; d) f = 30 mm/min p = 300 MPa

## 5.3.2. Conclusions

After the feasibility experiments, a first attempt to machine the piezoelectric actuator (2-DOF actuator) is made, as shown in **Figure 5.16**. Using the optimal parameters obtained with a qualitative analysis of the kerf (pressure of 200 MPa and feed rate of 60 mm/min), the cross-shaped actuator satisfies the requested properties.

The analysis of cutting surfaces with the optical microscope shows that the quality of the kerf is very different from the 2-DOF actuator machined with optimal parameter

**Figure 5.16.:** The 2-DOF actuator machined in Politecnico di Milano.

(**Figure 5.17**). Watching **Figure 5.18**, it is possible to notice the typical crater of material removal mechanism of a brittle material.

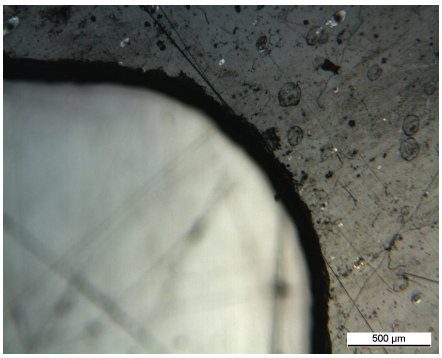


**Figure 5.17.:** An enlargement of 2-DOF actuator machined in Politecnico di Milano with optimizing parameter after the feasibility experiments.

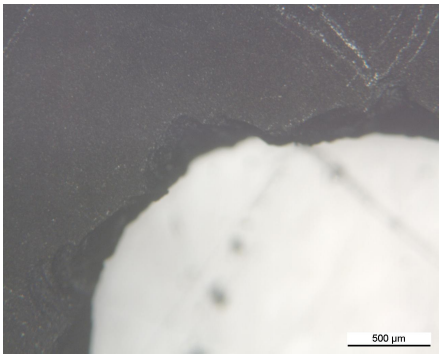


**Figure 5.18.:** An enlargement of 2-DOF actuator machined in Politecnico di Milano with non-optimizing parameter after the feasibility experiments.

# 6. EXPERIMENTAL DESIGN AND ANALYSIS OF THE RESULTS

In this section all the aspects regarding the experimentation are fully analyzed. The design of experiments is presented, including screening, optimization and validation experiments by analyzing the choice of the investigation parameters and their levels. The results of the quality analysis of the cutting surface are shown following the guide lines presented in **Section 5.2**.

## 6.1. Water jet system setup and monitoring

The first part of the experimental work consists in the water jet system setup, particularly the setup of the abrasive feeding system and the specimen fixturing system.

### 6.1.1. The hopper and the abrasive feeding system

The implementation of fine water jet system in a traditional water jet machine involves a new hopper to improve the versatility of the machine. As a matter of fact, in this way it's possible to change the system (from fine to macro) more rapidly, without losing time emptying and cleaning the hopper. The choice to do a self-made mini hopper (**Figure 6.2**) is due to the required versatility of water jet system. This self-made feeding system is characterized by a small cylinder, that contains the abrasive, a bar to switch manually on/off the feeding system and a selector bar to regulate the abrasive flow rate.

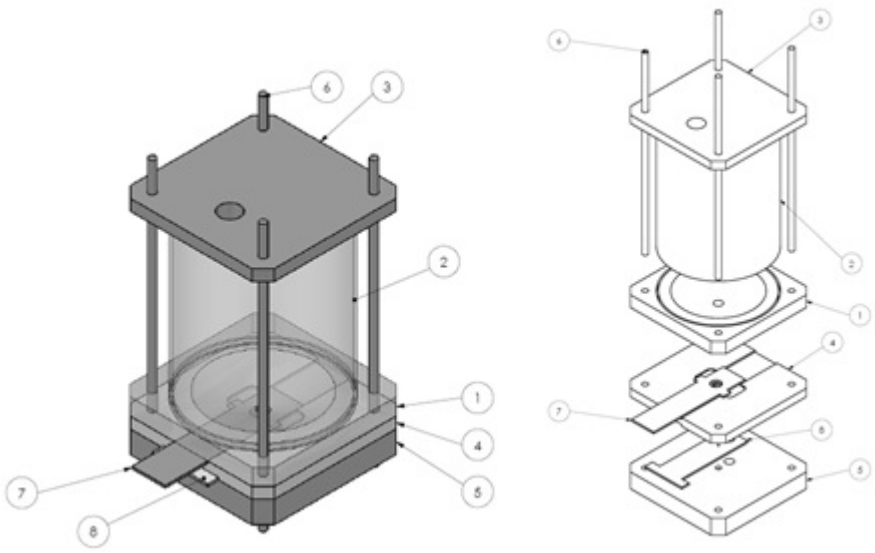

**Figure 6.1.:** The 3D-drawing of the new mini-hopper designed in cooperation with Tecnalia: 1) lower base; 2) cylinder; 3) upper base; 4) selector base; 5) lid; 6) rod; 7) selector; 8) selector of flow rate

The abrasive feeding system (**Figure 6.2**) is composed by:

- a cylinder, to contain abrasive particles;
- an upper cap, to avoid the dirty enter the hopper
- an upper base
- a bar, to switch ON / OFF of the system
- a lower base, with an air valve
- a selector bar with calibrated holes to select the abrasive flow rate

Since the mini-hopper is self-made, the abrasive feeding system requires a specific calibration in order to find the corresponding abrasive flow rate and the specific calibrated hole in the selector bar working at the different process parameters. The abrasive flow rate is principally influenced by the gravity, the calibrated hole diameter through which the abrasive flows and the suction effect caused by the Venturi effect of the jet inside the mixing chamber. Because of this, the calibration is performed by measuring the difference in the hopper weight after 30s in real working conditions. The calibration is made only for Garnet#200 with different measuring bar: the upper level of abrasive flow rate is set to 150 g/min which is the physical limit of the suction capability of the cutting head. The results are presented in **Table 6.1**: the mean value for the diameter hole of 2 mm is 84,2 g/min (the standard deviation is 5,5 g/min), and mean value for the diameter hole of 2,5 mm is 134 g/min (the standard deviation is 3,5 g/min). The value of standard deviation is compatible with the values present in the calibration of abrasive system in [41].

**Figure 6.2.:** The self-made mini hopper installed in the water jet system.

**Table 6.1.:** Calibration of abrasive system

| Pressure [MPa] | Abrasive flow rate [g/min] | Diameter hole [mm] |
|---|---|---|
| 250 | 83,6 | 2 |
| 250 | 132,8 | 2,5 |
| 300 | 90,1 | 2 |
| 300 | 138 | 2,5 |
| 350 | 79 | 2 |
| 350 | 131,4 | 2,5 |

It's necessary to demonstrate that the experimental conditions with this self-made mini hopper are always the same: working with a new orifice every run verifies this essential condition. A monitoring of the depression in the abrasive feeding tube is carried out in order to demonstrate that there is no relationship between the pressure level and the suction caused by the Venturi effect.
**Figure 6.3** shows that the suction is nearly equal for values of pressure of 250 and 350 MPa, provided the orifice is in good conditions. On the contrary, **Figure 6.4** shows that tthe suction depression is not equal in case the orifice is worn: as a consequence, with this abrasive feeding system, it is necessary to work with the orifice in optimal conditions not to change the power of suction of the cutting head.

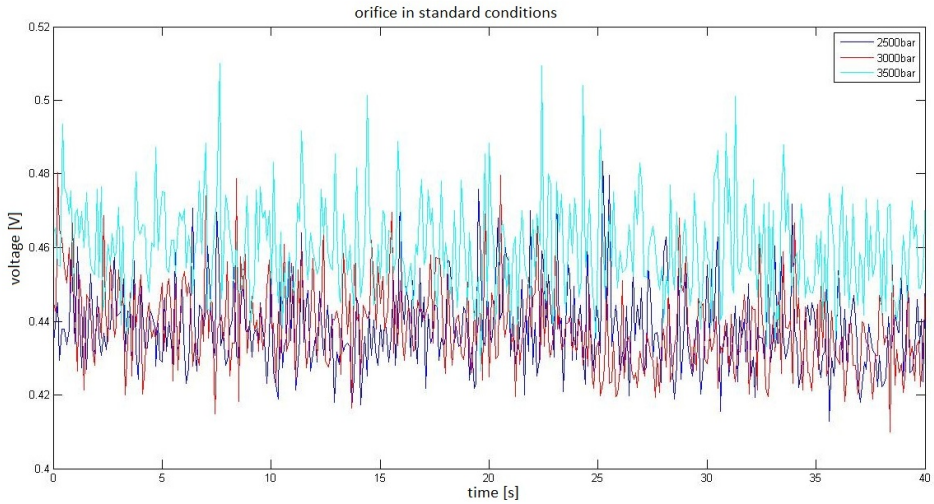


**Figure 6.3.:** Good orifice: the signal shows that the working pressure does not influence the depression in the abrasive system.

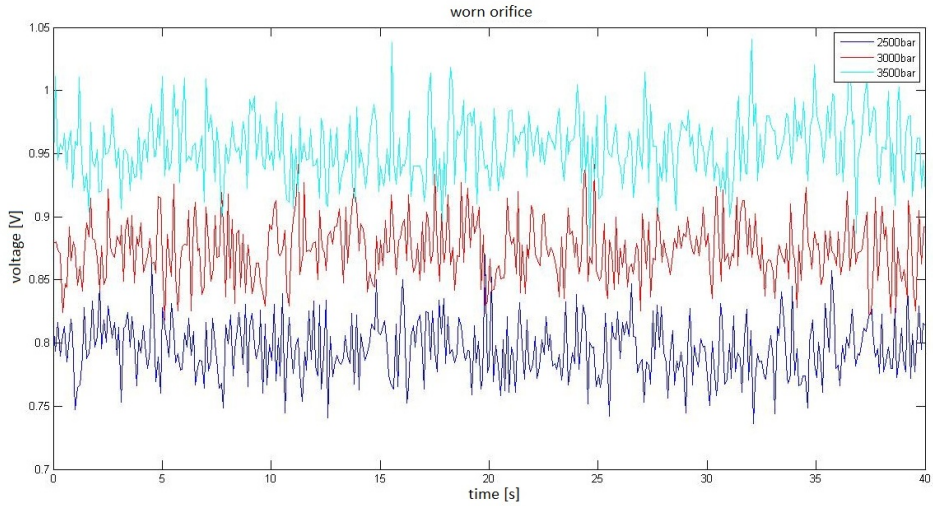


**Figure 6.4.:** Worn orifice: the signal shows that the working pressure influences the depression in the abrasive system.

Moreover, it is possible to demonstrate that there is no correlation between the pressure fluctuations, due to the pump frequency, and depression fluctuations, when the orifice is in good conditions (**Figure 6.5**). On the contrary, when the orifice is worn, there's a clear correspondence between pressure and depression fluctuations (**Figure 6.6**).

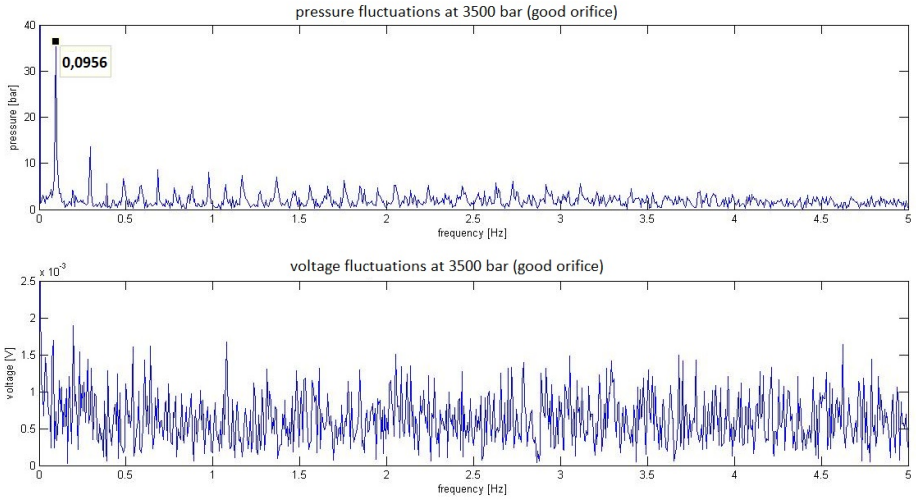


**Figure 6.5.:** The signal shows that the pressure fluctuations do not influence the depression in the abrasive system if the orifice is in good conditions.

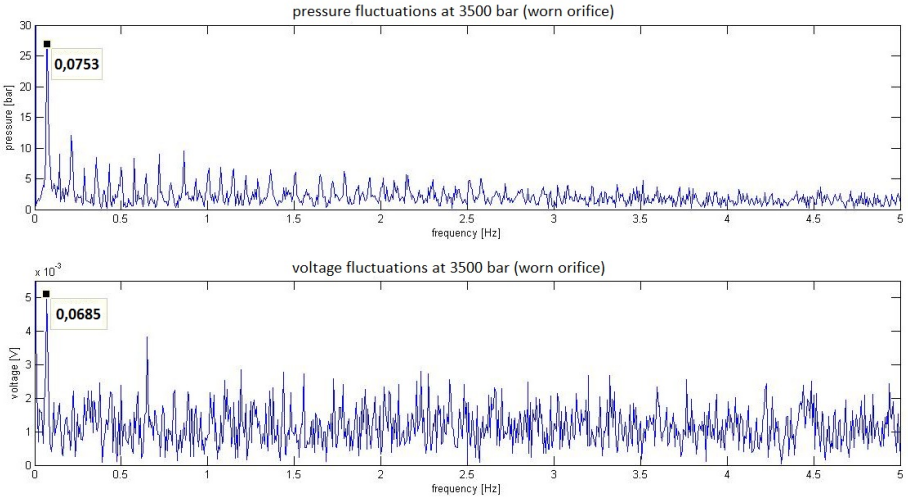


**Figure 6.6.:** The signal shows that the pressure fluctuations influence the depression in the abrasive system if the orifice is worn.

Furthermore, it's possible to demonstrate that the kerf is affected by the fluctuations of the abrasive, analyzing the **Figure 6.7**. The feed rate is 100 mm/min and the frequency of the peaks of machined edge is 0,64 Hz: the same frequency is evident in the frequency analysis of the depression, shown in **Figure 6.8** (it's not possible to see the frequency of 0,07 Hz because the cut lasts less than 15 s).
Finally, the correct setup of this water jet system implies the use of a new orifice.

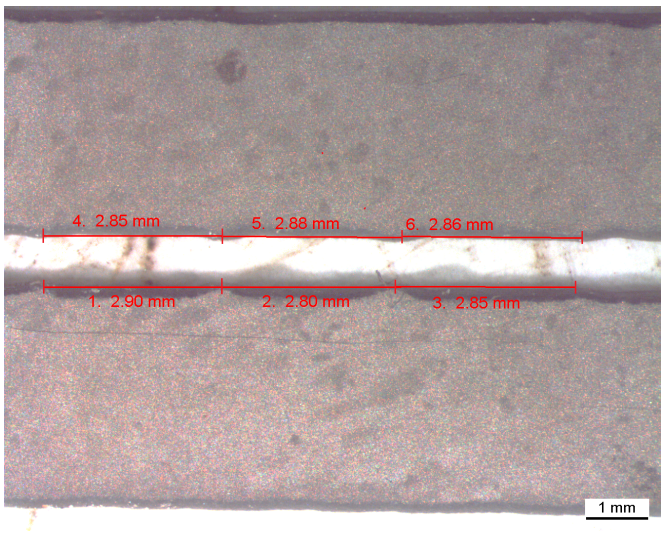


**Figure 6.7.:** The distance among the peaks is more less 2,85 mm, that is equivalent to a frequency of 0,64 Hz.

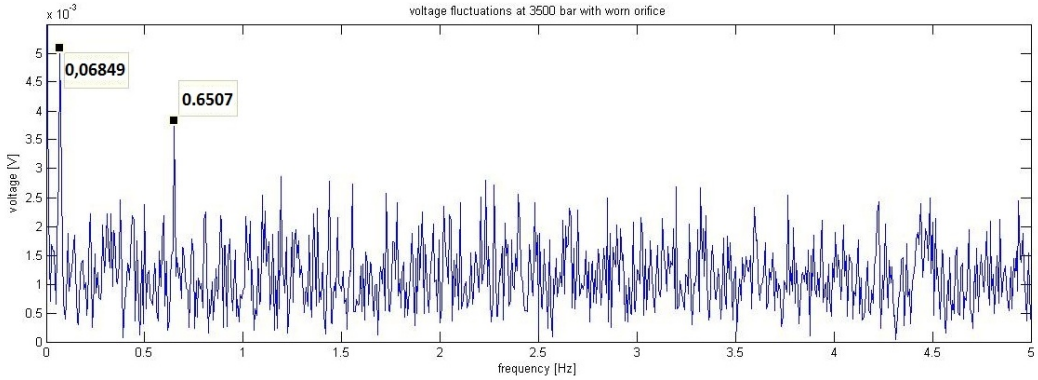


**Figure 6.8.:** Depression fluctuations affect directly the quality of the cut surface.

### 6.1.2. The fixturing system

The fixturing system is quite simple but specifically customized for the target material. In fact, the piezoelectric thin specimen is very brittle, so it needs to be properly fixed on a rigid substrate in order to avoid shocks or vibrations which could be dangerous for its integrity: the final solution was to fix it on a piece of hard polystyrene with an adhesive tape, as shown in **Figure 6.9**. This is possible because of the small applied forces on the workpiece. **Figure 6.10** shows a correct setup of the system, after which it is possible to start the experimentation

**Figure 6.9.:** The fixturing system used during this experimentation.

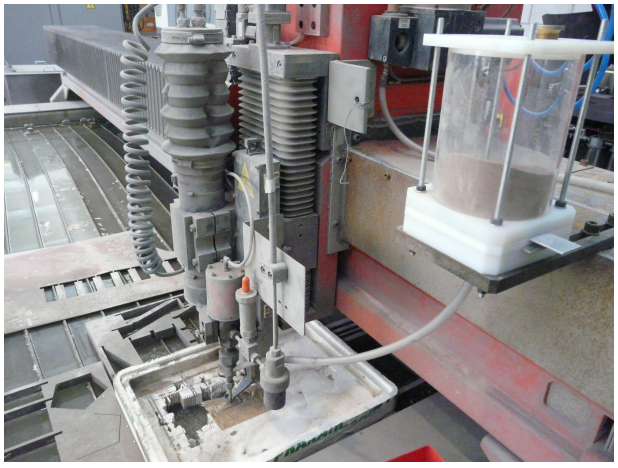

**Figure 6.10.:** The final setup of the waterjet system used to machine piezoelectric material.

## 6.2. Design of experiments

In water jet technology there are many parameters that can influence the quality of cutting surface: the choice of the variable parameters for this experimentation is made starting from the literature review, presented in **Section 5.2**.
The literature review points out that pressure, orifice diameter, focus diameter, abrasive mass flow rate and feed rate are the most influential parameters. Particularly, feed rate seems to be the most important influencing parameter for ceramic machining, while the influence of focuser length has less importance thus this parameter is not involved in the investigation.
During the experimentations, some parameters were are kept constant, as shown in

**Table 6.**2.

**Table 6.2.:** Constant parameters used in this experimentation

| Parameter | Level |
|---|---|
| Focus diameter | 0,5 mm |
| Focus length | 76,2 mm |
| Impact angle | 90° |
| Numebr of passes | 1 |

All data about this experimentation (screening, optimization and validation experiments) are shown in **Appendix A**.

### 6.2.1. Statistical review

A Design Of Experiments (DOE) approach was used a a statistical method of analysis during the present work. Much of knowledge about products and processes in the engineering and scientific disciplines is derived from experimentation. An experiment is a series of tests conducted in a systematic manner to increase the understanding of an existing process or to explore a new product or process. Design of Experiments (DOE), is a tool to develop an experimentation strategy that maximizes learning using a minimum of resources. DOE essentially helps in identifying relationships between causes and effects, providing an understanding of interactions among the influencing factors, determining the levels to set the controllable factors in order to optimize the target result, minimizing the experimental error and improving the robustness of the design to variation.
The methodology of DOE ensures that all factors and their interactions are systematically investigated; thus, information obtained from a DOE analysis is much more reliable and complete than results from one-factor-at-a-time experiments that ignore interactions and may lead to misleading conclusions.
In any experiments, variability arising from a nuisance factor can affect the results. Generally, a nuisance factor is a design factor that probably has an effect on the response, but it is not interesting in that effect. When the nuisance source of variability is known and controllable, the design technique called blocking can be used to systematically eliminate its effect on the statistical comparisons among treatments.

### 6.2.2. Screening experiments

The aim of the screening tests is to determine the upper level of the feed rate parameter. **Table 6.3** summarizes both the variable and constant parameters used in this screening tests. The constant parameters are taken from a previous experimentation, carried out at Politecnico di Milano.

**Table 6.3.:** Constant parameters used in this experimentation

| **Parameter** | **Level** |
|---|---|
| Variable parameters | |
| Feed rate | 90 - 110 - 130 - 150 - 170 - 190 mm/min |
| Constant parameter | |
| Kind of abrasive | Garnet#200 |
| Abrasive flow rate | 80 g/min |
| Pressure | 250 MPa |
| Orifice diameter | 0,15 mm |
| Standoff distance | 1 mm |

At this stage of the experimentation, the analysis of the kerf is mainly qualitative and just a visual geometric analysis is considered. As shown in **Figure 6.11**, at 190 mm/min the kerf is not rectilinear; moreover, the characteristic fracture mode of brittle materials is more evident in the case of feed rate 190 mm/min and 150 mm/min (**Figure 6.12**). Finally, the screening tests show that the highest level of feed rate characterized by a good kerf quality , is 110 mm/min (**Figure 6.13**).

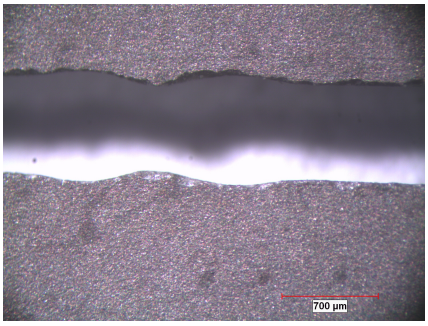


**Figure 6.11.:** Kerfs quality at feed rates of 190 mm/min

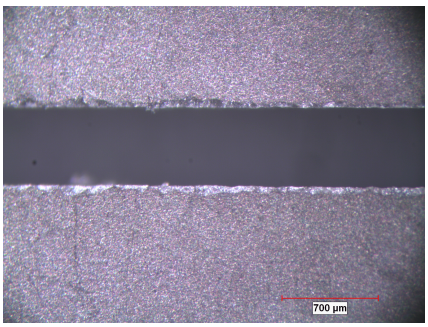


**Figure 6.13.:** Kerfs quality at feed rates of 110 mm/min

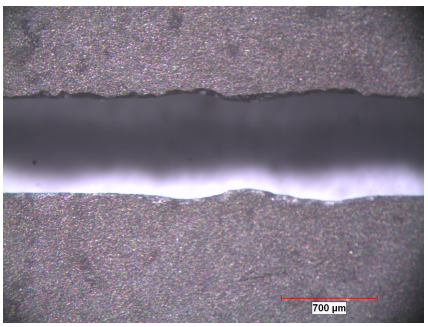


**Figure 6.12.:** Kerfs quality at feed rates of 150 mm/min

### 6.2.3. Optimization experiments

The aim of the second step of this experimentation is to find the best parameters in terms of kerf quality, particularly in terms of roughness, in order to verify if water jet is an appealing technology in the machining of piezoelectric ceramics.
A DOE approach is chosen as optimization technique, where the investigated parameters are feed rate, pressure, abrasive flow rate and orifice diameter. In these tests, the flow rate is chosen within the physical limits of the cutting head, capable to have a regular flow rate up to 150 g/min. The upper level of feed rate was determined by the previous screening tests, while the lower one is determinated by the experimentation carried out at Politecnico di Milano. For fine abrasive water jet, the typical orifices have a diameter of 0,15 and 0,18 mm and the Garnet#200 is characterized by finer abrasive particles. The standoff distance is 1 mm because for micro applications the jet is more coherent.
In **Table 6.4** there is a summary of investigating and constant parameters.

**Table 6.4.:** Parameters of optimization tests.

| **Parameter** | **Level** |
|---|---|
| Variable parameters | |
| Feed rate | 30 - 70 - 110 mm/min |
| Abrasive flow rate | 80 - 140 g/min |
| Pressure | 250 - 300 - 350 MPa |
| Orifice diameter | 0,15 - 0,18 mm |
| Constant parameters | |
| Kind of abrasive | Garnet#200 |
| Standoff distance | 1 mm |

In optimization experiments, it's necessary a blocking approach, because it's very difficult to assure the same operative conditions: in this case, the block is represented by the orifice. The operations of assembly and disassembly of the orifice mounting can be complex and can easily cause its damage. for this reason, the continuous

change of the orifice cannot assure the homogeneity of the experimental condition within all the experimental runs.
The number of experiments is the product between a (3, levels of feed rate), b (3, levels of pressure), c (2, levels of abrasive flow rate), the number of block factors (2) and the number of replicates (4): 144 experiments made possible to determine the best parameters in order to obtain a good quality of the kerf.
**Figure 6.14** shows the machining of the piezoelectric specimen.

**Figure 6.14.:** Machining of the piezoelectric material

## 6.2.4. Validation experiments

The last step of the experimentation consists in validation experiments, as a demonstration of the obtained results after the analysis of the optimization tests. The validation experiments consist in the machining of the case-study actuators described in **Section 4.2**. Two 2-DoF actuators were cut, as shown in **Figure 6.15**: the first one was machined with the optimal parameters, using as abrasive Garnet#200, the second one with the same parameters, using as abrasive Alumina #220. This kind of abrasive particles are finer, so it could be interesting to investigate the different behavior and quality of machined surface. The side effect when using Alumina #220 is the problem of clogging (**Figure 6.16**), that causes frequent machining stops and makes no repeatable the experiments. Further developments and studies about the fluid dynamics of the cutting head are necessary to develop an improved system of abrasive feeding system to industrially use Alumina #220.

a)  b) 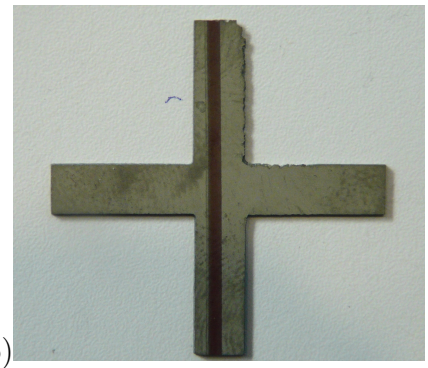

**Figure 6.15.:** The two 2-DoF machined by (a) Garnet#200 and by (b) Alumina#220

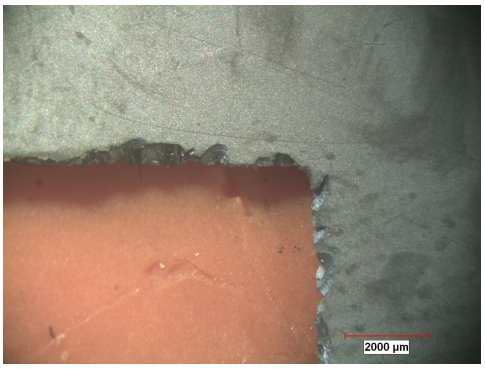


**Figure 6.16.:** An enlargement of the detail machined only by water after the clogging of Alumina#220.

## 6.3. Analysis of results

The quality of the machined surface is the result of four different analysis. Provided that the hypothesis of symmetric kerf (**Figure 6.17**) is verified, the analyzed results are the top kerf width, the bottom kerf width, the kerf taper and the roughness. An optical microscope is used for the analysis of the geometrical kerf dimensions, while a profilometer is used for the roughness analysis. All the technical data of the instruments are presented in **Appendix C**.

### 6.3.1. Kerf quality analysis of the optimization experiments

This section points out the results of the cutting optimization. In the **Appendix A** is possible to find all the data sets, the statistical analysis and the ANOVA's hypothesis verification.

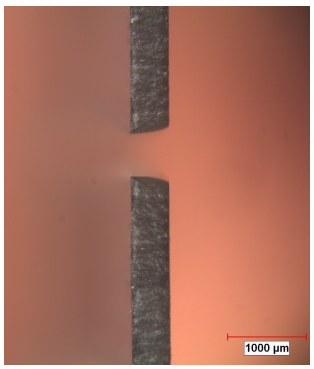


**Figure 6.17.:** The kerf taper is characterized by simmetry

### Top kerf width

The analysis of variances (ANOVA) shows that orifice, abrasive flow rate and feed rate influence the top kerf width, while the pressure is a non-significant parameter (**Figure 6.18**). Also the parameters interactions don't affect the top kerf width (**Figure 6.19**)

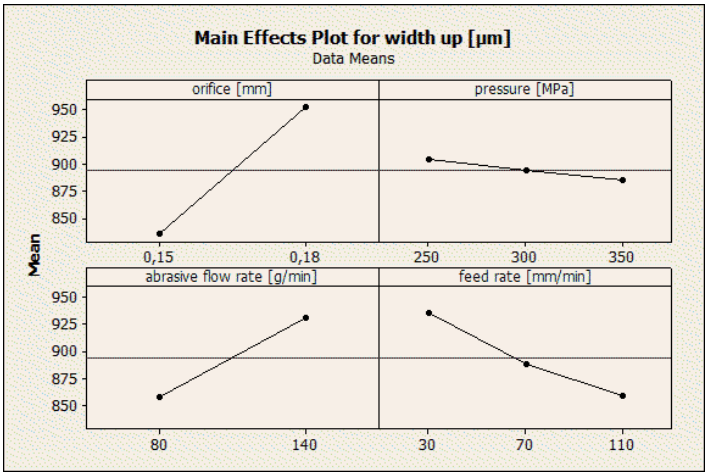


**Figure 6.18.:** The main effects plot for the top kerf width.

Since the aim is having a small width, it's possible to use the multiple comparisons to set the correct level of each parameters: using the Tuckey's test, the orifice of 0,15 mm, abrasive flow rate of 80 g/min, and the feed rate of 110 mm/min are the best parameters. The level of pressure can be chosen arbitrarily. With the best parameters, the width on top of the cut is around 810 µm. In **Table 6.5** all the results of the analysis are shown, and **Figure 6.20** shows the analysis of the top kerf width.

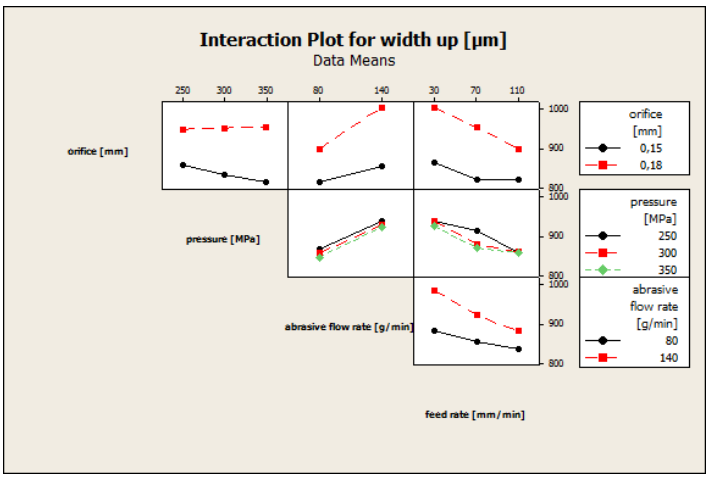


**Figure 6.19.:** The interaction plot for the top kerf width

**Table 6.5.:** Mean value and standard deviaton of top kerf width.

| Parameters | | | | Measurements | |
|---|---|---|---|---|---|
| Orifice [mm] | Pressure [MPa] | Feed rate [mm/min] | Abrasive flow rate [g/min] | Mean [µm] | Standard deviation [µm] |
| 0,18 | * | 30 | 80 | 923,4 | 116,1 |
| 0,18 | * | 70 | 80 | 912,4 | 56,9 |
| 0,18 | * | 110 | 80 | 861,4 | 54,4 |
| 0,18 | * | 30 | 140 | 1068,9 | 90,7 |
| 0,18 | * | 70 | 140 | 997,4 | 58,6 |
| 0,18 | * | 110 | 140 | 935,5 | 39,1 |
| 0,15 | * | 30 | 80 | 835,4 | 59,8 |
| 0,15 | * | 70 | 80 | 796,0 | 67,7 |
| **0,15** | ***** | **110** | **80** | **810,7** | **74,9** |
| 0,15 | * | 30 | 140 | 886,4 | 91,0 |
| 0,15 | * | 70 | 140 | 847,4 | 68,6 |
| 0,15 | * | 110 | 140 | 828,7 | 76,0 |

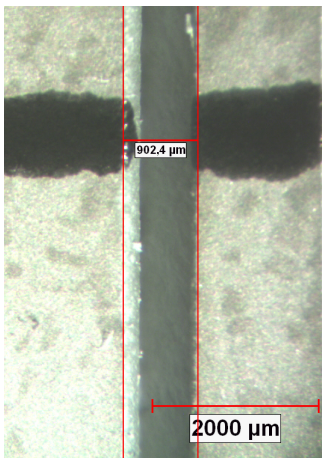


**Figure 6.20.:** The analysis of the machined top kerf width.

### Bottom kerf width

The analysis of variances (ANOVA) shows that orifice, abrasive flow rate and feed rate influence the on bottom kerf width, while pressure is a non-significant parameter (**Figure 6.21**). Also the interactions among the parameters don't affect the bottom kerf width (**Figure 6.22**).

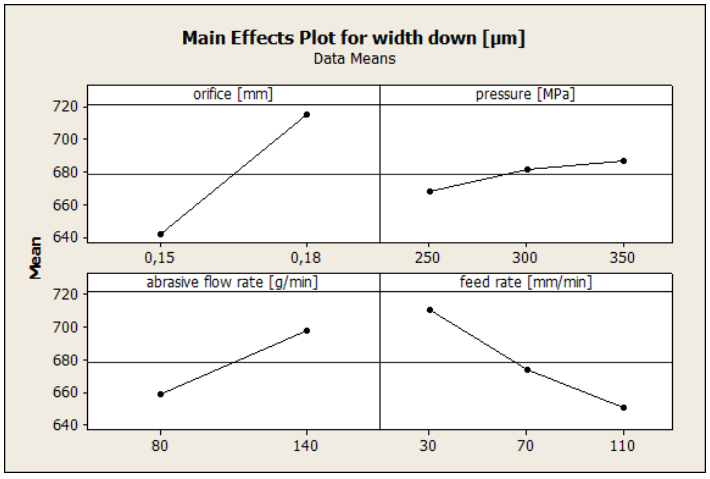


**Figure 6.21.:** The main effects plot for the bottom kerf width.

Since the aim is having a small width, it's possible to use the multiple comparisons to set the correct level of each parameters: using the Tuckey's test, the orifice of 0,15 mm, and the feed rate of 110 mm/min are the best parameters. Since there's no statistical difference between the two levels of abrasive flow rate, it is more economical to set the level of 80 g/min. The level of pressure can be chosen arbitrarily. With best parameters, the width on bottom of the cut is around 625

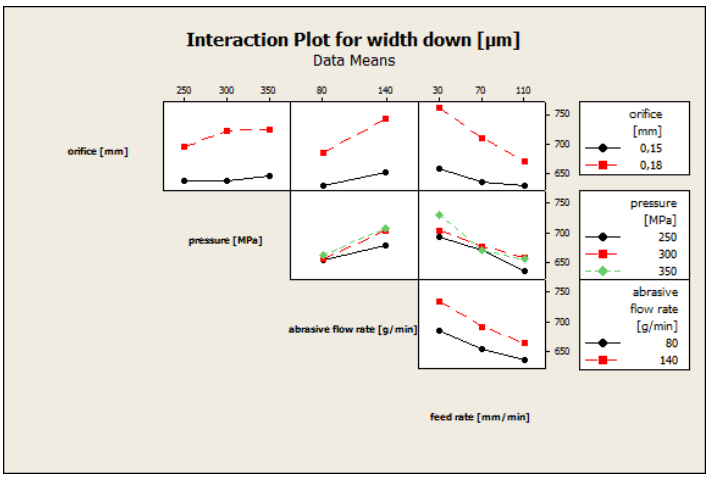


**Figure 6.22.:** The interaction plot for bottom kerf width.

µm. In the **Table 6.6** all the results of the analysis are shown, and **Figure 6.23** shows the analysis of the width on bottom of the cut.

**Table 6.6.:** Mean value and standard deviaton of the bottom kerf width

| **Parameters** | | | | **Measurements** | |
|---|---|---|---|---|---|
| Orifice [mm] | Pressure [MPa] | Feed rate [mm/min] | Abrasive flow rate [g/min] | Mean [µm] | Standard deviation [µm] |
| 0,18 | * | 30 | 80 | 727,7 | 68,2 |
| 0,18 | * | 70 | 80 | 683,7 | 45,9 |
| 0,18 | * | 110 | 80 | 648,6 | 37,9 |
| 0,18 | * | 30 | 140 | 786,5 | 54,1 |
| 0,18 | * | 70 | 140 | 739,0 | 47,7 |
| 0,18 | * | 110 | 140 | 695,0 | 39,1 |
| 0,15 | * | 30 | 80 | 641,0 | 42,9 |
| 0,15 | * | 70 | 80 | 626,1 | 69,9 |
| **0,15** | ***** | **110** | **80** | **624,0** | **89,0** |
| 0,15 | * | 30 | 140 | 673,0 | 67,0 |
| 0,15 | * | 70 | 140 | 646,9 | 40,8 |
| 0,15 | * | 110 | 140 | 635,8 | 59,2 |

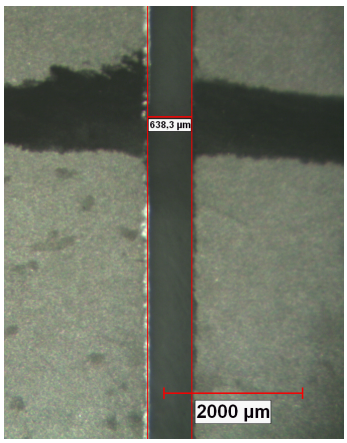


**Figure 6.23.:** The analysis of the machined bottom kerf width.

### Kerf taper

The analysis of variances (ANOVA) shows that orifice, abrasive flow rate and pressure influence the taper of the cut, while feed rate is a nonessential parameter, as shown **Figure 6.24**: this is due to the small thickness of the machined materials. Also the interactions among the parameters don't affect the taper of the cut (**Figure 6.25**).

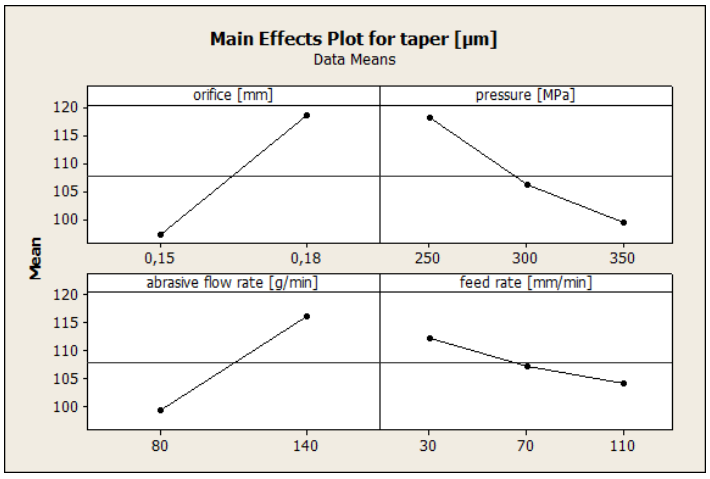


**Figure 6.24.:** The main effects plot for the kerf taper.

Since the aim is having a small taper, it's possible to use the multiple comparisons to set the correct level of each parameters: using the Tuckey's test, there's no statistical difference among the levels of orifice, abrasive flow rate, and pressure. It's possible to choose all the parameters arbitrary. The value of taper is around 100 µm. The most economical choice is than a pressure of 250 MPa and an abrasive flow rate of 80 g/min.

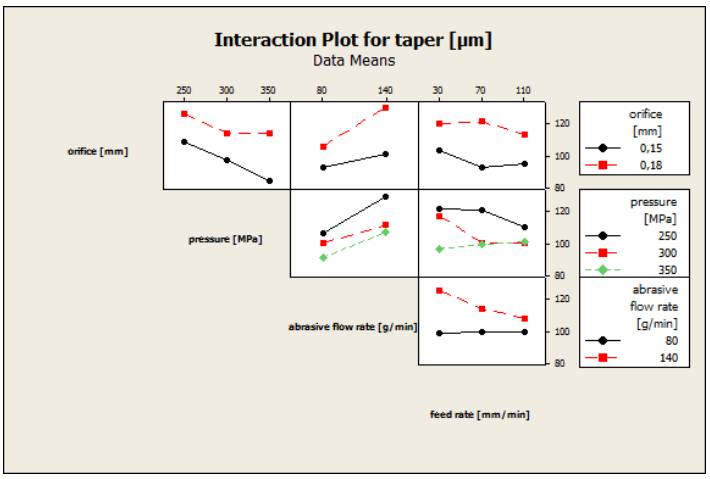


**Figure 6.25.:** The interaction plot for the kerf taper.

The **Table 6.7** shows the mean value and standard deviation of the width on bottom, considering only the parameters that affect the cut.

**Table 6.7.:** Mean value and standard deviaton of the taper of the cut

| **Parameters** | | | | **Measurements** | |
|---|---|---|---|---|---|
| Orifice [mm] | Pressure [MPa] | Feed rate [mm/min] | Abrasive flow rate [g/min] | Mean [µm] | Standard deviation [µm] |
| 0,18 | 250 | * | 80 | 107,1 | 39,8 |
| 0,18 | 300 | * | 80 | 106,4 | 35,6 |
| 0,18 | 350 | * | 80 | 105,1 | 28,9 |
| 0,18 | 250 | * | 140 | 146,3 | 31,3 |
| 0,18 | 300 | * | 140 | 122,7 | 36,8 |
| 0,18 | 350 | * | 140 | 123,5 | 31,9 |
| 0,15 | 250 | * | 80 | 105,6 | 24,0 |
| 0,15 | 300 | * | 80 | 94,7 | 23,5 |
| 0,15 | 350 | * | 80 | 77,5 | 41,0 |
| 0,15 | 250 | * | 140 | 113,1 | 27,2 |
| 0,15 | 300 | * | 140 | 100,9 | 29,4 |
| 0,15 | 350 | * | 140 | 90,9 | 28,2 |

### Roughness

The analysis of the kerf, shows no plastic deformation in the cutting zone: therefore, it is possible to characterize the kerf itself with the roughness (and not waviness), using the profilometer shown in **Figure 6.26**. Given the small dimension of the

piezoelectric ceramic, the cut off is $\lambda = 0.8$ mm for a total length of $5 \cdot \lambda = 4mm$. The cut off is the greatest spacing of respective surface irregularities to be included in the measurement of the average roughness height. It should always be greater than the roughness width in order to obtain the total roughness height rating. The value of the cut off and the total length of evaluation is set using ISO 4288-1996, as shown in **Table 6.8**. For Ra of 2 µm, a cut off of 0,8 mm and a sampling length up to 4 mm are recommended.

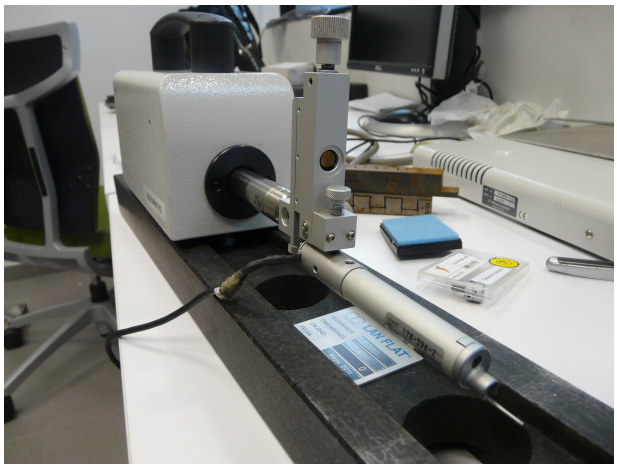

**Figure 6.26.:** The profilometer used during the analysis

**Table 6.8.:** The table of ISO 4288-1996

| **Recommended Cut-off (ISO 4288 - 1996)** | | | | |
|---|---|---|---|---|
| Periodic Profiles | Non-Periodic profiles | | Cut-off | Sampling length / Evalutaion Length |
| Spacing distance (mm) | Rz (µm) | Ra (µm) | λc (mm) | λc (mm) / L |
| > 0,013 - 0,04 | to 0,1 | to 0,02 | 0,08 | 0,08 / 0,4 |
| > 0,04 - 0,13 | > 0,1 - 0,5 | > 0,02 - 0,1 | 0,25 | 0,25 / 1,25 |
| > 0,13 - 0,4 | > 0,5 - 10 | > 0,1 - 2 | 0,8 | 0,8 / 4 |
| > 0,4 - 1,3 | > 10 - 50 | > 2 - 10 | 2,5 | 2,5 / 12,5 |
| > 1,3 - 4 | > 50 | > 10 | 8 | 8 / 40 |

The analysis of variances (ANOVA) shows that orifice and feed rate influence the roughness while pressure and abrasive flow rate are nonessential parameters, as shown in **Figure 6.27**. The interactions are not significative, as shown in **Figure 6.28**.

Since the aim is having a small roughness, it's possible to use the multiple comparisons to set the correct level of each parameters: using the Tuckey's test, the orifice

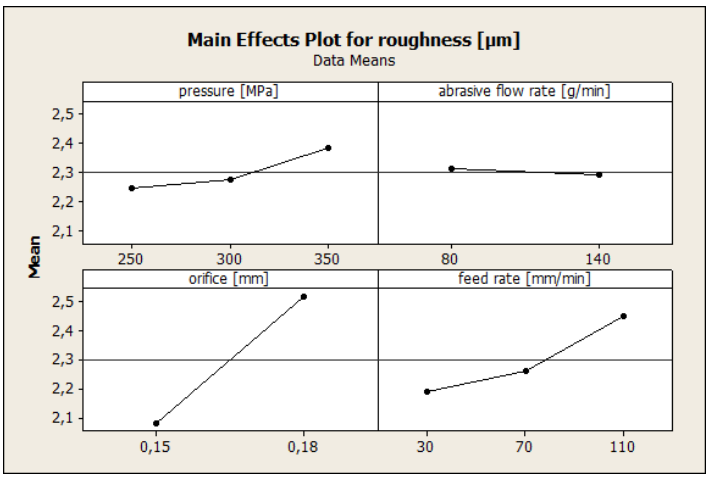


**Figure 6.27.:** The main effects plot for the roughness.

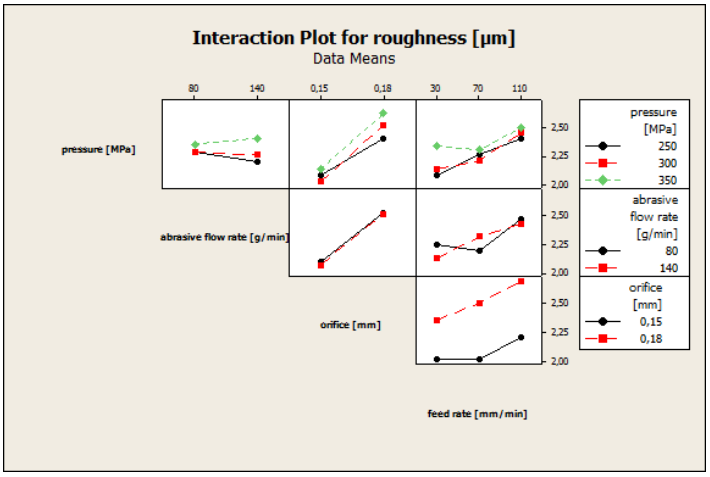


**Figure 6.28.:** The interaction plot for the roughness.

of 0,15 mm, is the best parameters. The feed rate optimal range is between 30 and 70 mm/min. Since there's no statistical difference between the levels of abrasive flow rate, it is appropriate to set the level of 80 g/min due to economic reasons. The level of pressure can be chosen arbitrarily, but a pressure of 250 MPa is more suitable because it stresses less the system. Machining with optimized parameters, the final roughness is around 2 µm. The **Table 6.9** shows the mean value and standard deviation of the width on top, considering only the parameters that affected the cut, and **Figure 6.29** shows an example the output of the program to measure the roughness.

Pressure doesn't have an influence because for cutting 0,5mm-thick material an high level of energy is not required. Abrasive flow rate doesn't influence the results because of the fragile nature of the piezoelectric material: when the brittle fractures start, it's impossible to control them with a correct regulation of the abrasive flow

**Table 6.9.:** Mean value and standard deviaton of the roughness

| Parameters | | | | Measurements | |
|---|---|---|---|---|---|
| Orifice [mm] | Pressure [MPa] | Feed rate [mm/min] | Abrasive flow rate [g/min] | Mean [µm] | Standard deviation [µm] |
| 0,18 | * | 30 | * | 2,35 | 0,43 |
| 0,18 | * | 70 | * | 2,50 | 0,41 |
| 0,18 | * | 110 | * | 2,70 | 0,36 |
| 0,15 | * | 30 | * | 2,02 | 0,33 |
| 0,15 | * | 70 | * | 2,01 | 0,34 |
| 0,15 | * | 110 | * | 2,20 | 0,32 |

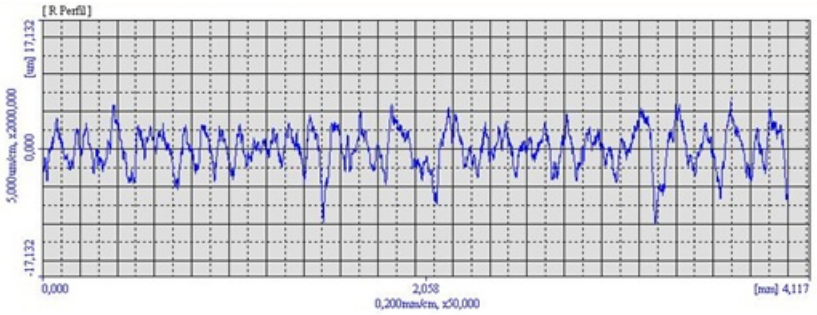


**Figure 6.29.:** An example of the program output for roughness measurement.

rate. The orifice diameter is a significant parameter because it probably makes more coherent the jet, and it has a good effect on the surface quality. The jet close to the kerf machines a smooth surface, but a too long permanence could cause scratches: so the optimal level of feed rate is probably 70 mm/min.

### 6.3.2. Results summary of optimization experiments

Significant parameters pointed out from optimization experiments are shown in **Table 6.10**.

**Table 6.10.:** Significant parameters.

| | Orifice | Pressure | Feed rate | Abrasive flow rate |
|---|---|---|---|---|
| Top kerf width | X | | X | X |
| Bottom kerf width | X | | X | X |
| Kerf taper | X | X | | X |
| Kerf Roughness | X | | X | |

Suggested optimale value of each parameters are shown in **Table 6.11**.

**Table 6.11.:** Optimal parameters.

| | Orifice [mm] | Pressure [MPa] | Feed rate [mm/min] | Abrasive flow rate [g/min] |
|---|---|---|---|---|
| Top kerf width | 0,15 | 250 | 110 | 80 |
| Bottom kerf width | 0,15 | 250 | 110 | 80 |
| Kerf taper | 0,15 | 350 | 110 | 80 |
| Kerf Roughness | 0,15 | 250 | 70 | 80 |

### 6.3.3. Kerf surface quality in validation experiments

The quality of machined surface of the 2-DoF actuators is evaluated only in terms of roughness. The **Table 6.12** shows a brief summary of the results.

**Table 6.12.:** Mean value and standard deviaton of kerf roughness.

| **Parameters** | | | | | **Measurements** | |
|---|---|---|---|---|---|---|
| Orifice [mm] | Pressure [MPa] | Feed rate [mm/min] | Abrasive flow rate [g/min] | Kind of abra-sive | Mean [µm] | Standard devia-tion [µm] |
| 0,15 | 250 | 70 | 80 | Garnet #200 | 2,35 | 0,22 |
| 0,15 | 250 | 70 | 80 | Alumina #220 | 1,40 | 0,08 |

The validation experiments confirm the conclusion obtained with the optimization experiments: the best parameters to work piezoelectric ceramic are orifice of 0,15 mm, pressure of 250 MPa, feed rate of 70 mm/min and abrasive flow rate of 80 g/min. Due to the dimension of the abrasive particles, the surface machined with Alumina#220 shows a better surface quality, probably due to the dimension of the abrasive particles. Moreover, being the standard deviation of Alumina#220 smaller than the standard deviation of Garnet#200, the process shows a high repeatability. Finer particles have good results also in terms of precision and dimension accuracy, as shown in **Figure 6.30.** Another good effects of Alumina#220 is on the chipping that is evident in the machined back side of Garnet#200, as shown in **Figure 6.31**.

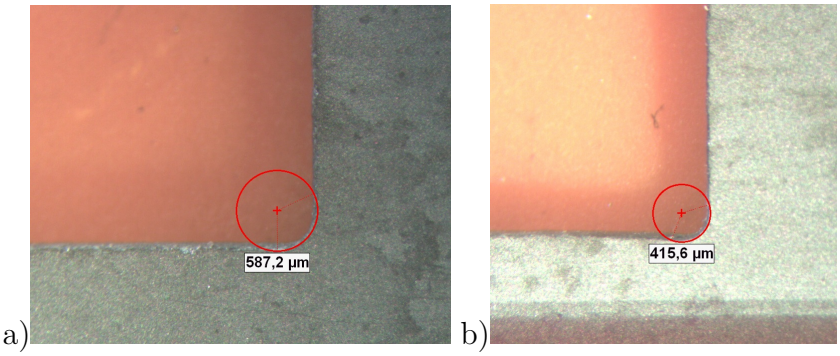


**Figure 6.30.:** Angles machined by Garnet#200 (a) and by Alumina#220

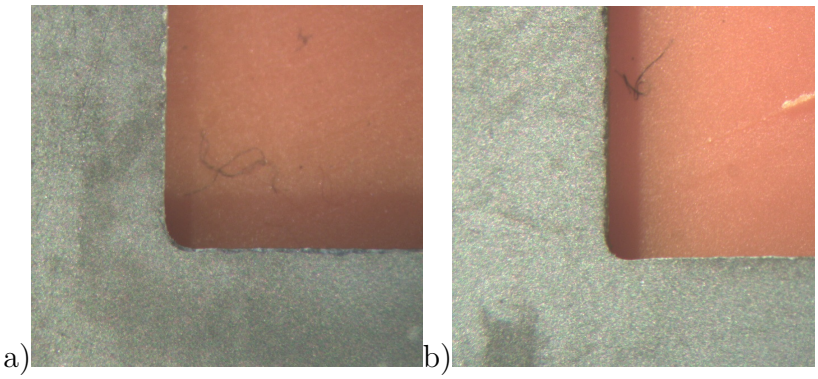


**Figure 6.31.:** Back side machined by Garnet#200 (a) and by Alumina#220

### 6.3.4. Scanning electron microscope analysis

In order to understand more deeply the machining mechanism and the influence of the process parameters on it, a further analysis of the kerf surface is carried out at Politecnico di Milano by means of a SEM (scanning electron microscope, datasheet in **Appendix C**). The specimens have to be treated, because a SEM analysis is possible only with a conductive material: the process of gold-plating allows to analyze this non-conductive ceramic material. The **Figure 6.32** shows that the structure is inhomogeneous, with the typical shape of the material produced by powder manufacturing. It's possible to distinguish clearly the powder grains and to evaluate the grains dimensions, that are around 2 µm.

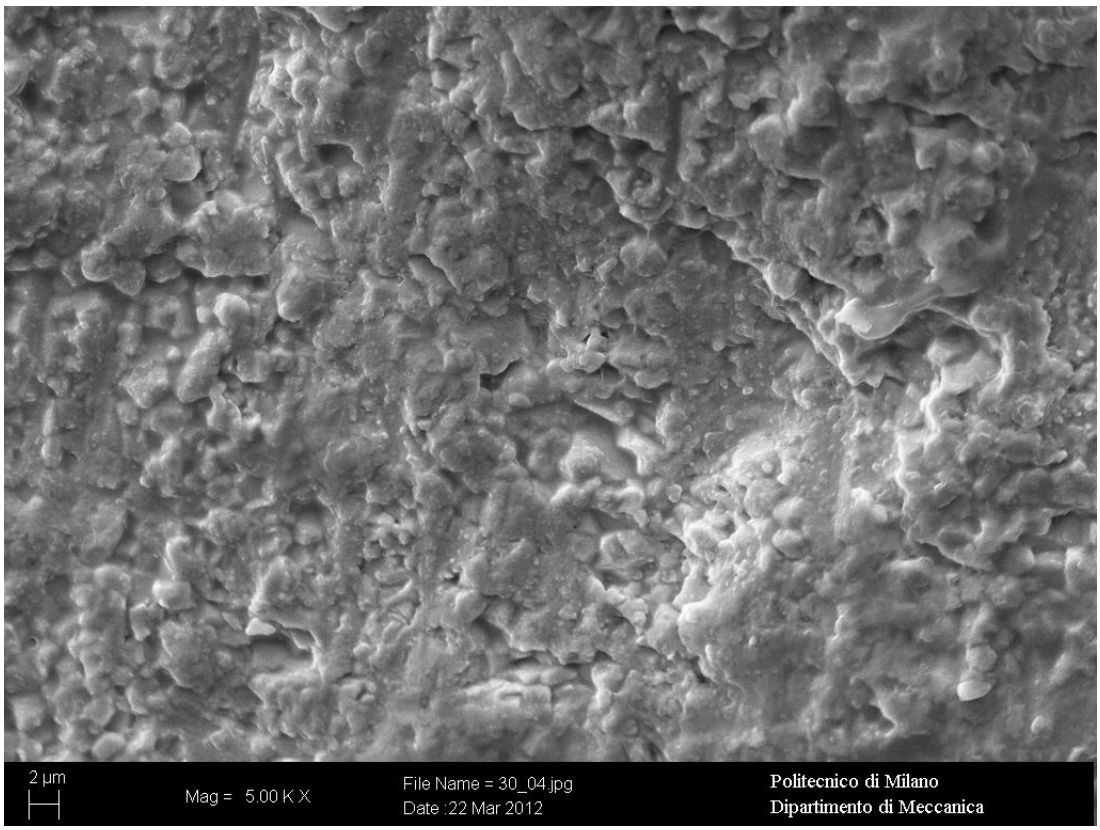


**Figure 6.32.:** The kerf structure of the PZT material with an enlargement of 5.000X.

The **Figure 6.33** shows the material removal mechanism is characterized by brittle fractures among powder grains, but there are also tracks of ductile fractures. A ductile fracture is more desirable because the process is more regular and it's possible to control more easily with a parameters optimization. The generated friction heat will enter the bodies through these asperities, leading to very high local temperatures, often higher than 1000°C: the high local temperatures generated at the ceramic surface can cause thermal stresses and reactions which may promote thermal wear processes, such as: thermal spalling, thermal cracking, plastic deformation, formation of grain boundary cavities [44]. The very high temperatures generated at the exposed surface may lead to a transition from brittle to ductile behaviour of the ceramic. This phenomenon could partly explain the observed presence of plastically deformed wear surfaces after AWJ machining of piezoceramics.
A common characteristic in all the specimen at difference feed rate is the presence of embedded abrasive particles in the ceramic matrix, as shown in **Figure 6.34**. The shape of the particle is sharp and irregular and the dimension is smaller than the nominal dimension. However, it's not possible to determine how much of the fragmentation has occured at different stages of the process, for example during particle acceleration, particle contact with mixing tube and specimen: probably, this is due

to the fact that they are crumbled during the cutting process since the hardness of the piezoelectric material is comparable to the abrasive one.

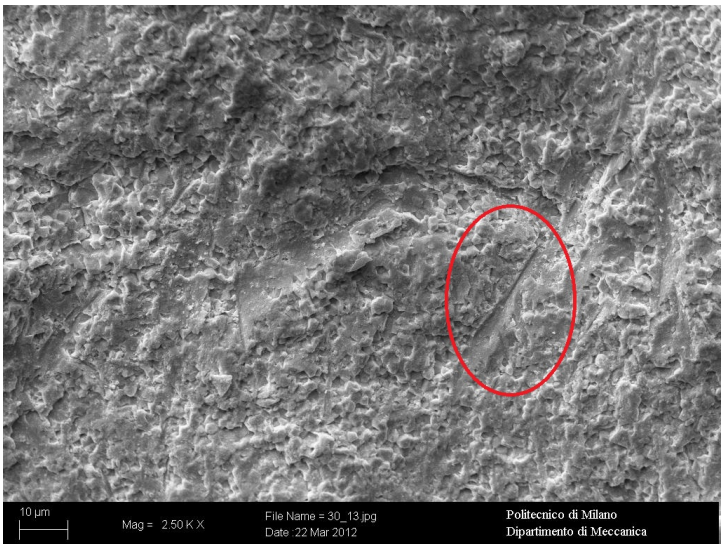


**Figure 6.33.:** The brittle fracture is dominant, but there are also tracks of ductile fracture.

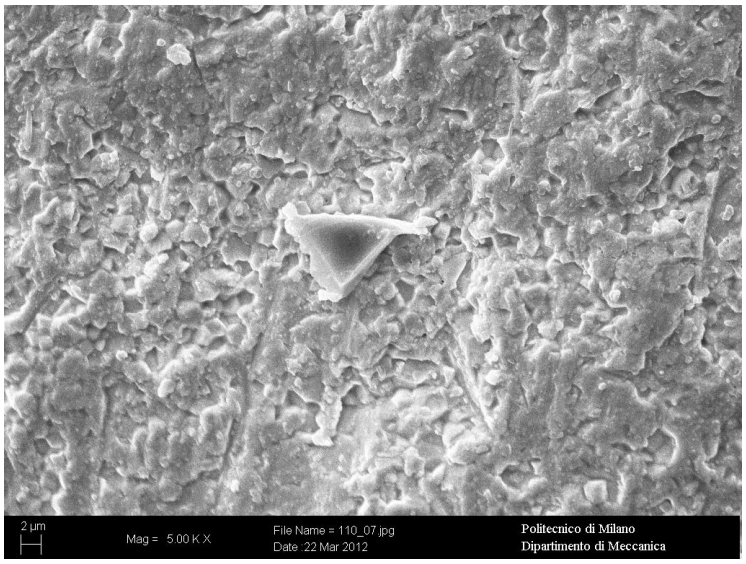


**Figure 6.34.:** An abrasive particle embedded in the ceramic material.

The SEM images are taken at the middle of the kerf, in order to avoid the entrance and exit zone: particularly, the exit zone is characterized by chipping, that is an irregular phenomenon present in all the specimens. Analyzing the images in **Figure 6.35**, there is no evident differences between the kerf surface at the different feed rates: the structure looks like irregular in all the cases.

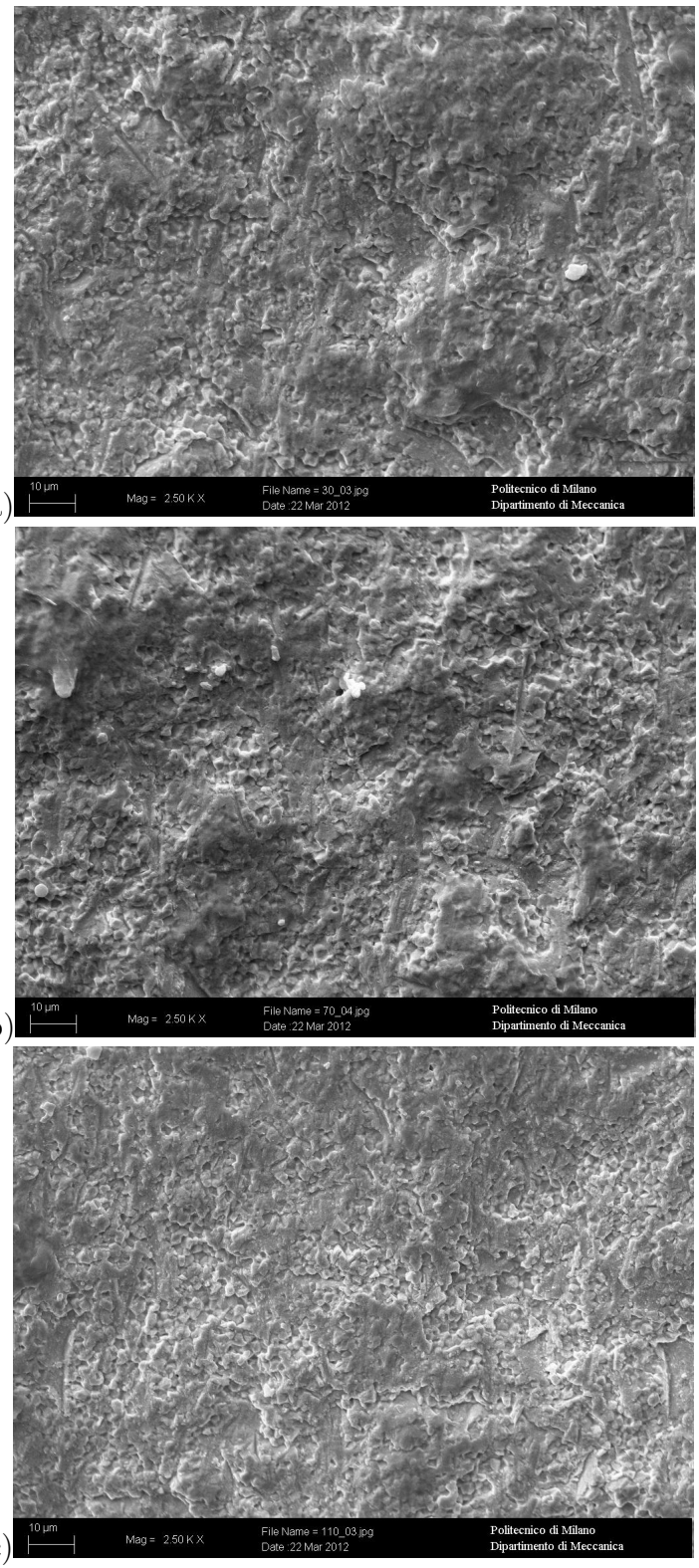


**Figure 6.35.:** Enlargement of 2.500X for different feed rate: a) 30 mm/min; b) 70 mm/min; c) 110 mm/min

The material was not cleaned before the analysis in order to not affect the machined kerf and to not remove the abrasive particles: due to this fact, many organic residuals are also present on the kerf surface and it is rather difficult to distinguish them from the abrasive particles. For this reason, a further chemical analysis is necessary to detect the particles. The results are shown in **Figure 6.36** and **Table 6.13**: elements like Pb and Ti are typical of the piezo-ceramic material composition, while the presence of high percentages of Si, Fe, Al and O identifies unquestionably the abrasive particles. The X-Ray analysis of the piezoceramic material of the machined areas shows that it doesn't contain Fe, Si, Al and O, originating from the abrasive medium. The absence of these elements implies that the abrasive doesn't involve a chemical reaction with the ceramic. Probably, the chemical analysis of the areas characterized by ductile fractures could demonstrate the abrasive involves reaction and oxidation of the piezoceramic. Another important consideration is about the dimension of the piezoelectric grains, that are smaller than the dimension of the abrasive particles: this means that working with a finer abrasive probably makes possible to improve the quality, because the machined surfaces would be more regular. This is agreed with the results of validation experiments, that show the surface quality is better for Alumina#220 than for Garnet#200.

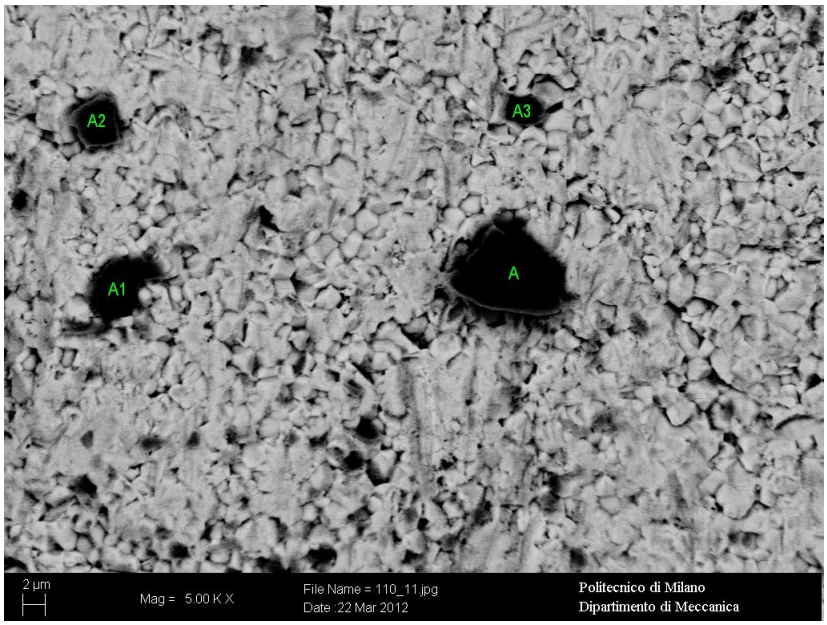


**Figure 6.36.:** The chemical analysis of the abrasive particles

### 6.3.5. Post - Anova analysis: the Pearson - Hartley charts

The Pearson–Hartley charts can be used as a post-hoc statistical power analysis, conducted after a study has been completed. Briefly, using the sample size and the

**Table 6.13.:** Chemical analysis of the abrasive particles embedded in the machined kerf

| **Material** | **Elements** | | | | | | | | |
|---|---|---|---|---|---|---|---|---|---|
| Garnet #200 | $SiO_2$ 35% | $FeO$ 33% | $Al_2O_3$ 23% | $MgO$ 7% | $CaO$ 1% | $MnO$ 1% | | | |
| Abrasive particle | $Si$ 22,4% | $Fe$ 25,5% | $Al$ 12,9% | $Mg$ 3,3% | $Ca$ 0,9% | $Mn$ 0,9% | $O$ 33,8% | $Pb$ 0,3% | $Ti$ 0,1% |

effect size, it is possible to determine which is the statistical power of the carried out analysis, assuming that the effect size in the sample is equal to the effect size in the population. A complete theoretical review is presented in **Appendix B**.
In the present power analysis, the roughness is considered the parameter to detect: the orifice diameter and the feed rate are the only parameters that affect it, as demonstrated by the ANOVA analysis
The statistical power is shown in **Figure 6.37** and it is 41%.
The value of the power is small, because normally the value is around 90%. Generally, when the analysis aims to detect small effects, more replicates are required and so a higher number of experimental runs. In the present study where 4 replicates were performed, it is difficult to detect small variations on roughness caused by the influence of orifice and feed rate, because the differences between different levels are very small with a slightly large standard deviation.

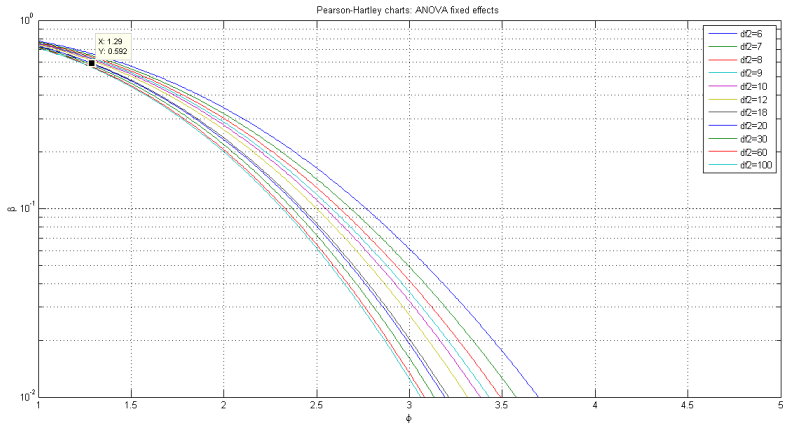


**Figure 6.37.:** Pearson – Hartley charts for the calculation of the analysis power.

With the actual power value it is possible to detect a difference between the levels of 0,6 µm. The value of the power is confirmed also by the analysis made by the software Minitab ®. The results are shown in **Figure 6.38**.

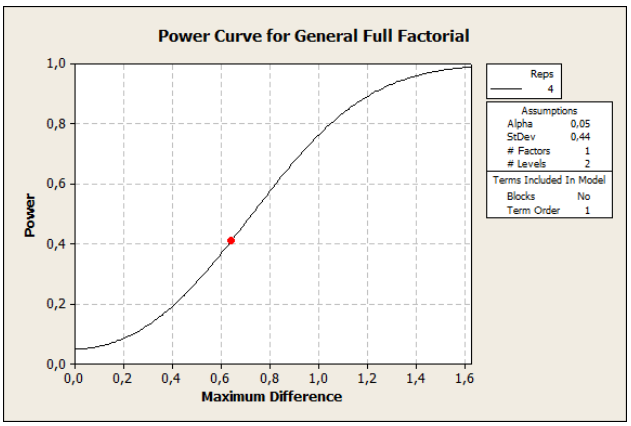


**Figure 6.38.:** Calculation of the maximum detectable difference due to the power.

Knowing the difference and assuming that the value of the specimens standard deviation as representative of the populations, it is possible to estimate how many replicates are necessary to have a power of 90%: the result (**Figure 6.39**) is that 8 replicates are necessary, which means 288 experiments.
The aim of this experimentation is a first optimization, so it is not interesting to detect differences in the order of 0,1 µm among the different levels of each factors: from this point of view, a great experimental efforts is not justified, so 4 replicates is the more reasonable compromise.

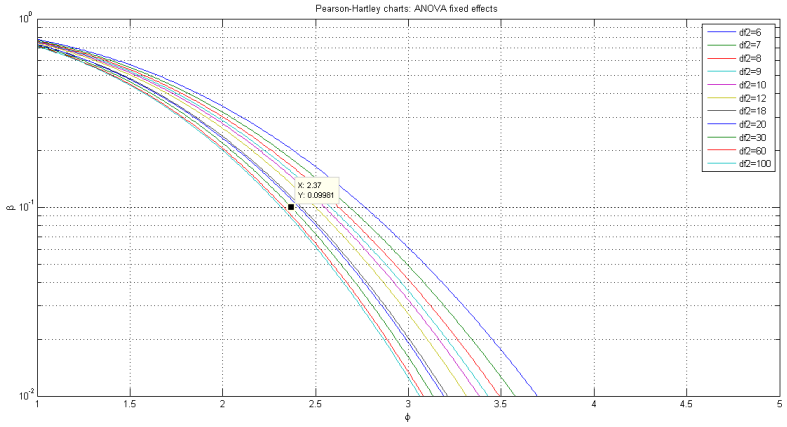


**Figure 6.39.:** Pearson – Hartley charts for the calculating of the sample size, setting a power of 90%

# 7. CONCLUSIONS AND FUTURE DEVELOPMENTS

In scientific literature, there are few papers which deal with the argument of this work: this thesis work could be a starting point for enhancing machining with fine water jet of piezoelectric material, and to get aware a better understanding of the problems linked to parameters optimization.
Some future developments could be the fine water jet cutting and milling of hard piezoceramics and piezocomposites. There is a growing interest in this new category of materials applied to several different fields and, consequently, there is a lot of reasons to study and improve their machining process.

## 7.1. Conclusions

The three main reasons that make fine abrasive water jet an appealing technology in the field of piezoelectric ceramics are the extreme flexibility with short manufacturing time, the relatively low costs and, above all, the reduction or even the absence of mechanical and thermal stresses.
The kerf quality is evaluated in terms of kerf width and roughness: smaller kerf width (less than 1 mm) are important to minimize the scraps (piezoelectric is a valuable and expensive material) and allows to machine features of small dimensions. The roughness is more important, being strictly linked to the material mechanical strength and because of the presence of craters is a source of cracks and fractures. Moreover, the micro final applications requires implicitly high dimensional precision and a very smooth kerf.

The statistical approach made it possible to determine that the best process parameters to work with are an orifice of 0,15 mm and a feed rate of 30 or 70 mm/min, while the values of pressure and abrasive flow rate are not significant. The jet close to the kerf has a good smoothing effect, but a too long permanence could cause scratches and craters. So, for the experimenter, the best value for the feed rate is 70 mm/min.
Since a 0,5mm-thick piezoelectric material does not require a high cutting energy to be machined ,the pressure is a non-significant parameter: in order to reduce the mechanical stresses on the workpiece and reduce the costs, the best pressure level is 250 MPa.
A common feature in all the specimens is a major integrity of the material at the entrance of the jet. At the entrance the kerf is regular while at the exit it is characterized by several craters whose dimensions are typically less than 100 µm. Along the kerf thickness two main machining mechanisms are present: the kerf upper side of the material is mainly subjected to compression which is a good working condition for hard brittle ceramics, while towards the bottom side where the jet approaches the exit from the kerf, there are adverse tensile stresses that enhance fragile fractures and craters for this materials, as shown in **Figure 7.1**.

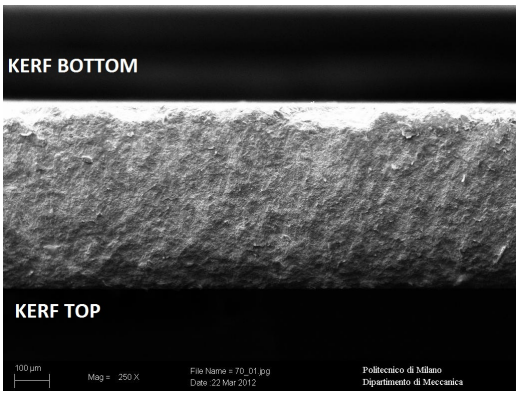


**Figure 7.1.:** The structure of the specimen at the exit is characterized by chipping.

The fixturing system has probably an influence on this phenomenon: the polystyrene is perfect in avoiding the jet rebounding that could damage the material, but it isn't so rigid. Different materials could be more adequate as support: for example, Plexiglas is more rigid than polystyrene and can offer a more rigid support providing the same protection to water rebounding. **Figure 7.2** shows the machined kerf and the typical chipping of brittle materials.

Abrasive flow rate doesn't influence the quality of the kerf: this is an unexpected effect, because increasing the abrasive flow rate, the roughness usually decreases. This effect is strictly linked to the material, that isn't homogeneous, as shown in the SEM analysis in **Section 6.3**: the mechanical remove mechanism of a brittle material is characterized by fractures along the "powder boundaries", so it's impossible to improve the roughness beyond the limits of the material. When the brittle

a) 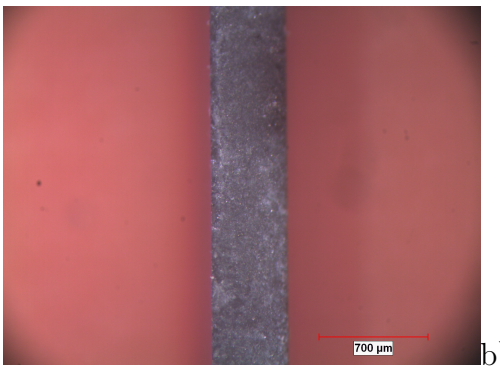

b) 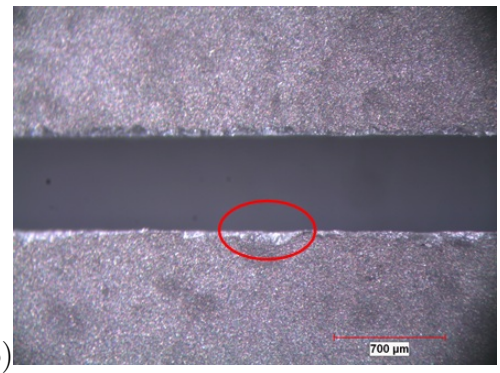


**Figure 7.2.:** The chipping phenomenon in piezoelectric material: a) it's evident that the entrance of the jet is on the right side; b) on the bottom side there are considerable craters, as highlighted in the red circle

fracture starts, it's not possible to stop or control it by regulating the abrasive flow rate. The abrasive hardness and particle size deeply influence the roughness: in the fragile fracture, the hardness is the most important parameter, because the abrasive particle breaks in a more regular way the piezoelectric material. As a matter of fact, the technologic optimization of water jet parameters reduces the roughness in a smaller way than the kind of abrasive. The hardness of the Garnet is around 7,5-8 Mohs, while the hardness of the Alumina is around 9 Mohs: a bigger hardness can machine better the material, as shown in the experiments of validation. Moreover, the abrasive particle size is around 0,075 mm for Garnet (#200) and around 0,066 mm for Alumina (#220): this could have an influence, knowing the dimension of the piezoelectric powder. In **Figure 7.3** is shown the machined kerf.

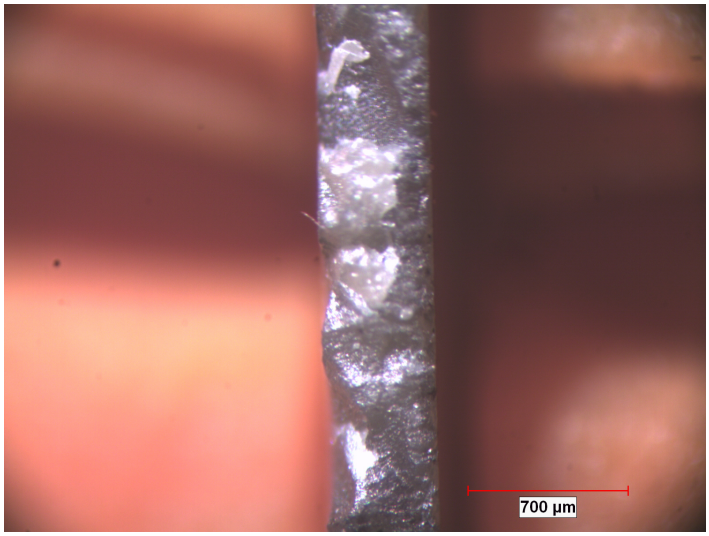


**Figure 7.3.:** The "cracking among powder particles" is the typical fracture mode of piezoelectric ceramic.

## 7.2. Future developments

It's impossible to divide the improvement of material performance from the machining technology and the final applications. Materials and machining technology have to be developed at the same time. It's important to find an economical machining technology because improved materials have a high price of manufacturing: the exploration of new research horizons can be supported by an innovative machining technology, but at the same time this has to be supported by new applications. Fine abrasive water jet represents an attractive technology due to the above mentioned reasons when machining hard piezoceramics and in the case of milling piezoceramics.

### 7.2.1. Fine abrasive water jet machining of hard piezoceramics

Hard piezoelectric materials have better properties than soft piezoelectric materials, but they are much more difficult to machine. These problems are due to their Curie temperature, which is on average around 150°C, because there are changes in piezoelectric properties at the temperature of 100°C. It's impossible to machine this kind of material with laser or EDM without affecting their piezoelectric properties, at least close to the machined surface (see **Section 4.3**). Water jet represents probably the best technology to machine hard piezoelectric materials without altering them.

### 7.2.2. Fine abrasive water jet milling of piezocomposites

There are several practical limitations to implementing piezoceramics, namely the brittle nature of ceramics makes them vulnerable to accidental breakage during handling and bonding procedures, as well as their extremely limited ability to conform to curved surfaces and the large add-on mass associated with using a typically lead-based piezoceramic. The idea of a composite material consisting of an active piezoceramic fibrous phase embedded in a polymeric matrix phase solves many of the aforementioned restrictions.
Typically, crystalline materials have much higher strengths in the fiber form, where the decrease in volume fraction of flaws leads to an increase in specific strength. Moreover, in addition to protecting the fibers, the flexible nature of the polymer matrix allows the material to more easily conform the curved surface found in more realistic industrial applications [45].
In conclusion, the active fibers offer many advantages over traditional monolithic piezoelectric devices such as increased actuation authority, flexibility and the ability to impose twisting deformation onto a structure.
Smart Material Corp. manufactures this composite material, which contains piezoelectric rods embedded in a polymer matrix and aligned through the thickness of the device. **Figure. 7.4** ([45])shows this type of device where the active pixels

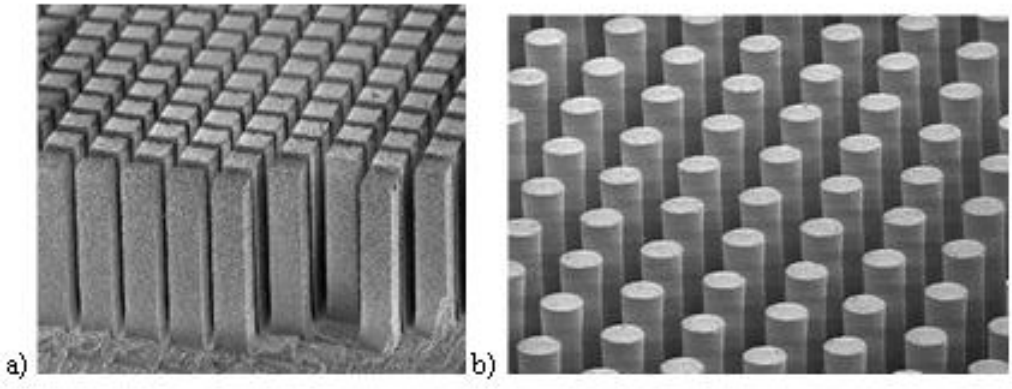


**Figure 7.4.:** Composites by Smart Materials Corp: a) rectangular fibers, b) round fibers.

can be either rectangular (80 micron with 120-micron spaces) or round (70 micron diameter with 50-micron spaces).

Nowadays, these devices are manufactured using a patented soft-mold technology: this process consists simply of copying a soft mold from a positive form of the final structure, filling the mold with piezoceramic material and subsequent firing of the element. This process holds many advantages over conventional die-and-fill, injection molding or dicing techniques. First, the molds are re-usable, thus allowing thousands of copies to be made of the original form with a single soft mold. While some configurations could be made by dicing the desired final shape from a monolithic piezoceramic block, the soft-molding process alleviates the need for such expensive cutting machinery[45].
The two principal disadvantages of piezoelectric fiber composite technology are the difficulty of processing and handling expensive piezoceramic fibers during actuator manufacture, and the high actuator voltage requirements. Piezoelectric fiber composites have typically employed high cost, extruded, round piezoceramic fibers.
Water jet is very attractive technology in this field of applications for many reasons. First of all, the dimension of the jet is compatible with the dimension of the spaces between rods (600 micron jet diameter and 120 micron spaces), so this technology is capable to machine these features. Moreover, the water jet technology is flexible and cost-efficient, so it is possible not to have a mold for every rod shape. Nowadays, water jet technology is not still used, but there are many experimental efforts to industrialize this appealing technology. Water jet milling and cutting are the field of research in which major efforts are necessary.
Some attempts of water jet milling for these applications were performed at Tecnalia R&I and the results are shown in **Figure 7.5** and **Figure 7.6**. The parameters are choosen from the previous experimentations, knowing the behaviour of the piezoceramic materials.

**Figure 7.5.:** The fixturing system is composed by polystyrene and sellotape

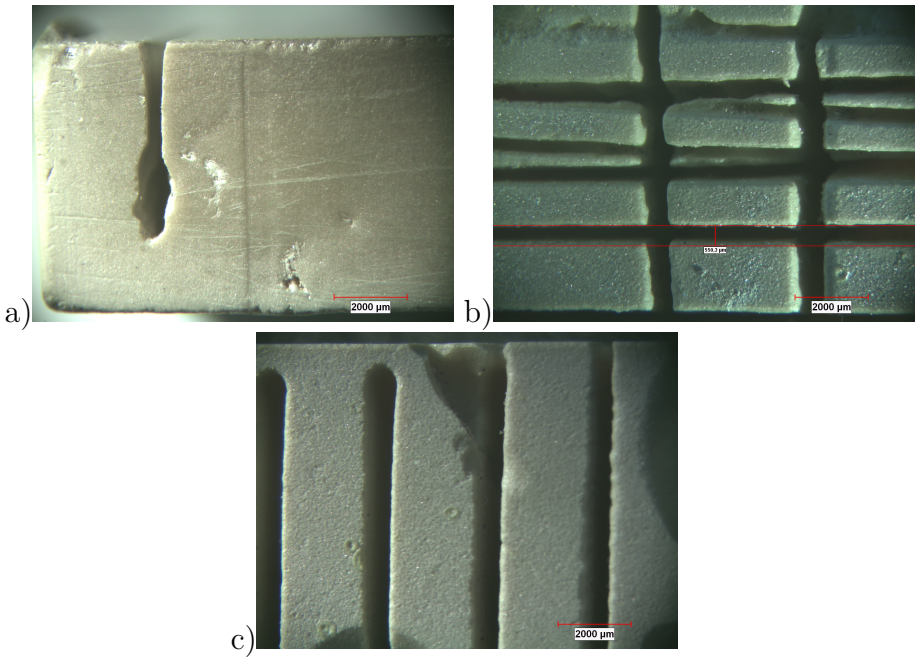


**Figure 7.6.:** Milling attemps at p=200 MPa and v=600 mm/min. In the case of clogging abrasive or too high forces the brittle behaviour of the material is evident, with the typical macro craters.

The biggest problem in these first attempts is the fixturing system: the polystyrene is too soft and affects the quality of the kerf, and the sellotape is machined by water and it doesn't fix the piezoelectric specimen. A possible solution is to glue the piezoelectric specimen to a Plexiglas sheet, as shown in **Figure 7.7**. The final parts is shown in **Figure 7.8** and **Figure 7.9**: after few attempts, the machined test

specimen has already a good quality surface, offering new opportunities for further investigation on this application.

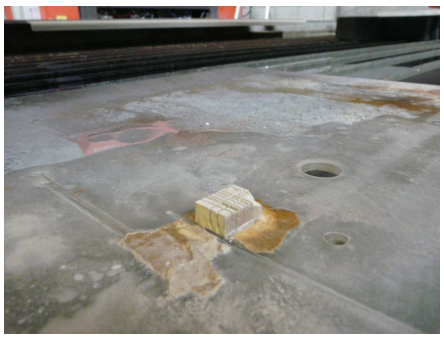

**Figure 7.7.:** The fixturing system is composed by a metallic bar and glue

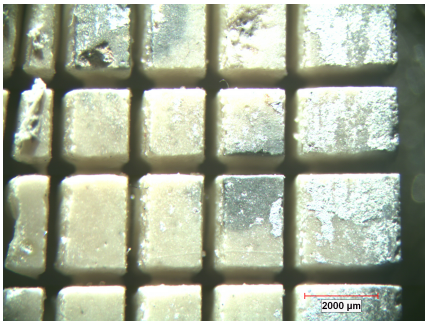


**Figure 7.8.:** An enlargement of 15x of the specimen, machined with pressure 200 MPa, feed rate 1000 mm/min, Garnet#200 and abrasive flow rate 80 g/min

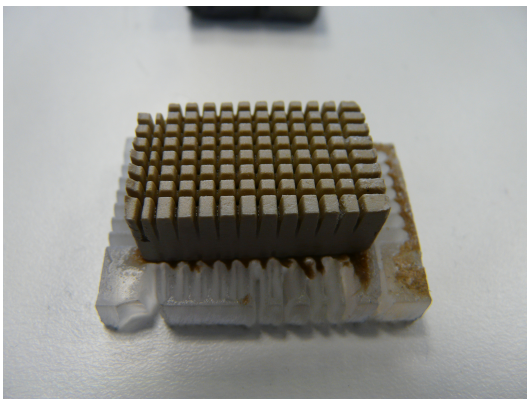

**Figure 7.9.:** The specimen machined by fine abrasive water jet technology

# Acknowledgments

I wish to thank my family for the support they provided me through my entire life and in particular, I must acknowledge my girlfriend Micol, without whose love and encouragement, I would not have finished this thesis.

I would like to express my gratitude to my supervisor Ing. Massimiliano Annoni and my tutor Dr. Francesco Arleo, for their technical and lovely collaboration.

A very special thanks goes to Dr. Alfredo Suarez, the "philospher" (and also the best football player in Spain), and Tecnalia's team, for their technical support, motivation and encouragment.

I wish to thank Fernando for his "paella" and his lessons of Spanish language and culture.

I also wish to thank all the people and friends who share their time in these five years.

In conclusion, I recognize that this research has been possible with the economic support of Tecnalia R&I.

# A. EXPERIMENTAL DATA

## A.1. Optimization experiments

In this section all the experiments data and the analysis of the results are presented. All the investigated variables are analysed with the statistical technique called ANOVA (analysis of variances). In **Table A.1** all the data and the results are shown.

**Table A.1.:** Experimental data.

| running order | orifice [mm] | pressure [MPa] | abrasive flow rate [g/min] | feed rate [mm/min] | width on top [µm] | width on bottom [µm] | taper [µm] | roughness [µm] |
|---|---|---|---|---|---|---|---|---|
| 1 | 0,18 | 250 | 80 | 70 | 917,4 | 697 | 110,2 | 2,416 |
| 2 | 0,18 | 300 | 140 | 110 | 990,7 | 726,3 | 132,2 | 3,017 |
| 3 | 0,18 | 350 | 80 | 110 | 814,4 | 550,3 | 132,1 | 3,044 |
| 4 | 0,18 | 250 | 140 | 70 | 1020 | 726,3 | 146,8 | 2,388 |
| 5 | 0,18 | 300 | 80 | 30 | 976,5 | 741 | 117,7 | 3,107 |
| 6 | 0,18 | 350 | 140 | 110 | 976,5 | 682,7 | 146,9 | 2,709 |
| 7 | 0,18 | 250 | 80 | 30 | 917,4 | 756 | 80,7 | 2,474 |
| 8 | 0,18 | 300 | 140 | 70 | 1005 | 741,3 | 131,8 | 3,149 |
| 9 | 0,18 | 350 | 80 | 70 | 931,8 | 697,3 | 117,2 | 2,713 |
| 10 | 0,18 | 250 | 140 | 110 | 917,4 | 668,7 | 124,3 | 2,836 |
| 11 | 0,18 | 300 | 80 | 110 | 903,2 | 653,3 | 124,9 | 2,641 |
| 12 | 0,18 | 350 | 140 | 30 | 1168 | 800,5 | 183,7 | 3,154 |
| 13 | 0,18 | 250 | 80 | 110 | 887,7 | 638,5 | 124,7 | 1,793 |
| 14 | 0,18 | 300 | 140 | 30 | 1137 | 755,7 | 190,6 | 1,926 |
| 15 | 0,18 | 350 | 80 | 30 | 1050 | 771,2 | 139,4 | 2,21 |
| 16 | 0,18 | 250 | 140 | 30 | 1138 | 757,4 | 190, | 2,047 |
| 17 | 0,18 | 300 | 80 | 70 | 888,5 | 756,6 | 65,9 | 2,464 |
| 18 | 0,18 | 350 | 140 | 70 | 1020 | 771,2 | 124,4 | 2,648 |
| 19 | 0,18 | 250 | 80 | 70 | 976 | 682,7 | 146,6 | 2,059 |
| 20 | 0,18 | 300 | 140 | 110 | 934 | 729,3 | 102,3 | 2,715 |
| 21 | 0,18 | 350 | 80 | 110 | 949,9 | 685,5 | 132,2 | 2,678 |
| 22 | 0,18 | 250 | 140 | 70 | 1053 | 685,5 | 183,7 | 3,633 |

| running order | orifice [mm] | pressure [MPa] | abrasive flow rate [g/min] | feed rate [mm/min] | width on top [µm] | width on bottom [µm] | taper [µm] | roughness [µm] |
|---|---|---|---|---|---|---|---|---|
| 23 | 0,18 | 300 | 80 | 30 | 1020 | 770,4 | 124,8 | 2,444 |
| 24 | 0,18 | 350 | 140 | 110 | 917,4 | 697 | 110,2 | 3,278 |
| 25 | 0,18 | 250 | 80 | 30 | 1108 | 755,7 | 176,1 | 2,891 |
| 26 | 0,18 | 300 | 140 | 70 | 1109 | 785 | 162 | 2,283 |
| 27 | 0,18 | 350 | 80 | 70 | 991,5 | 711,7 | 139,9 | 2,459 |
| 28 | 0,18 | 250 | 140 | 110 | 1065 | 653 | 206 | 2,445 |
| 29 | 0,18 | 300 | 80 | 110 | 903,9 | 654 | 124,9 | 3,210 |
| 30 | 0,18 | 350 | 140 | 30 | 1212 | 888,5 | 161,7 | 3,216 |
| 31 | 0,18 | 250 | 80 | 110 | 846,3 | 624 | 111,1 | 3,080 |
| 32 | 0,18 | 300 | 140 | 30 | 1155 | 873,1 | 140,9 | 2,394 |
| 33 | 0,18 | 350 | 80 | 30 | 990,7 | 858,4 | 66,1 | 2,533 |
| 34 | 0,18 | 250 | 140 | 30 | 1123 | 829,1 | 146,9 | 1,864 |
| 35 | 0,18 | 300 | 80 | 70 | 990,7 | 638,3 | 176,2 | 2,496 |
| 36 | 0,18 | 350 | 140 | 70 | 991,1 | 844 | 73,5 | 2,668 |
| 37 | 0,15 | 250 | 80 | 110 | 799,7 | 579,6 | 110,1 | 2,720 |
| 38 | 0,15 | 300 | 140 | 70 | 814,4 | 682,3 | 66,1 | 2,011 |
| 39 | 0,15 | 350 | 80 | 30 | 785 | 638,3 | 73,3 | 2,414 |
| 40 | 0,15 | 250 | 140 | 30 | 931,8 | 682,3 | 124,7 | 2,044 |
| 41 | 0,15 | 300 | 80 | 110 | 843,7 | 653 | 95,3 | 2,027 |
| 42 | 0,15 | 350 | 140 | 30 | 873,1 | 726,3 | 73,4 | 2,119 |
| 43 | 0,15 | 250 | 80 | 30 | 917,1 | 667,6 | 124,7 | 2,165 |
| 44 | 0,15 | 300 | 140 | 110 | 799,7 | 653 | 73,3 | 2,033 |
| 45 | 0,15 | 350 | 80 | 110 | 917,1 | 877,7 | 19,7 | 2,103 |
| 46 | 0,15 | 250 | 140 | 70 | 873,1 | 623,6 | 124,7 | 2,036 |
| 47 | 0,15 | 300 | 80 | 70 | 755,7 | 594,3 | 80,7 | 1,696 |
| 48 | 0,15 | 350 | 140 | 110 | 854,4 | 653 | 100,7 | 2,333 |
| 49 | 0,15 | 250 | 80 | 70 | 931,8 | 799,7 | 66,1 | 1,954 |
| 50 | 0,15 | 300 | 140 | 30 | 829,1 | 682,3 | 73,4 | 1,763 |
| 51 | 0,15 | 350 | 80 | 70 | 741 | 623,6 | 58,7 | 1,746 |
| 52 | 0,15 | 250 | 140 | 110 | 843,7 | 697 | 73,3 | 2,005 |
| 53 | 0,15 | 300 | 80 | 30 | 843,7 | 609 | 117,3 | 1,875 |
| 54 | 0,15 | 350 | 140 | 70 | 887,7 | 594,3 | 146,7 | 2,052 |
| 55 | 0,18 | 250 | 80 | 70 | 873,1 | 638,3 | 117,4 | 2,546 |
| 56 | 0,18 | 300 | 140 | 110 | 873,1 | 697,7 | 87,7 | 2,812 |
| 57 | 0,18 | 350 | 80 | 110 | 843,7 | 639,7 | 102, | 2,924 |
| 58 | 0,18 | 250 | 140 | 70 | 964,4 | 697,3 | 133,5 | 1,997 |
| 59 | 0,18 | 300 | 80 | 30 | 843,7 | 697,0 | 73,3 | 2,144 |
| 60 | 0,18 | 350 | 140 | 110 | 854,4 | 682,3 | 86,0 | 2,696 |

| running order | orifice [mm] | pressure [MPa] | abrasive flow rate [g/min] | feed rate [mm/min] | width on top [µm] | width on bottom [µm] | taper [µm] | roughness [µm] |
|---|---|---|---|---|---|---|---|---|
| 61 | 0,18 | 250 | 80 | 30 | 873,1 | 653,0 | 110,1 | 1,751 |
| 62 | 0,18 | 300 | 140 | 70 | 902,4 | 682,3 | 110,0 | 3,159 |
| 63 | 0,18 | 350 | 80 | 70 | 814,4 | 594,3 | 110,1 | 3,131 |
| 64 | 0,18 | 250 | 140 | 110 | 888,0 | 623,6 | 132,2 | 2,640 |
| 65 | 0,18 | 300 | 80 | 110 | 829,9 | 667,6 | 81,1 | 2,096 |
| 66 | 0,18 | 350 | 140 | 30 | 962,5 | 770,4 | 96,0 | 2,374 |
| 67 | 0,18 | 250 | 80 | 110 | 902,4 | 653,0 | 124,7 | 3,265 |
| 68 | 0,18 | 300 | 140 | 30 | 1020,0 | 770,4 | 124,8 | 1,888 |
| 69 | 0,18 | 350 | 80 | 30 | 726,3 | 623,6 | 51,3 | 2,296 |
| 70 | 0,18 | 250 | 140 | 30 | 991,1 | 770,4 | 110,3 | 2,032 |
| 71 | 0,18 | 300 | 80 | 70 | 858,4 | 741,0 | 58,7 | 2,136 |
| 72 | 0,18 | 350 | 140 | 70 | 1035,0 | 741,0 | 147,0 | 2,193 |
| 73 | 0,15 | 250 | 80 | 70 | 799,7 | 638,3 | 80,7 | 1,834 |
| 74 | 0,15 | 300 | 140 | 110 | 858,4 | 623,6 | 117,4 | 1,923 |
| 75 | 0,15 | 350 | 80 | 110 | 931,8 | 579,6 | 176,1 | 2,123 |
| 76 | 0,15 | 250 | 140 | 70 | 961,1 | 653,0 | 154,1 | 2,382 |
| 77 | 0,15 | 300 | 80 | 30 | 887,7 | 623,6 | 132,1 | 1,806 |
| 78 | 0,15 | 350 | 140 | 110 | 902,4 | 653,0 | 124,7 | 2,033 |
| 79 | 0,15 | 250 | 80 | 30 | 854,8 | 667,6 | 93,6 | 1,991 |
| 80 | 0,15 | 300 | 140 | 70 | 770,4 | 623,6 | 73,4 | 2,074 |
| 81 | 0,15 | 350 | 80 | 70 | 799,7 | 564,9 | 117,4 | 1,795 |
| 82 | 0,15 | 250 | 140 | 110 | 755,7 | 623,6 | 66,0 | 2,220 |
| 83 | 0,15 | 300 | 80 | 110 | 829,1 | 594,3 | 117,4 | 1,993 |
| 84 | 0,15 | 350 | 140 | 30 | 814,4 | 638,3 | 88,0 | 2,246 |
| 85 | 0,15 | 250 | 80 | 110 | 843,7 | 609,0 | 117,3 | 1,866 |
| 86 | 0,15 | 300 | 140 | 30 | 931,8 | 623,6 | 154,1 | 1,697 |
| 87 | 0,15 | 350 | 80 | 30 | 741,0 | 594,3 | 73,3 | 1,910 |
| 88 | 0,15 | 250 | 140 | 30 | 843,7 | 638,3 | 102,7 | 1,531 |
| 89 | 0,15 | 300 | 80 | 70 | 887,7 | 624,0 | 131,8 | 1,614 |
| 90 | 0,15 | 350 | 140 | 70 | 726,3 | 653,3 | 36,5 | 1,892 |
| 91 | 0,15 | 250 | 80 | 110 | 755,7 | 535,6 | 110,0 | 1,866 |
| 92 | 0,15 | 300 | 140 | 70 | 814,4 | 512,5 | 95,4 | 2,082 |
| 93 | 0,15 | 350 | 80 | 30 | 785,5 | 682,3 | 51,3 | 2,064 |
| 94 | 0,15 | 250 | 140 | 30 | 755,7 | 564,9 | 95,4 | 1,681 |
| 95 | 0,15 | 300 | 80 | 110 | 711,7 | 550,3 | 80,7 | 2,005 |
| 96 | 0,15 | 350 | 140 | 30 | 843,7 | 667,6 | 88,0 | 1,966 |
| 97 | 0,15 | 250 | 80 | 30 | 829,1 | 564,9 | 132,1 | 2,072 |
| 98 | 0,15 | 300 | 140 | 110 | 887,7 | 682,3 | 102,7 | 2,351 |

| running order | orifice [mm] | pressure [MPa] | abrasive flow rate [g/min] | feed rate [mm/min] | width on top [µm] | width on bottom [µm] | taper [µm] | roughness [µm] |
|---|---|---|---|---|---|---|---|---|
| 99 | 0,15 | 350 | 80 | 110 | 697,0 | 579,6 | 58,7 | 1,855 |
| 100 | 0,15 | 250 | 140 | 70 | 814,4 | 579,6 | 117,4 | 2,355 |
| 101 | 0,15 | 300 | 80 | 70 | 711,7 | 564,9 | 73,4 | 1,806 |
| 102 | 0,15 | 350 | 140 | 110 | 623,6 | 476,9 | 73,3 | 2,228 |
| 103 | 0,15 | 250 | 80 | 70 | 785,0 | 564,9 | 110,1 | 1,978 |
| 104 | 0,15 | 300 | 140 | 30 | 829,1 | 623,6 | 102,7 | 1,742 |
| 105 | 0,15 | 350 | 80 | 70 | 711,7 | 594,3 | 58,7 | 1,785 |
| 106 | 0,15 | 250 | 140 | 110 | 829,1 | 579,6 | 124,7 | 1,877 |
| 107 | 0,15 | 300 | 80 | 30 | 785,0 | 638,6 | 73,2 | 1,925 |
| 108 | 0,15 | 350 | 140 | 70 | 799,7 | 667,6 | 66,0 | 2,032 |
| 109 | 0,15 | 250 | 80 | 110 | 858,4 | 653,0 | 102,7 | 2,545 |
| 110 | 0,15 | 300 | 140 | 70 | 917,1 | 726,3 | 95,4 | 1,860 |
| 111 | 0,15 | 350 | 80 | 30 | 917,1 | 711,7 | 102,7 | 2,161 |
| 112 | 0,15 | 250 | 140 | 30 | 1049,0 | 755,7 | 146,6 | 2,114 |
| 113 | 0,15 | 300 | 80 | 110 | 799,7 | 623,6 | 88,0 | 2,528 |
| 114 | 0,15 | 350 | 140 | 30 | 990,5 | 799,7 | 95,4 | 1,993 |
| 115 | 0,15 | 250 | 80 | 30 | 931,8 | 638,3 | 146,7 | 2,022 |
| 116 | 0,15 | 300 | 140 | 110 | 887,7 | 681,3 | 103,2 | 2,682 |
| 117 | 0,15 | 350 | 80 | 110 | 741,0 | 653,0 | 44,0 | 1,952 |
| 118 | 0,15 | 250 | 140 | 70 | 917,4 | 653,0 | 132,2 | 2,156 |
| 119 | 0,15 | 300 | 80 | 70 | 799,7 | 653,0 | 73,3 | 2,885 |
| 120 | 0,15 | 350 | 140 | 110 | 843,7 | 638,3 | 102,7 | 3,342 |
| 121 | 0,15 | 250 | 80 | 70 | 858,4 | 711,7 | 73,3 | 2,452 |
| 122 | 0,15 | 300 | 140 | 30 | 990,5 | 682,3 | 154,1 | 1,880 |
| 123 | 0,15 | 350 | 80 | 70 | 770,4 | 579,6 | 95,4 | 2,630 |
| 124 | 0,15 | 250 | 140 | 110 | 858,4 | 667,6 | 95,4 | 3,001 |
| 125 | 0,15 | 300 | 80 | 30 | 829,1 | 682,3 | 73,4 | 1,993 |
| 126 | 0,15 | 350 | 140 | 70 | 873,1 | 682,3 | 95,4 | 2,437 |
| 127 | 0,18 | 250 | 80 | 70 | 902,4 | 697,0 | 102,7 | 2,489 |
| 128 | 0,18 | 300 | 140 | 110 | 873,1 | 726,3 | 73,4 | 2,609 |
| 129 | 0,18 | 350 | 80 | 110 | 873,1 | 682,3 | 95,4 | 2,593 |
| 130 | 0,18 | 350 | 80 | 70 | 858,4 | 697,0 | 80,7 | 2,214 |
| 131 | 0,18 | 300 | 80 | 30 | 902,4 | 741,0 | 80,7 | 2,784 |
| 132 | 0,18 | 350 | 80 | 110 | 1005,0 | 770,4 | 117,3 | 2,210 |
| 133 | 0,18 | 250 | 140 | 30 | 741,0 | 623,6 | 58,7 | 2,046 |
| 134 | 0,18 | 300 | 80 | 70 | 902,4 | 770,4 | 66,0 | 2,147 |
| 135 | 0,18 | 250 | 140 | 70 | 990,5 | 697,0 | 146,7 | 2,364 |
| 136 | 0,18 | 250 | 140 | 110 | 931,9 | 682,3 | 124,8 | 2,598 |

| running order | orifice [mm] | pressure [MPa] | abrasive flow rate [g/min] | feed rate [mm/min] | width on top [µm] | width on bottom [µm] | taper [µm] | roughness [µm] |
|---|---|---|---|---|---|---|---|---|
| 137 | 0,18 | 300 | 140 | 110 | 841,4 | 638,3 | 101,5 | 2,512 |
| 138 | 0,18 | 350 | 80 | 30 | 1020,0 | 799,7 | 110,1 | 2,436 |
| 139 | 0,18 | 250 | 140 | 110 | 741,0 | 697,0 | 22,0 | 2,335 |
| 140 | 0,18 | 300 | 80 | 30 | 1071,0 | 770,4 | 150,3 | 2,163 |
| 141 | 0,18 | 350 | 140 | 30 | 931,8 | 741,0 | 95,4 | 2,594 |
| 142 | 0,18 | 250 | 80 | 30 | 1020,0 | 799,7 | 110,1 | 1,738 |
| 143 | 0,18 | 300 | 140 | 70 | 946,4 | 653,0 | 146,7 | 2,253 |
| 144 | 0,18 | 350 | 80 | 70 | 976 | 726,3 | 124,8 | 2,041 |

## A.2. Analysis of the kerf top width

The ANOVA model used to analyse the top kerf width is the complete model: all the factors and their interactions are considered ;only the interaction between the orifice and the other factors are disregarded, because this is a hypothesis of the blocking approach applied on the factor “orifice”.
Before analyzing the experiments data, it’s useful to see the main effects plot (**Figure A.1**) and the interaction plot (**Figure A.2**). Observing the main effects plot, it seems that orifice, abrasive flow rate and feed rate influence the top kerf width, while all the interactions seem to be not significant.

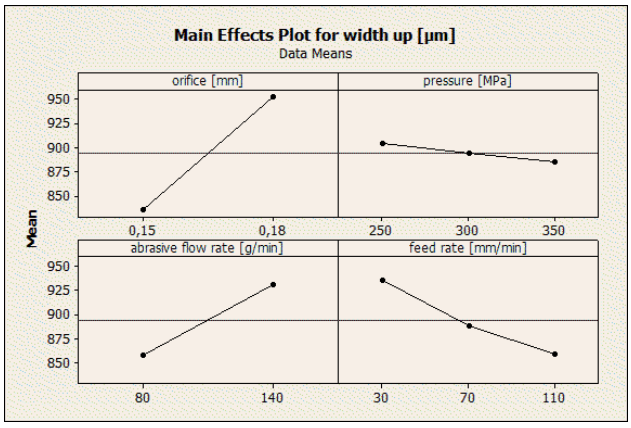


**Figure A.1.:** Main effects plots for top kerf width.

The ANOVA output of the programme is presented below:

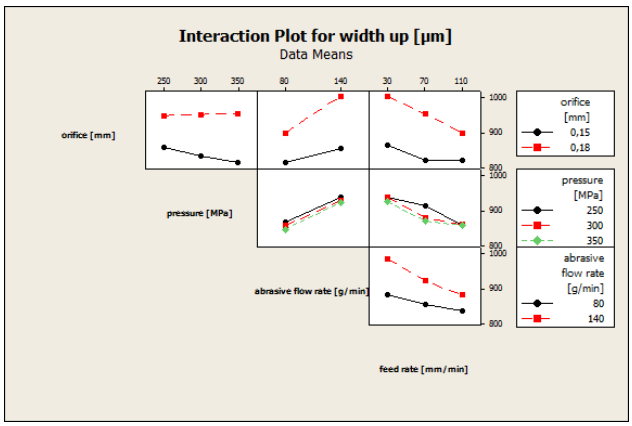


**Figure A.2.:** Interaction plot for top kerf width.

**General Linear Model: width up [µm versus orifice [mm]; pressure [MP; ...**

| Factor | Type | Levels | Values |
|---|---|---|---|
| orifice [mm] | fixed | 2 | 0,15; 0,18 |
| pressure [MPa] | fixed | 3 | 250; 300; 350 |
| abrasive flow rate [g/min] | fixed | 2 | 80; 140 |
| feed rate [mm/min] | fixed | 3 | 30; 70; 110 |

Analysis of Variance for width up [µm], using Adjusted SS for Tests

| Source | DF | Seq SS | Adj SS | Adj MS | F | P |
|---|---|---|---|---|---|---|
| **orifice [mm]** | 1 | 489557 | 489557 | 489557 | 79,14 | 0,000 |
| pressure [MPa] | 2 | 8502 | 8502 | 4251 | 0,69 | 0,505 |
| **abrasive flow rate** [g/min] | 1 | 191742 | 191742 | 191742 | 30,99 | 0,000 |
| **feed rate [mm/min]** | 2 | 141316 | 141316 | 70658 | 11,42 | 0,000 |
| pressure [MPa]* abrasive flow rate [g/min] | 2 | 354 | 354 | 177 | 0,03 | 0,972 |
| pressure [MPa]*feed rate [mm/min] | 4 | 11291 | 11291 | 2823 | 0,46 | 0,768 |
| abrasive flow rate [g/min]* feed rate [mm/min] | 2 | 21041 | 21041 | 10521 | 1,70 | 0,187 |
| pressure [MPa]* abrasive flow rate [g/min]* feed rate [mm/min] | 4 | 7258 | 7258 | 1815 | 0,29 | 0,882 |
| Error | 125 | 773279 | 773279 | 6186 | | |
| Total | 143 | 1644341 | | | | |

S = 78,6526 R-Sq = 52,97% R-Sq(adj) = 46,20%

The ANOVA shows that orifice, abrasive flow rate and feed rate influence the top kerf width (p-value smaller than $\alpha_{BONF} = 0{,}05 \ / \ 4 = 0{,}0125$).
After that it's necessary to verify the statistical hypothesis of ANOVA: the test of normality of the residuals (**Figure A.3**), the test for equal variances (**Figure A.4**) and the independence of the residuals (**Figure A.5**).

After these verifications, it's possible to confirm that orifice, abrasive and feed rate influence the top kerf width.
In addition it is important to establish which level of each factor is the best, in

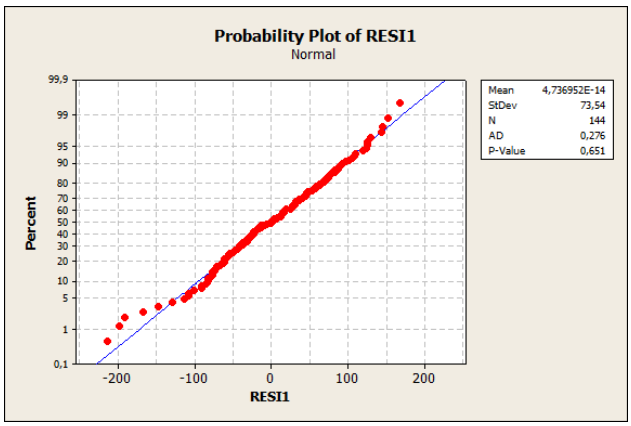


**Figure A.3.:** The probability plot shows the normality of the residuals (p-value bigger than 0,05)

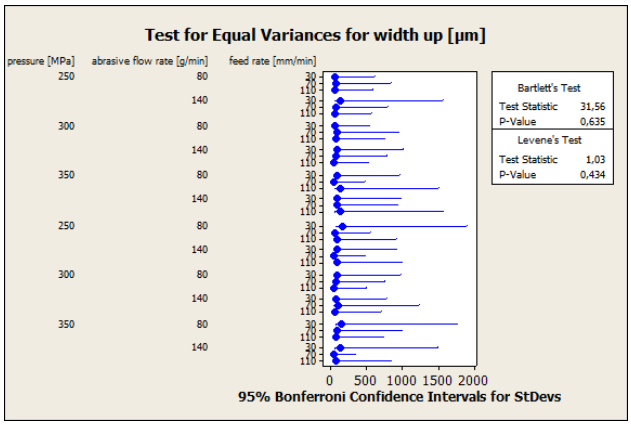


**Figure A.4.:** The test for equal variances shows that the variances are homogenous (p-value bigger than 0,05)

this case to minimize the top kerf width. The employed statistical method is the "multiple comparisons", using the Tuckey's test.

### Factor: orifice

$T_\alpha = \frac{q_\alpha(a, df_E)}{\sqrt{2}} = \frac{q_{0,016}(2,125)}{\sqrt{2}} = \frac{3,64}{\sqrt{2}} = 2,57$

The critic value is: $T_\alpha\sqrt{\hat{V}(\hat{D}_{ij})} = T_\alpha\sqrt{MS_E\frac{2}{b\cdot c\cdot n}} = 2,57\sqrt{6186\cdot\frac{2}{2\cdot 3\cdot 4}} = 58,34$

Mean of each level of orifice:
- 0,15 = 835,88 µm
- 0,18 = 952,5 µm

| differences | 0,18 |
|---|---|
| **0,15** | 116,62 |

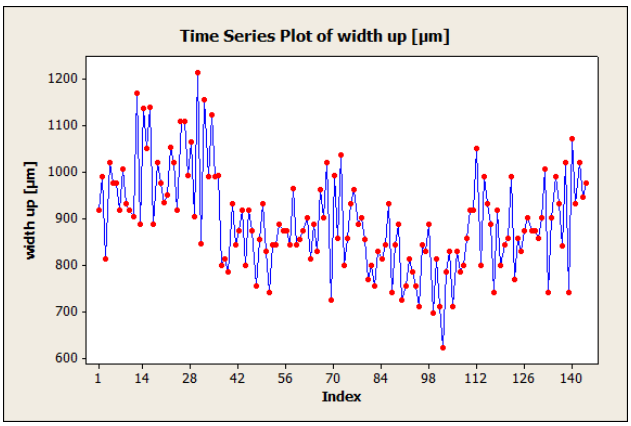


**Figure A.5.:** The time series plot shows that there aren't any trends, but the residuals are independent: it's useful to see a systematic error.

The best level of orifice to minimize the top kerf width is 0,15 mm.

### Factor: abrasive flow rate

$T_\alpha = \frac{q_\alpha(a,df_E)}{\sqrt{2}} = \frac{q_{0,016}(2,125)}{\sqrt{2}} = \frac{3,64}{\sqrt{2}} = 2,57$

The critic value is: $T_\alpha\sqrt{\hat{V}(\hat{D}_{ij})} = T_\alpha\sqrt{MS_E\frac{2}{a\cdot c\cdot n}} = 2,57\sqrt{6186\cdot\frac{2}{2\cdot 3\cdot 4}} = 58,34$

Mean of each level of abrasive flow rate:
- 80 = 857,7 µm
- 140 = 930,7 µm

| differences | 140 |
|---|---|
| 80 | 73 |

The best level of abrasive flow rate to minimize the top kerf width is 80 g/min.

### Factor: feed rate

$T_\alpha = \frac{q_\alpha(a,df_E)}{\sqrt{2}} = \frac{q_{0,016}(3,125)}{\sqrt{2}} = \frac{4,14}{\sqrt{2}} = 2,93$

The critic value is: $T_\alpha\sqrt{\hat{V}(\hat{D}_{ij})} = T_\alpha\sqrt{MS_E\frac{2}{a\cdot b\cdot n}} = 2,93\sqrt{6186\cdot\frac{2}{2\cdot 2\cdot 4}} = 81,47$

Mean of each level of feed rate:
- 30 = 935,2 µm
- 70 = 888,3 µm
- 110 = 859,1 µm

| differences | 70 | 110 |
|---|---|---|
| **30** | 46,9 | 76,81 |
| **70** | | 29,2 |

There's no meaningful difference among each levels: It's possible to choose arbitrary the level of feed rate, but it's better to set on the level of 110 mm/min in order to increase productivity.

## A.3. Analysis of the kerf bottom width

The ANOVA model used to analyse the bottom kerf width is the complete model: all the factors and their interactions are considered; only the interaction between the orifice and the other factors are disregarded, because this is a hypothesis of the blocking approach which was used on the factor "orifice").
Before analysing the experiments data, it's useful to see the main effects plots (**Figure A.6**) and the interaction plot (**Figure A.7**). Observing the main effects plot, it seems that orifice, abrasive flow rate and feed rate influence the bottom kerf width, while all the interactions seem to be not significant.

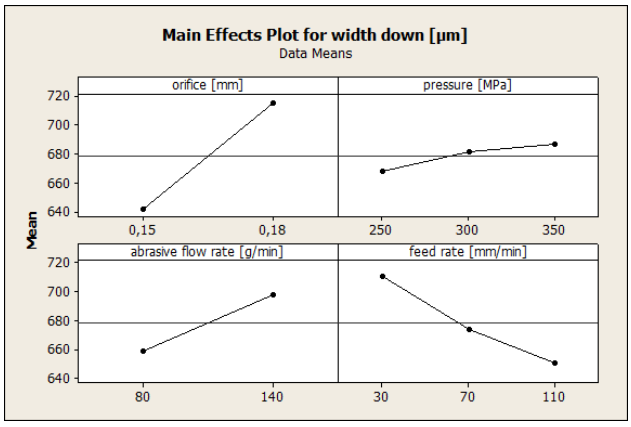


**Figure A.6.:** Main effects plots of the bottom kerf width.

The ANOVA output of the programme is presented below:

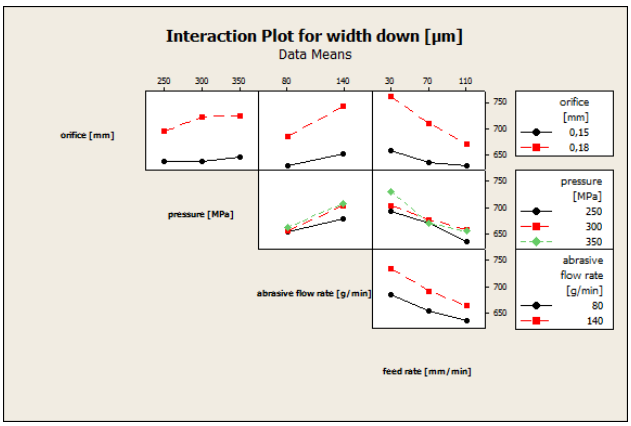


**Figure A.7.:** Interaction plot for bottom kerf width.

**General Linear Model: width down [ versus orifice [mm]; pressure [MP; ...**

| Factor | Type | Levels | Values |
|---|---|---|---|
| orifice [mm] | fixed | 2 | 0,15; 0,18 |
| pressure [MPa] | fixed | 3 | 250; 300; 350 |
| abrasive flow rate [g/min] | fixed | 2 | 80; 140 |
| feed rate [mm/min] | fixed | 3 | 30; 70; 110 |

Analysis of Variance for width down [µm], using Adjusted SS for Tests

| Source | DF | Seq SS | Adj SS | Adj MS | F | P |
|---|---|---|---|---|---|---|
| orifice [mm] | 1 | 196197 | 196197 | 196197 | 60,20 | 0,000 |
| pressure [MPa] | 2 | 8985 | 8985 | 4492 | 1,38 | 0,256 |
| abrasive flow rate [g/min] | 1 | 55606 | 55606 | 55606 | 17,06 | 0,000 |
| feed rate [mm/min] | 2 | 87952 | 87952 | 43976 | 13,49 | 0,000 |
| pressure [MPa]* abrasive flow rate [g/min] | 2 | 4592 | 4592 | 2296 | 0,70 | 0,496 |
| pressure [MPa]*feed rate [mm/min] | 4 | 8087 | 8087 | 2022 | 0,62 | 0,649 |
| abrasive flow rate [g/min]* feed rate [mm/min] | 2 | 2874 | 2874 | 1437 | 0,44 | 0,644 |
| pressure [MPa]* abrasive flow rate [g/min]* feed rate [mm/min] | 4 | 21966 | 21966 | 5492 | 1,69 | 0,158 |
| Error | 125 | 407381 | 407381 | 3259 | | |
| Total | 143 | 793641 | | | | |

S = 57,0881 R-Sq = 48,67% R-Sq(adj) = 41,28%

The ANOVA shows that orifice, abrasive flow rate and feed rate influence the bottom kerf width (p-value smaller than $\alpha_{BONF} = 0{,}05 \ / \ 4 = 0{,}0125$).
After that it's necessary to verify the statistical hypothesis of ANOVA: the test of normality of the residuals (**Figure A.8**), the test for equal variances (**Figure A.9**) and the independence of the residuals (**Figure A.10**).

After these verifications, it's possible to confirm that orifice, abrasive flow rate and feed rate influence the bottom kerf width.
In addition it is important to determine which is the best level for each factor, in this case to minimize the bottom kerf width. The employed statistical method is

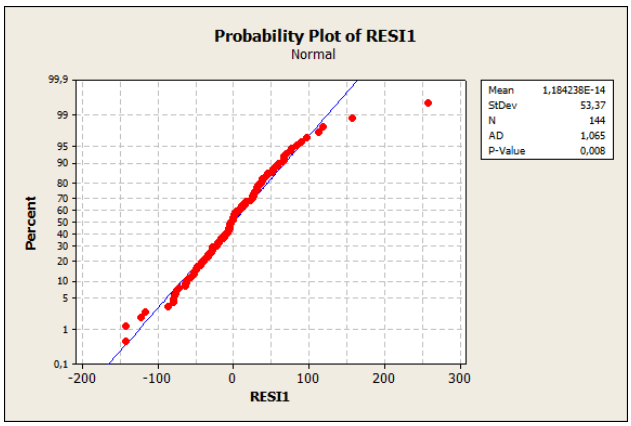


**Figure A.8.:** The probability plot shows the normality of the residuals (p-value bigger than 0,05)

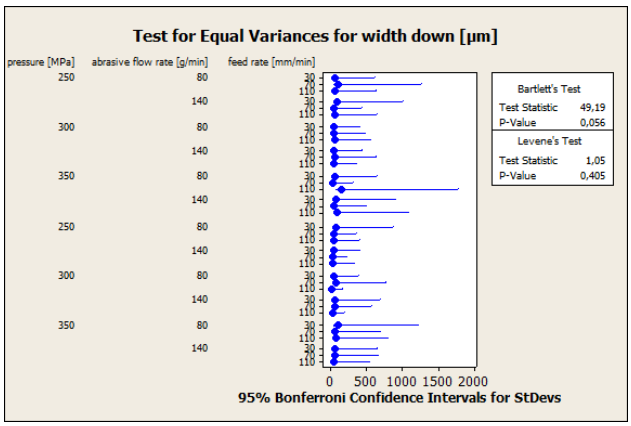


**Figure A.9.:** The test for equal variances shows that the variances are homogenous (p-value bigger than 0,05)

the multiple comparisons, using the Tuckey's test.

### Factor: orifice

$T_\alpha = \frac{q_\alpha(a,df_E)}{\sqrt{2}} = \frac{q_{0,016}(2,125)}{\sqrt{2}} = \frac{3,64}{\sqrt{2}} = 2,57$

The critic value is: $T_\alpha\sqrt{\hat{V}(\hat{D}_{ij})} = T_\alpha\sqrt{MS_E\frac{2}{b\cdot c\cdot n}} = 2,57\sqrt{3259\cdot\frac{2}{2\cdot 3\cdot 4}} = 42,35$

Mean of each level of orifice:
- 0,15 = 641,62 µm
- 0,18 = 715,44 µm

| differences | 0,18 |
|---|---|
| 0,15 | 73,82 |

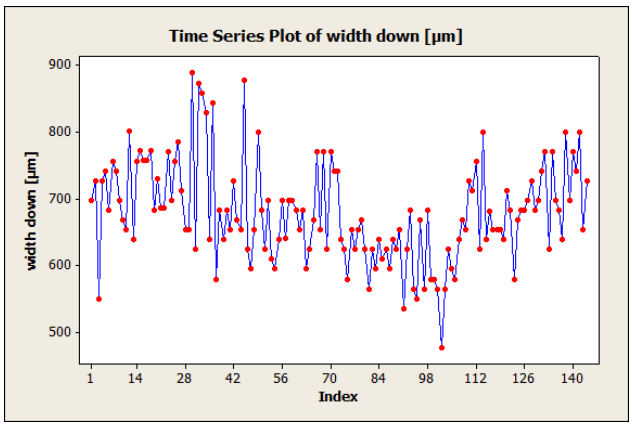


**Figure A.10.:** The time series plot shows that there aren't any trends, but the residuals are independent: it's useful to see a systematic error.

The best level of orifice to minimize the bottom kerf width is 0,15 mm.

### Factor: abrasive flow rate

$T_\alpha = \frac{q_\alpha(a, df_E)}{\sqrt{2}} = \frac{q_{0,016}(2,125)}{\sqrt{2}} = \frac{3,64}{\sqrt{2}} = 2,57$

The critic value is: $T_\alpha\sqrt{\hat{V}(\hat{D_{ij}})} = T_\alpha\sqrt{MS_E\frac{2}{a \cdot c \cdot n}} = 2,57\sqrt{3259 \cdot \frac{2}{2 \cdot 3 \cdot 4}} = 42,35$

Mean of each level of abrasive flow rate:
- 80 = 658,8 µm
- 140 = 698,18 µm

| differences | 140 |
|---|---|
| **80** | 39,3 |

There's no meaningful difference between these two levels, but the value is very close to the critic value, so it's possible to infer that the best level of abrasive flow rate to minimize the bottom kerf width is 80 g/min.

### Factor: feed rate

$T_\alpha = \frac{q_\alpha(a, df_E)}{\sqrt{2}} = \frac{q_{0,016}(3,125)}{\sqrt{2}} = \frac{4,14}{\sqrt{2}} = 2,93$

The critic value is: $T_\alpha\sqrt{\hat{V}(\hat{D_{ij}})} = T_\alpha\sqrt{MS_E\frac{2}{a \cdot b \cdot n}} = 2,93\sqrt{3259 \cdot \frac{2}{2 \cdot 2 \cdot 4}} = 59,13$

Mean of each level of feed rate:
- 30 = 710,8 µm
- 70 = 673,91 µm
- 110 = 650,84 µm

| differences | 70 | 110 |
|---|---|---|
| **30** | 36,89 | 59,96 |
| **70** | | 23,07 |

The best level of feed rate to minimize the bottom kerf width is 110 mm/min.

## A.4. Analysis kerf taper

The ANOVA model of used to analyse the kerf taper is the complete model: all the factors and their interactions are considered; only the interaction between the orifice and the other factors are disregarded, because this is a hypothesis of the blocking approach, which was used on the factor "orifice".
Before analysing the experiments data, it's useful to see the main effects plots (**Figure A.11**) and the interaction plot (**Figure A.12**). Observing the main effects plot, it seems that orifice, abrasive flow rate and pressure influence the kerf taper, while the interactions that seem to be meaningful are those between pressure-feed rate and abrasive flow rate – feed rate.

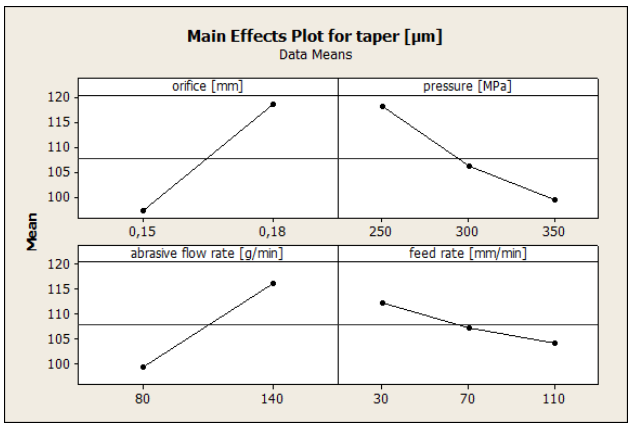


**Figure A.11.:** Main effects plots of the kerf taper.

The ANOVA output of the programme is presented below:

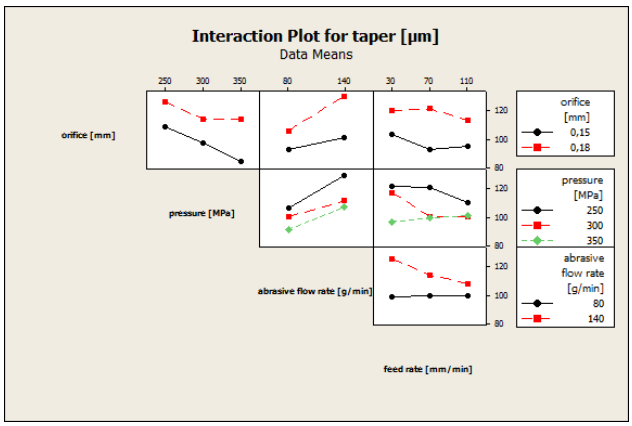


**Figure A.12.:** Interaction plot for the kerf taper.

**General Linear Model: taper [µm] versus orifice [mm]; pressure [MP; ...**

| Factor | Type | Levels | Values |
|---|---|---|---|
| orifice [mm] | fixed | 2 | 0,15; 0,18 |
| pressure [MPa] | fixed | 3 | 250; 300; 350 |
| abrasive flow rate [g/min] | fixed | 2 | 80; 140 |
| feed rate [mm/min] | fixed | 3 | 30; 70; 110 |

Analysis of Variance for taper [µm], using Adjusted SS for Tests

| Source | DF | Seq SS | Adj SS | Adj MS | F | P |
|---|---|---|---|---|---|---|
| orifice [mm] | 1 | 16479 | 16479 | 16479 | 16,17 | 0,000 |
| pressure [MPa] | 2 | 8665 | 8665 | 4333 | 4,25 | 0,016 |
| abrasive flow rate [g/min] | 1 | 10209 | 10209 | 10209 | 10,02 | 0,002 |
| feed rate [mm/min] | 2 | 1574 | 1574 | 787 | 0,77 | 0,464 |
| pressure [MPa]* abrasive flow rate [g/min] | 2 | 897 | 897 | 449 | 0,44 | 0,645 |
| pressure [MPa]*feed rate [mm/min] | 4 | 3117 | 3117 | 779 | 0,76 | 0,550 |
| abrasive flow rate [g/min]* feed rate [mm/min] | 2 | 2094 | 2094 | 1047 | 1,03 | 0,361 |
| pressure [MPa]* abrasive flow rate [g/min]* feed rate [mm/min] | 4 | 5380 | 5380 | 1345 | 1,32 | 0,266 |
| Error | 125 | 127396 | 127396 | 1019 | | |
| Total | 143 | 175812 | | | | |

S = 31,9244 R-Sq = 27,54% R-Sq(adj) = 17,10%

The ANOVA shows that orifice and feed rate influence the kerf taper (p-value smaller than $\alpha_{BONF} = 0{,}05 \ / \ 4 = 0{,}0125$), while the p-value of pressure is very close to the $\alpha_{BONF}$ , so the experimenter considers its influence at this step.
After that it's necessary to verify the statistical hypothesis of ANOVA: the test of normality of the residuals (**Figure A.13**), the test for equal variances (**Figure A.14**) and the independence of the residuals (**Figure A.15**).

After these verifications, it is possible to infer that orifice, pressure and abrasive flow rate influence the kerf taper.
In addition to find the influencing parameters, it's important to establish which level of each factor is the best, in this case to minimize the kerf taper. The employed

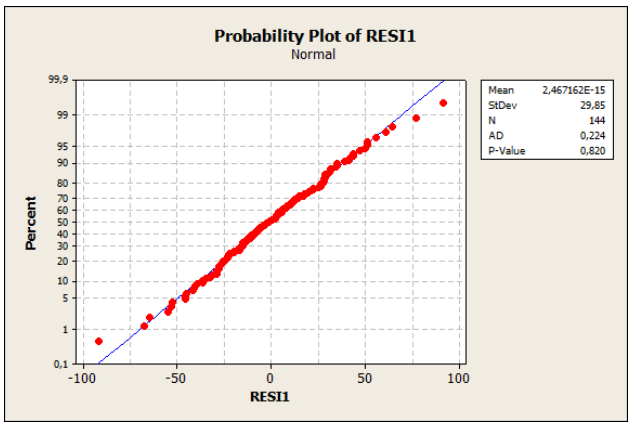


**Figure A.13.:** The probability plot shows the normality of the residuals (p-value bigger than 0,05)

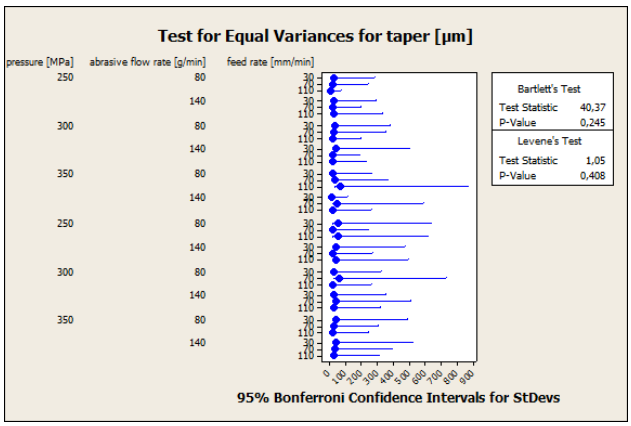


**Figure A.14.:** The test for equal variances shows that the variances are homogenous (p-value bigger than 0,05)

statistical method is the multiple comparisons, using the Tuckey's test.

### Factor: orifice

$T_\alpha = \frac{q_\alpha(a,df_E)}{\sqrt{2}} = \frac{q_{0,016}(2,125)}{\sqrt{2}} = \frac{3,64}{\sqrt{2}} = 2,57$

The critic value is: $T_\alpha\sqrt{\hat{V}(\hat{D}_{ij})} = T_\alpha\sqrt{MS_E\frac{2}{b\cdot c\cdot n}} = 2,57\sqrt{1019\cdot\frac{2}{2\cdot 3\cdot 4}} = 23,68$

Mean of each level of orifice:
- 0,15 = 97,13 µm
- 0,18 = 118,53 µm

| **differences** | **0,18** |
|---|---|
| **0,15** | 21,4 |

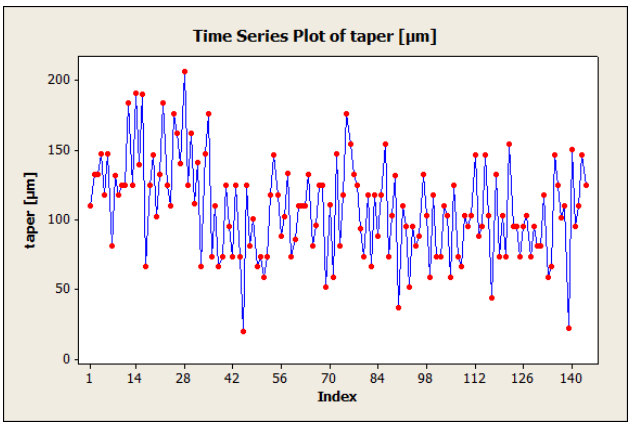


**Figure A.15.:** The time series plot shows that there aren't any trends, but the residuals are independent: it's useful to see a systematic error.

There's no meaningful difference between these two levels.

### Factor: abrasive flow rate

$T_\alpha = \frac{q_\alpha(a, df_E)}{\sqrt{2}} = \frac{q_{0,016}(2,125)}{\sqrt{2}} = \frac{3{,}64}{\sqrt{2}} = 2,57$

The critic value is: $T_\alpha\sqrt{\hat{V}(\hat{D_{ij}})} = T_\alpha\sqrt{MS_E\frac{2}{a\cdot c\cdot n}} = 2,57\sqrt{1019\cdot\frac{2}{2\cdot 3\cdot 4}} = 23,69$

Mean of each level of abrasive flow rate:
- 80 = 99,41 µm
- 140 = 116,25 µm

| **differences** | **140** |
|---|---|
| **80** | 16,84 |

There's no meaningful difference between these two levels, but for economic reasons it is better to set the abrasive flow rate on the level of 80 g/min.

### Factor: pressure

$T_\alpha = \frac{q_\alpha(a, df_E)}{\sqrt{2}} = \frac{q_{0,016}(3,125)}{\sqrt{2}} = \frac{4{,}14}{\sqrt{2}} = 2,93$

The critic value is: $T_\alpha\sqrt{\hat{V}(\hat{D_{ij}})} = T_\alpha\sqrt{MS_E\frac{2}{a\cdot b\cdot n}} = 2,93\sqrt{1019\cdot\frac{2}{2\cdot 2\cdot 4}} = 33,06$

Mean of each level of pressure:
- 30 = 118,04 µm
- 70 = 106,19 µm
- 110 = 99,26 µm

| differences | 300 | 350 |
|---|---|---|
| **250** | 11,85 | 18,78 |
| **300** | | 6,93 |

There's no meaningful difference among each levels.

## A.5. Analysis of kerf roughness

The ANOVA model used to analyse the roughness is the complete model: all the factors and their interactions are considered; only the interaction between the orifice and the other factors are disregarded, because this is a hypothesis of the blocking approach, which was used on the "orifice" factor.
Before analysing the experiments data, it's useful to see the main effects plots (**Figure A.16**) and the interaction plot (**Figure A.17**). Observing the main effects plot, it seems that orifice, feed rate and pressure influence the kerf roughness, while the interaction that seems to be meaningful is those between abrasive flow rate – feed rate.

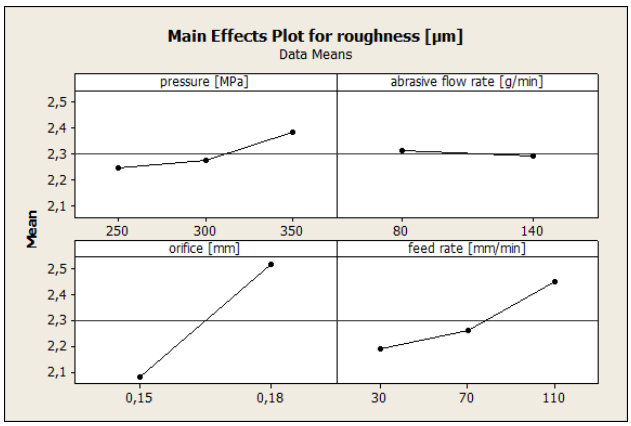


**Figure A.16.:** Main effects plots of the roughness.

The ANOVA output of the programme is presented below:

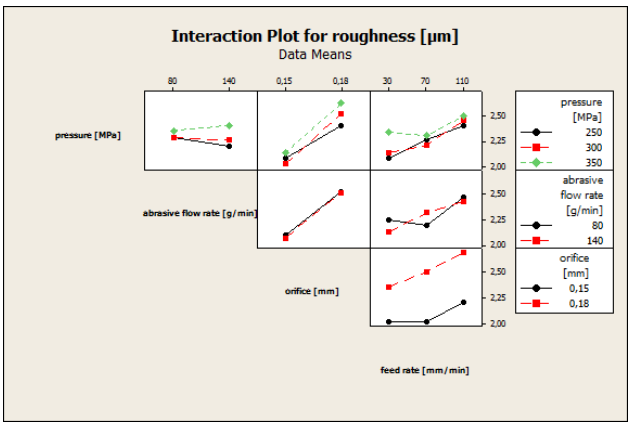


**Figure A.17.:** Interaction plot for the roughness.

**General Linear Model: roughness [µ versus pressure [MP; abrasive flo; ...**

| Factor | Type | Levels | Values |
|---|---|---|---|
| pressure [MPa] | fixed | 3 | 250; 300; 350 |
| abrasive flow rate [g/min] | fixed | 2 | 80; 140 |
| feed rate [mm/min] | fixed | 3 | 30; 70; 110 |
| orifice [mm] | fixed | 2 | 0,15; 0,18 |

**Analysis of Variance for roughness [µm], using Adjusted SS for Tests**

| Source | DF | Seq SS | Adj SS | Adj MS | F | P |
|---|---|---|---|---|---|---|
| pressure [MPa] | 2 | 0,5035 | 0,5295 | 0,2647 | 1,95 | 0,147 |
| abrasive flow rate [g/min] | 1 | 0,0138 | 0,0153 | 0,0153 | 0,11 | 0,738 |
| feed rate [mm/min] | 2 | 1,7762 | 1,8137 | 0,9068 | 6,66 | 0,002 |
| pressure [MPa]* abrasive flow rate [g/min] | 2 | 0,0980 | 0,1128 | 0,0564 | 0,41 | 0,662 |
| pressure [MPa]*feed rate [mm/min] | 4 | 0,2881 | 0,3720 | 0,0930 | 0,68 | 0,605 |
| abrasive flow rate [g/min]* feed rate [mm/min] | 2 | 0,3695 | 0,5901 | 0,2950 | 2,17 | 0,119 |
| pressure [MPa]* abrasive flow rate [g/min]* feed rate [mm/min] | 4 | 0,5710 | 0,5164 | 0,1291 | 0,95 | 0,438 |
| orifice [mm] | 1 | 7,0916 | 7,0916 | 7,0916 | 52,10 | 0,000 |
| Error | 125 | 17,0135 | 17,0135 | 0,1361 | | |
| Total | 143 | 27,7252 | | | | |

S = 0,368928 R-Sq = 38,64% R-Sq(adj) = 29,80%

The ANOVA shows that orifice and feed rate influence the taper of the cut (p-value smaller than $\alpha_{BONF} = 0{,}05 \ / \ 4 = 0{,}0125$).
After that it's necessary to verify the statistical hypothesis of ANOVA: the test of normality of the residuals (**Figure A.18**), the test for equal variances (**Figure A.19**) and the independence of the residuals (**Figure A.20**).

The residuals are not normal, so it's necessary to apply Box-Cox transformation (**Figure A.21**) and then and then a new ANOVA, with the transformed data.

The ANOVA output of the programme is presented below:

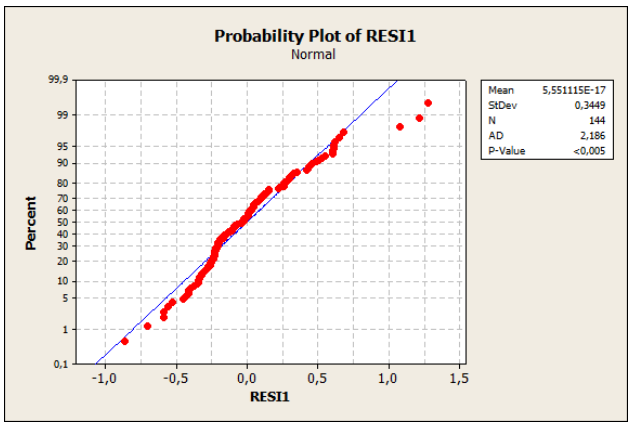


**Figure A.18.:** The probability plot shows the non-normality of the residuals (p-value smaller than 0,05)

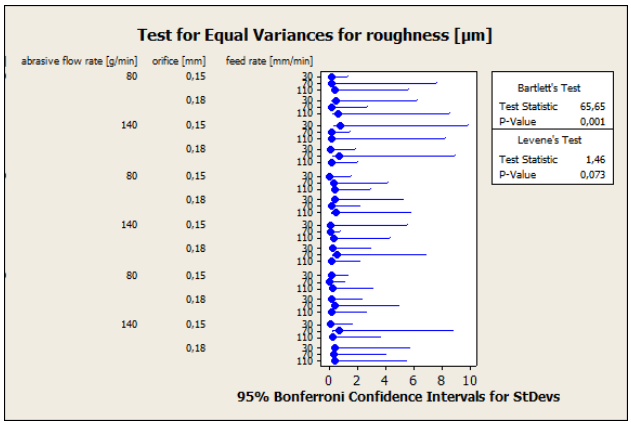


**Figure A.19.:** The test for equal variances shows that the variances are homogenous (p-value bigger than 0,05)

**General Linear Model: transformed versus pressure [MP; abrasive flo; ...**

| Factor | Type | Levels | Values |
|---|---|---|---|
| pressure [MPa] | fixed | 3 | 250; 300; 350 |
| abrasive flow rate [g/min] | fixed | 2 | 80; 140 |
| feed rate [mm/min] | fixed | 3 | 30; 70; 110 |
| orifice [mm] | fixed | 2 | 0,15; 0,18 |

Analysis of Variance for transformed data, using Adjusted SS for Tests

| Source | DF | Seq SS | Adj SS | Adj MS | F | P |
|---|---|---|---|---|---|---|
| pressure [MPa] | 2 | 0,10843 | 0,11094 | 0,05547 | 2,32 | 0,102 |
| abrasive flow rate [g/min] | 1 | 0,00701 | 0,00702 | 0,00702 | 0,29 | 0,589 |
| feed rate [mm/min] | 2 | 0,34658 | 0,35724 | 0,17862 | 7,47 | 0,001 |
| pressure [MPa]* abrasive flow rate [g/min] | 2 | 0,02342 | 0,02615 | 0,01308 | 0,55 | 0,580 |
| pressure [MPa]*feed rate [mm/min] | 4 | 0,07718 | 0,09421 | 0,02355 | 0,99 | 0,418 |
| abrasive flow rate [g/min]* feed rate [mm/min] | 2 | 0,08313 | 0,12543 | 0,06272 | 2,62 | 0,076 |
| pressure [MPa]* abrasive flow rate [g/min]* feed rate [mm/min] | 4 | 0,10638 | 0,09603 | 0,02401 | 1,00 | 0,408 |
| orifice [mm] | 1 | 1,33150 | 1,33150 | 1,33150 | 55,71 | 0,000 |
| Error | 125 | 2,98752 | 2,98752 | 0,02390 | | |
| Total | 143 | 5,07117 | | | | |

S = 0,154597 R-Sq = 41,09% R-Sq(adj) = 32,60%

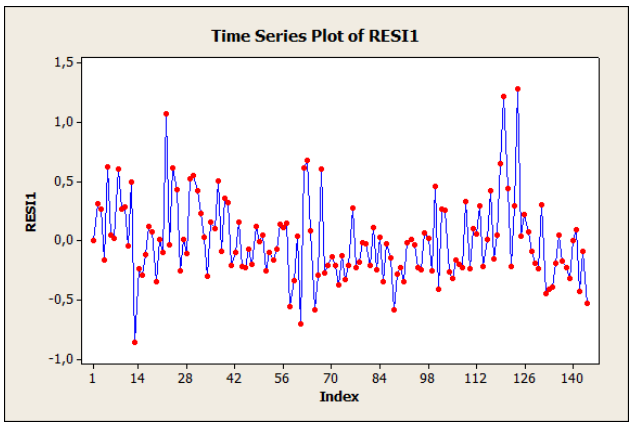


**Figure A.20.:** The time series plot shows that there aren't any trends, but the residuals are independent: it's useful to see a systematic error.

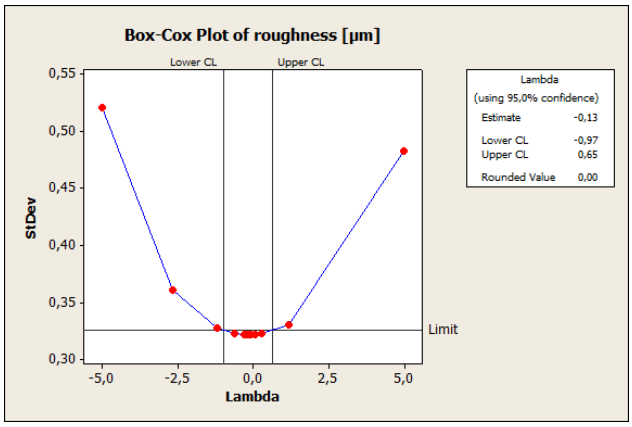


**Figure A.21.:** The Box-Cox plot shows the estimate lambda, that is necessary to transform the original data into data with normal distribution

After that it's necessary to verify the statistical hypothesis of ANOVA: the test of normality of the residuals (**Figure A.22**), the test for equal variances (**Figure A.23**) and the independence of the residuals (**Figure A.24**).

The residuals don't have a normal distribution after the Box-Cox transformation: a possible way it's to simplify the model, considering only the significant factors, namely orifice and feed rate.

The ANOVA output of the programme is presented below:

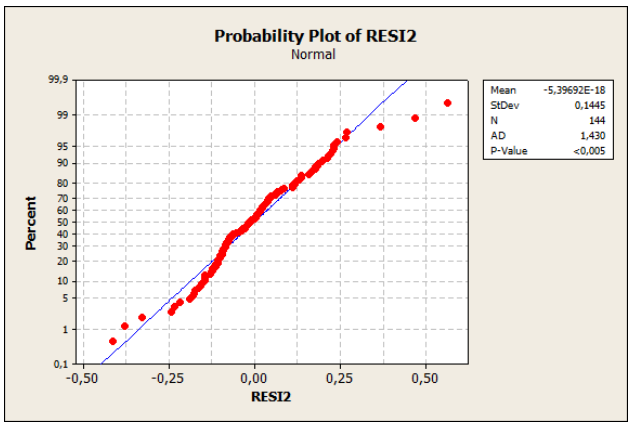


**Figure A.22.:** The probability plot shows the non-normality of the residuals (p-value smaller than 0,05)

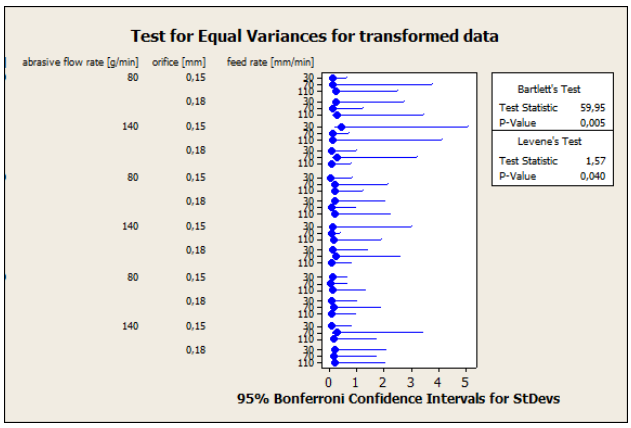


**Figure A.23.:** The test for equal variances shows that the variances are not homogenous (p-value smaller than 0,05)

**General Linear Model: transformed versus feed rate [m; orifice [mm]**

| Factor | Type | Levels | Values |
|---|---|---|---|
| feed rate [mm/min] | fixed | 3 | 30; 70; 110 |
| orifice [mm] | fixed | 2 | 0,15; 0,18 |

Analysis of Variance for transformed data, using Adjusted SS for Tests

| Source | DF | Seq SS | Adj SS | Adj MS | F | P |
|---|---|---|---|---|---|---|
| feed rate [mm/min] | 2 | 0,34778 | 0,34778 | 0,17389 | 7,08 | 0,001 |
| orifice [mm] | 1 | 1,28498 | 1,28498 | 1,28498 | 52,32 | 0,000 |
| Error | 140 | 3,43842 | 3,43842 | 0,02456 | | |
| Total | 143 | 5,07117 | | | | |

S = 0,156717 R-Sq = 32,20% R-Sq(adj) = 30,74%

After that it's necessary to verify the statistical hypothesis of ANOVA: the test

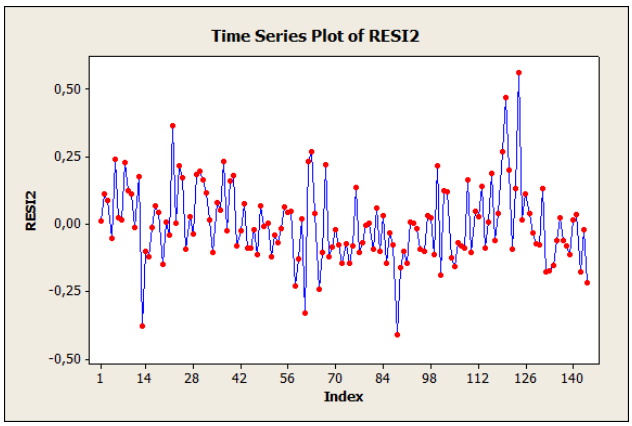


**Figure A.24.:** The time series plot shows that there aren't any trends, but the residuals are independent: it's useful to see a systematic error.

of normality of the residuals (**Figure A.25**), the test for equal variances (**Figure A.26**) and the independence of the residuals (**Figure A.27**).

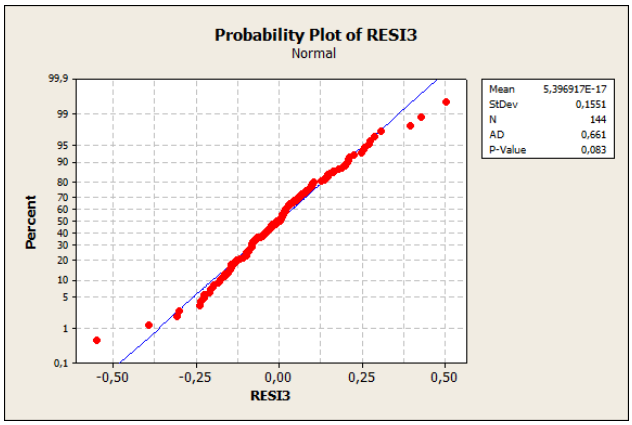


**Figure A.25.:** The probability plot shows the normality of the residuals (p-value bigger than 0,05)

After these verifications, it is possible to infer that orifice and feed rate influence the roughness. In addition to find the influencing parameters, it's important to establish which level of each factor is the best, in this case to minimize the roughness.
The employed statistical method is the multiple comparisons, using the Tuckey's test.

### Factor: orifice

$T_\alpha = \frac{q_\alpha(a, df_E)}{\sqrt{2}} = \frac{q_{0,025}(2,140)}{\sqrt{2}} = \frac{3{,}58}{\sqrt{2}} = 2,53$

The critic value is: $T_\alpha \sqrt{\hat{V}(\hat{D}_{ij})} = T_\alpha \sqrt{MS_E \frac{2}{b \cdot n}} = 2,53 \sqrt{0,02456 \cdot \frac{2}{3 \cdot 4}} = 0,162$

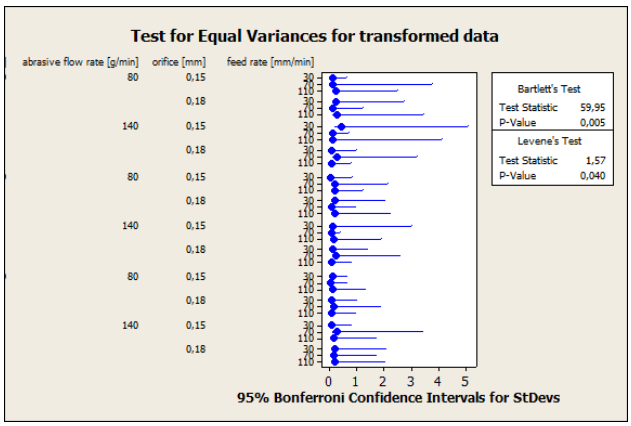


**Figure A.26.:** The test for equal variances shows that the variances are homogenous (p-value bigger than 0,05)

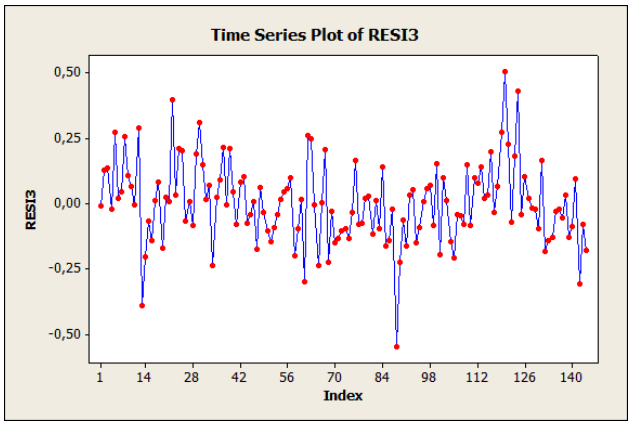


**Figure A.27.:** The time series plot shows that there aren't any trends, but the residuals are independent.

Mean of each level of orifice:
- 0,15 = 2,0815 µm
- 0,18 = 2,5179 µm

| differences | 0,18 |
|---|---|
| **0,15** | 0,4364 |

The orifice of 0,15 mm is the best to minimize the roughness.

### Factor: feed rate

$T_\alpha = \frac{q_\alpha(a,df_E)}{\sqrt{2}} = \frac{q_{0,025}(3,140)}{\sqrt{2}} = \frac{4,12}{\sqrt{2}} = 2,91$

The critic value is: $T_\alpha\sqrt{\hat{V}(\hat{D}_{ij})} = T_\alpha\sqrt{MS_E\frac{2}{a\cdot n}} = 2,91\sqrt{0,02456\cdot\frac{2}{2\cdot 4}} = 0,228$

Mean of each level of feed rate:
- 30 = 2,1885 µm
- 70 = 2,2592 µm
- 110 = 2,4514 µm

| **differences** | **70** | **110** |
|---|---|---|
| **30** | 0,071 | 0,2629 |
| **70** | | 0,1922 |

The best parameters of feed rate can be chosen arbitrary between 30 and 70 mm/min.

# B. PEARSON-HARTLEY CHARTS

In any experimental design problem, a critical decision is the choice of sample size which determines as a consequence the number of replicates to run. Generally, if the experimenter is interested in detecting small effects caused by the influencing factors more replicates are required than if the experimenter is interested in detecting large effects.

## B.1. Operating characteristic curves

Before describing the operating characteristic curves, it is necessary a statistical review.
The *type I error* is the probability to reject a hypothesis when it is true, while the *type II error* is the probability not to reject a hypothesis that is false. The power of a statistical test is the probability that the test will reject the null hypothesis when the null hypothesis is actually false (the probability of not committing a type II error, or making a false negative decision).
The *critical region D* of a hypothesis test is the function $\pi_D : \Theta \rightarrow [0, 1]$, defined by:
$\pi_D(\vartheta) = P_\vartheta \{X \epsilon D\}$
- if $\vartheta \epsilon \Theta_D$ (the null hypothesis is true), then $\pi_D$ is the type I error
- if $\vartheta \epsilon \Theta_A$ (the null hypothesis is false), then $\pi_D$ is the type II error

The operating characteristic curves are the plots of the type II error probability of a statistical test for a particular sample size versus a parameter that reflects the extent to which the null hypothesis is false. These curves can be used to guide the experimenter in selecting the number of replicates so that the design will be sensitive to important potential differences in the treatments. The type II error probability

of a statistical test is:

$$\beta = 1 - P\{reject\, H_0 \,|\, H_0\, is\, false\} = 1 - P\{F_0 > F_{\alpha,a-1,N-a} \,|\, H_0\, is\, false\} \quad \text{(B.1)}$$

To evaluate the probability statement in the previous equation, it's necessary to know the distribution of the test statistic F0 if the null hypothesis is false. It can be shown that, if $H_0$ is false, the statistic $F_0 = {}^{MS_t}/_{MS_E}$ is distributed as a non-central F random variable with a-1 and N-a degrees of freedom and the non-centrality parameter δ. If δ=0, the non-central F distribution becomes the usual (central) F distribution. Operating characteristic curves are used to evaluate the probability statement in the previous equation.
These curves plot the probability of type II error against a parameter Φ:

$$\Phi^2 = \frac{n \sum \tau_i^2}{a\sigma^2} \quad \text{(B.2)}$$

The quantity $\sigma^2$ is related to the non-centrality parameter δ with this equation:

$$\delta = \sigma^2 \cdot \nu_1 \quad \text{(B.3)}$$

In [46] curves are available for α= 0,05 and α= 0,01 and a range of degrees of freedom for numerator and denominator. An example is shown in **Figure B.1**.

In the Matlab® program implemented by the author of this work and Nicolò Vecchi, it is possible to compute automatically the power in a much easier and faster way compared to consulting the traditional printed charts[46]. An example is shown in the **Figure B.2**.

In using the operating characteristic curves, the experimenter has to specify the parameter Φ. This is often difficult to do in practice.
The statistical power analysis can either be done before (*a priori* power analysis) or after (*post hoc* power analysis) data are collected. A priori power analysis is conducted prior to the research study, and is typically used in estimating the necessary sample sizes to achieve adequate power. Post-hoc power analysis is conducted after a study has been completed, and uses the obtained sample size and effect size to determine what the power was in the study, assuming the effect size in the sample is equal to the effect size in the population. Whereas the utility of prospective power analysis in experimental design is universally accepted, the usefulness of retrospective techniques is controversial, falling for the temptation to use the statistical analysis of the collected data to estimate the power will result in uninformative and misleading values.

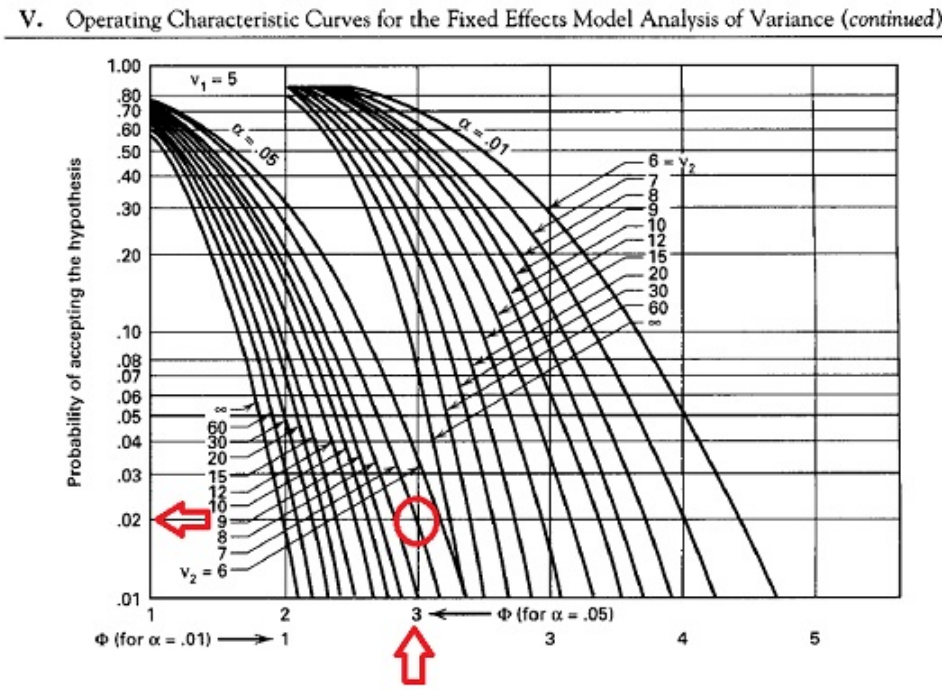


**Figure B.1.:** An exemple of Pearson-Hartley Charts.

The operating characteristic curves can be used to assist the experimenter in determining an appropriate sample size (number of replicates n) for a two-factorial design. The appropriate value of the parameter $\Phi$ and the numerator and denominator degrees of freedom are shown in the **Table B.1**.

**Table B.1.:** Operative characteristic curve parameters for the two factor-factorial, fixed effects model.

| **Factor** | $\Phi^2$ | **Numerator degrees of feedrom** | **Denominator degrees of freedom** |
|---|---|---|---|
| **A** | $\frac{bn\sum_{i=1}^{a}\tau_i^2}{a\sigma^2}$ | a-1 | ab(n-1) |
| **B** | $\frac{an\sum_{j=1}^{b}\beta_j^2}{b\sigma^2}$ | b-1 | ab(n-1) |
| **AB** | $\frac{n\sum_{i=1}^{a}\sum_{j=1}^{b}(\tau\beta)_{ij}^2}{\sigma^2[(a-1)(b-1)+1]}$ | (a-1)(b-1) | ab(n-1) |

A very effective way to use these curves is to find the smallest value of $\Phi^2$ corresponding to a specified difference between any two treatment means. For example, if the difference in any two row means is D, then the minimum value of $\Phi^2$ is:

$$\Phi^2 = \frac{bnD^2}{2a\sigma^2} \tag{B.4}$$

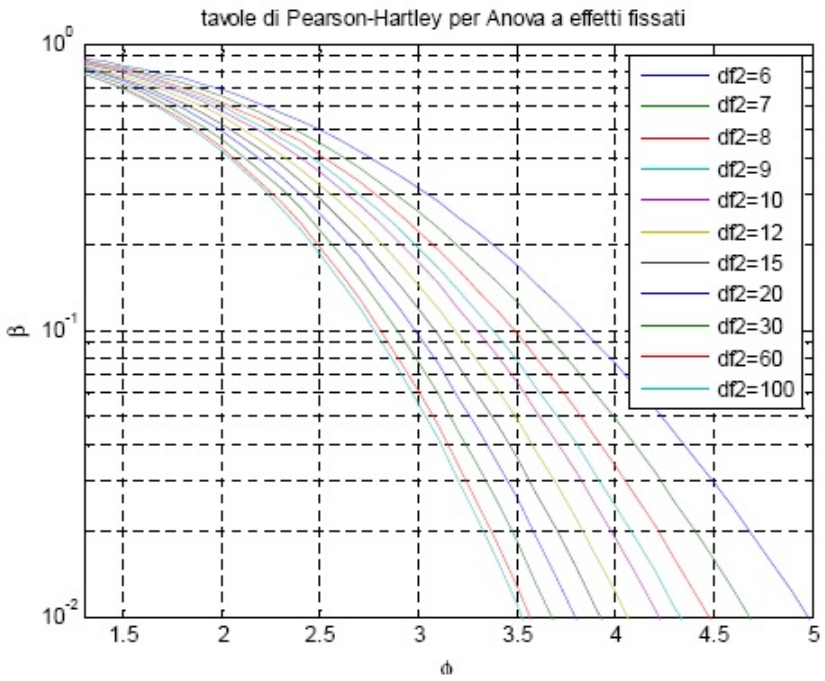


**Figure B.2.:** An example of the ouput of the program, which can plot the operating characteristic curves.

Whereas if the difference in any two column means is D, then the minimum value of $\Phi^2$ is :

$$\Phi^2 = \frac{anD^2}{2b\sigma^2} \tag{B.5}$$

Finally, the minimum value of $\Phi^2$ corresponding to a difference of D between any two interaction effects is:

$$\Phi^2 = \frac{nD^2}{2\sigma^2[(a-1)(b-1)+1]} \tag{B.6}$$

Thus, it is possible to conclude that n replicates are enough to provide the desired sensitivity as long as the estimation of the standard deviation in sot seriously in error. If in doubt, the experimenter could repeat the above procedure with other values of σ to determine the effect of misestimating this parameter on the sensitivity of the design.

## B.2. Program for calculation of power and sample size

The source code for the calculation power of the statistical test is reported below.

```
function Trolli_Vecchi
%
% Programma calcolo_tavole_Pearson_Hartley :
%
% Programma didattico il calcolo della potenza del test F per l'ANoVA
% per modello a effetti fissati e effetti casuali e per plottare
% tavole di Pearson Hartley.
%
% Autori:  Alessandro Trolli
% Nicolò Vecchi
%
% Menù di scelta tra calcolo potenza e plot tavole
continua='y';
while (continua=='y')
clear all
close all
clc
scelta1= menu('Menù principale','Calcolo Potenza','Plot Tavole',...  'Quit');
if (scelta1==1)
% Pulisco la memoria.  clear all close all clc home
% Menu' per scegliere ANOVA.
ico_v = menu('Menu" principale.','ANOVA a effetti fissati','ANOVA a effetti casuali',...

'Informazioni sul programma','Modalita" di utilizzo del programma','Quit');
% Inizio ciclo if :  ANOVA effetti fissati
if (ico_v==1),
clear all
warning off
format short g
dlgTitle = 'Fissati'; prompt = {'livello di confidenza:',...
'df1:'...
'df2:',...
'parametro phi:'};
def = {'0.95','4','25','1.54',};
lineNo = 1;
answer = inputdlg(prompt,dlgTitle,lineNo,def);
alfa = str2num(char(answer(1)));
if (alfa<0)|(alfa>=1)
disp(' ')
disp ('Inserire alfa corretto')
disp(' ')
disp('Powered by Trolli Vecchi ')
disp (' ')
continua=input('Vuoi utilizzare di nuovo il programma?  (y/n) ','s');
elseif (alfa>=0)|(alfa<1)
df1 = str2num(char(answer(2)));
df2 = str2num(char(answer(3)));
```

```
phi = str2num(char(answer(4)));
npf=phi^2*(df1+1);
F=icdf('ncf',alfa,df1,df2,0);
Beta=cdf('ncf',F,df1,df2,npf)
Potenza=1-Beta
disp(' ')
disp('Powered by Trolli Vecchi ')
disp (' ')
continua=input('Vuoi utilizzare di nuovo il programma?  (y/n) ','s');
end
% ANOVA effetti casuali
elseif (ico_v==2),
clear all
warning off
format short g
dlgTitle = 'Casuali';
prompt = {'livello di confidenza:',...
'df1:'...
'df2:',...
'parametro lambda:'};
def = {'0.95','4','30','3',};
lineNo = 1;
answer = inputdlg(prompt,dlgTitle,lineNo,def);
alfa = str2num(char(answer(1)));
if (alfa<0)|(alfa>=1)
disp(' ')
disp ('Inserire alfa corretto')
disp(' ')
disp('Powered by Trolli Vecchi ')
disp (' ')
continua=input('Vuoi utilizzare di nuovo il programma?  (y/n) ','s');
elseif (alfa>=0)|(alfa<1)
df1 = str2num(char(answer(2)));
df2 = str2num(char(answer(3)));
lambda = str2num(char(answer(4)))
F=icdf('ncf',alfa,df1,df2,0);
Beta=cdf('ncf',F/(lambda^2),df1,df2,0)
Potenza=1-Beta
disp(' ')
disp('Powered by Trolli Vecchi ')
disp (' ')
continua=input('Vuoi utilizzare di nuovo il programma?  (y/n) ','s');
end
elseif (ico_v==3),
nome='ABOUT.TXT';
ftmp=legginfo(nome);
disp(' ')
disp('Powered by Trolli Vecchi ')
disp (' ')
continua=input('Vuoi utilizzare di nuovo il programma?  (y/n) ','s');
elseif (ico_v==4),
nome='USAGE.TXT';
```

```
ftmp=legginfo(nome);
disp(' ')
disp('Powered by Trolli Vecchi ')
disp (' ')
continua=input('Vuoi utilizzare di nuovo il programma?  (y/n) ','s');
% Caso '5' :  Esco dal programma.
else (ico_v==5)
return
% Fine ciclo if
end
elseif (scelta1==2)
ico_v = menu('Menu" principale.','ANOVA a effetti fissati','ANOVA a effetti casuali',...
'Quit');
% Inizio ciclo if :  ANOVA effetti fissati
if (ico_v==1),
clear all
warning off
format short g
dlgTitle = 'Fissati'; prompt = {'livello di confidenza:',...
'df1:'...
'limite inf.  phi:'...
'limite sup phi:'};
def = {'0.99','1','1','5'};
lineNo = 1;
answer = inputdlg(prompt,dlgTitle,lineNo,def);
alfa = str2num(char(answer(1)));
if (alfa<0)|(alfa>=1)
disp(' ')
disp ('Inserire alfa corretto')
disp(' ')
disp('Powered by Trolli Vecchi ')
disp (' ')
continua=input('Vuoi utilizzare di nuovo il programma?  (y/n) ','s');
elseif (alfa>=0)|(alfa<1)
df1 = str2num(char(answer(2)));
phi_inf=str2num(char(answer(3)));
phi_sup=str2num(char(answer(4)));
if(phi_inf>=phi_sup)
disp(' ')
disp ('Inserire i valori di phi correttamente')
disp(' ')
disp('Powered by Trolli Vecchi ')
disp (' ')
continua=input('Vuoi utilizzare di nuovo il programma?  (y/n) ','s');
elseif (phi_inf<phi_sup)
for i=1:11 df2=[6 7 8 9 10 12 15 20 30 60 100];
phi2=phi_inf:0.1:phi_sup;
npf2=phi2.^2.*(df1+1);
F=icdf('ncf',alfa,df1,df2(i),0);
Beta2(:,i)=cdf('ncf',F,df1,df2(i),npf2);
phi2=phi2;
end
```

```
semilogy(phi2,Beta2)
grid on
ylim([0.01 1])
xlim([phi_inf phi_sup])
xlabel('\phi')
ylabel('\beta')
title('tavole di Pearson-Hartley per Anova a effetti fissati ')
legend('df2=6','df2=7','df2=8','df2=9','df2=10','df2=12','df2=15','df2=20',...
'df2=30','df2=60','df2=100')
disp(' ')
disp('Powered by Trolli Vecchi ')
disp (' ') continua=input('Vuoi utilizzare di nuovo il programma?  (y/n) ','s');
end
end
%
%ANOVA random effects
elseif (ico_v==2)
clear all
warning off
format short g
dlgTitle = 'Casuali'; prompt = {'livello di confidenza:',...
'df1:',...
'limite inf.  lambda:',...
'limite sup.  lambda:'};
def = {'0.99','1','20','190'};
lineNo = 1;
answer = inputdlg(prompt,dlgTitle,lineNo,def);
alfa = str2num(char(answer(1)));
if (alfa<0)|(alfa>=1)
disp(' ')
disp ('Inserire alfa corretto')
disp(' ')
disp('Powered by Trolli Vecchi ')
disp (' ')
continua=input('Vuoi utilizzare di nuovo il programma?  (y/n) ','s');
elseif (alfa>=0)|(alfa<1)
df1 = str2num(char(answer(2)));
lambda_inf=str2num(char(answer(3)));
lambda_sup=str2num(char(answer(4)));
if(lambda_inf>=lambda_sup)
disp(' ')
disp ('Inserire i valori di lambda correttamente')
disp(' ')
disp('Powered by Trolli Vecchi ')
disp (' ')
continua=input('Vuoi utilizzare di nuovo il programma?  (y/n) ','s');
elseif (lambda_inf<lambda_sup)
for i=1:11
df2=[6 7 8 9 10 12 15 20 30 60 100];
lambda1=lambda_inf:0.1:lambda_sup;
F=icdf('ncf',alfa,df1,df2(i),0);
Beta1(:,i)=cdf('ncf',F./(lambda1.^2),df1,df2(i),0);
```

```
end
semilogy(lambda1,Beta1)
hold on
grid on
ylim([0.01 1])
xlim([lambda_inf lambda_sup])
xlabel('\lambda')
ylabel('\beta')
title('tavole di Pearson-Hartley per Anova a effetti fissati (df_1=1)')
legend('df2=6','df2=7','df2=8','df2=9','df2=10','df2=12','df2=15','df2=20',...
'df2=30','df2=60','df2=100')
disp(' ')
disp('Powered by Trolli Vecchi ')
disp (' ')
continua=input('Vuoi utilizzare di nuovo il programma?  (y/n) ','s');
end
end
else (ico_v==3)
return
end
else return
end
end
```

# C. DATA SHEET

In this Appendix the data sheet of water jet system and technical instruments are presented.

## C.1. Water jet cutting system

The water jet cutting system is ByJet Classic 3015 (**Figure C.1**). The data sheet is presented in **Table C.1**.

| **Name** | BYJET CLASsIC 3015 |
|---|---|
| **Cutting range** | x = 3048 mm; y = 1524 mm; z = 250 mm |
| **Maximum cutting speed** | 50 m/min |
| **Minimum traverse speed** | 0,001 m/min |
| **Positioning accuracy** | ± 0,08 mm / axis |
| **Repeatability** | ± 0,025 mm / axis |
| **Maximum material thickness** | 200 |
| **Capacity of the cutting tank** | 4,2 $m^3$ |
| **Total electrical supply machine** | 64 kW |
| **Maximum operating pressure** | 3800 bar |

**Table C.1.:** Data sheet of ByJet Classic 3015

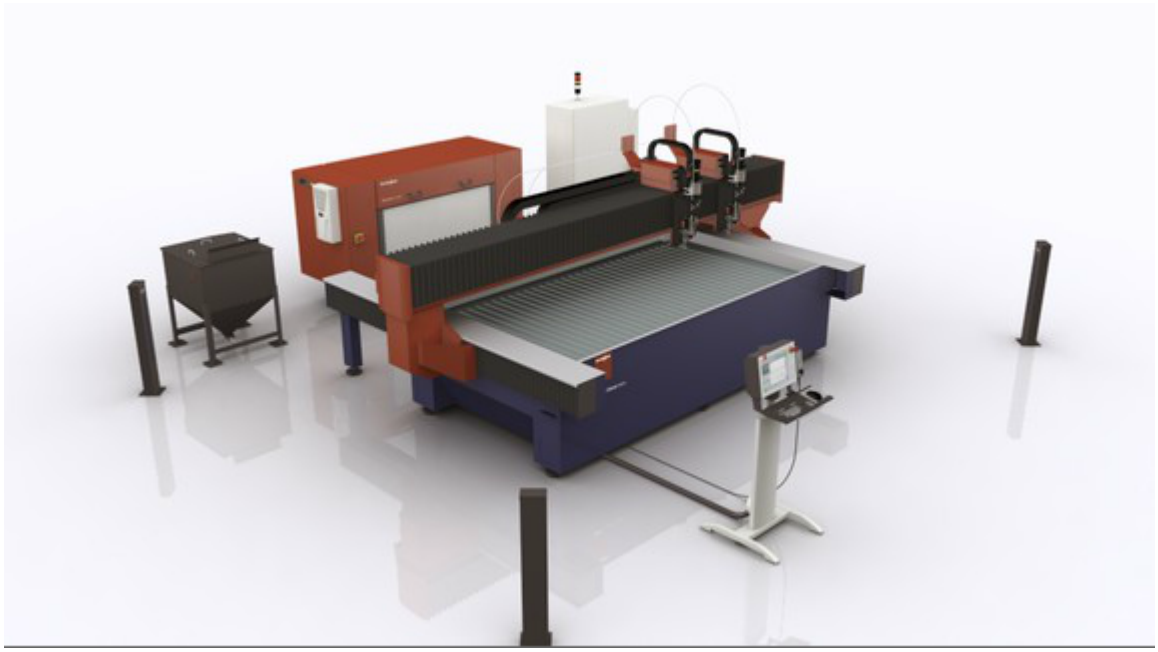

**Figure C.1.:** Water jet cutting system used in this experimentation

## C.2. Optical microscope

The optical microscope is Motic SMZ - 140 Series (**Figure C.2**). The data sheet is presented in **Table C.2**.

| | |
|---|---|
| **Name** | Motic SMZ - 140 Series |
| **Optical system** | Greenough Stereocopic |
| **Interpupillary adjustment** | 54 mm - 76 mm |
| **Magnification range** | 15X - 60X |
| **Working distance** | 33 mm - 200 mm |
| **Software** | Clemex Captiva 5.0 |

**Table C.2.:** Data sheet of Motic SMZ - 140 Series

**Figure C.2.:** The optical microscope used in this experimentation

## C.3. Scanning electron microscope

The scanning electron microscope is Evo 50 XVP (**Figure C.3**). The data sheet is presented in **Table C.3**.

| | |
|---|---|
| **Name** | Evo 50 XVP |
| **Acceleration voltage** | 0,2 - 30 kV |
| **Pressure range** | 1 - 750 Pa |
| **Resolution** | 3,0 nm |
| **Magnification** | 5X - 150.000X |
| **Motion system** | x = 100 mm; y = 125 mm; z = 35 mm |
| **Maximum dimension (specimen)** | h = 120 mm; d = 250 mm |
| **Maximum weight (specimen)** | 0,5 kg (no tilted) - 2 kg (tilted) |
| **Software** | SEM V.05.04.05.00 |

**Table C.3.:** Data sheet of Motic SMZ - 140 Series


**Figure C.3.:** The scanning electron microscope used in this experimentation

## C.4. Profilometer

The profilometer is Mitutoyo SV - 2000N2 (**Figure C.4**). The data sheet is presented in **Table C.4**.

| **Name** | Mitutoyo SV - 2000N2 |
|---|---|
| **Stylus stroke** | 2 μm |
| **Resolution** | 0,0001 μm |
| **Minimum cut-off** | 0,025 mm |
| **Straightness** | 0,3 μm per 50 mm |
| **Motion system** | x = 50 mm; z = 800 μm |
| **Software** | Surfpak |

**Table C.4.:** Data sheet of Mitutoyo SV - 2000N2

**Figure C.4.:** The profilometer used in this experimentation

# Bibliography


[1] M.Monno, M. Annoni, and C. Ravasio, *Water jet, a flexible technology.* Polipress, 2007.

[2] A. Momber and R.Kovacevic, *Principles of Abrasive Water Jet Machining.* Springer, 1998.

[3] D. Miller, "Micro abrasive waterjets," in *10th American Waterjet Conference*, Houston (USA), 14 August 1999.

[4] O. Blatnik *et al.*, "Waterjet machining for medm tools," 2011.

[5] I. Sabotin, "Repeatability and limitations of water-jet based micro-tooling process chain," in *7th International Conference on Multi-Material Micro Manufacture*, Bourg en Bress and Oyonnax (France), 23 November 2010.

[6] T. Aklint *et al.*, "Abrasive waterjet cutting for micro manufacturing," in *7th International Conference on Multi-Material Micro Manufacture*, Bourg en Bress and Oyonnax (France), 23 November 2010.

[7] P. Gudimetla, J. Wang, and W. Wong, "Kerf formation analysis in the abrasive waterjet cutting of industrial ceramics," *Journal of Materials Processing Technology*, vol. 128, pp. 123 – 129, 2002.

[8] J. Wang, "Predictive depth of jet penetration models for abrasive waterjet cutting of alumina ceramics," *International Journal of Mechanical Sciences*, vol. 49, pp. 306 – 316, 2007.

[9] D. Shanmugam, J.Wang, and H.Liu, "Minimisation of kerf tapers in abrasive waterjet machining of alumina ceramics using a compensation technique," *International Journal of Machine Tools and Manufacture*, vol. 48, pp. 1527 – 1534, 2008.

[10] A. Devineni, "Awsj cutting of glass: An experimental study of the effect of process parameters on the depth of cut and kerf width using doe," in *International Conference on Mechanical and Electrical Technology*, 2010.

[11] F. Kolahan and A. H. Khajavi, "Modeling and optimization of abrasive waterjet parameters using regression analysis," *International Journal of Aerospace and Mechanical Engineering*, vol. 5, pp. 248 – 253, 2011.

[12] J. Wang and D.M.Guo, "The cutting performance in multipass abrasive waterjet machining of industrial ceramics," *Journal of Materials Processing Technology*, vol. 133, pp. 371 – 377, 2003.

[13] R. Guo, C. Wang, and A. Yang, “Piezoelectric properties of the 1-3 type porous lead zirconate titanate ceramics,” *Journal of the European Ceramic Society*, vol. 24, pp. 3295 – 3302, 2011.

[14] A. Bellosi, D. Sciti, and S. Guicciardi, “Synergy and competition in nano- and micro-design of structural ceramics,” *Journal of the European Ceramic Society*, vol. 24, pp. 3295 – 3302, 2004.

[15] B. Watson, J. Friend, and L. Yeo, “Piezoelectric ultrasonic micro/milli-scale actuators,” *Sensors and Actuators A*, vol. 152, pp. 219 – 233, 2009.

[16] M. Monno and M. Annoni, *La tecnologia Waterjet / Abrasive Water Jet*. Notes for Mechanical Engineering course "Laboratorio di Tecnologie Speciali", 2010.

[17] H. Liu and D. McNiel, “Versatility of waterjet technology: form macro to micro machining for most materials,” in *18th International Conference on Water Jetting*, Graz (Austria), 19 October 2010.

[18] H. Liu, “Making waterjet-cut parts more fatigue resistant,” 2009. [Online]. Available: www.thefabricator.com/article/waterjetcutting/making-waterjet-cut-parts-more-fatigue-resistant

[19] H. Maurer, “Waterjet goes micro,” in *MM Live 2010*, Conventry (United Kingdom), 19 October 2010.

[20] D. Miller, “Micromachining with abrasive waterjets,” *Journal of Materials Processing Technology*, vol. 149, pp. 37 – 42, 2004.

[21] W. Siegenthaler, “Defining precision: revolutionary abrasive waterjet technology,” in *MM Live 2010*, Conventry (United Kingdom), 19 October 2010.

[22] A. Jauregui *et al.*, “Evaluation of micromechanical manufacturing process for microfluidic devices,” *International Journal of Advanced Manufacturing Technology*, vol. 48, pp. 963 – 972, 2010.

[23] M. Frotscher *et al.*, “Achieving small structures in thin ni-ti sheets for medical applications with water jet and micro machining: a comparison,” *Journal of Materials Engineering and Perforamance*, 2006.

[24] D. Miller, “Micromachining with abrasive waterjets,” in *MM Live 2010*, Conventry (United Kingdom), 19 October 2010.

[25] H. Liu, “Micro awj technology for meso-micro machining,” in *WJTA IMCA Conference and Expo*, Houston (United States), 19 September 2011.

[26] S. Formenti, “Controllo elettronico di attuatori per microfluidica a piezoelettrico,” Ph.D. dissertation, Politecnico di Milano, FacoltÃ  di Ingegneria Elettronica, 2010.

[27] L. Chen, E. Siores, and W. Wong, “Kerf characteristic in abrasive water jet cutting of ceramic materials,” *International Journal of Machined Tools Manufacturing*, vol. 36, pp. 1201 – 1206, 1996.

[28] L. Bertini, “Modelling, testing and design of a miniaturized piezoelectric actuator,” Ph.D. dissertation, UniversitÃ  di Pisa, FacoltÃ  di Ingegneria Meccanica, 2010.

[29] M. Boniardi, *Materiali Ceramici*. Notes for Mechanical Engineering course "Materiali", 2008.

[30] B. Andersen *et al.*, “Performance of piezoelectric ceramic multilayer components based on hard and soft pzt,” pp. –. [Online]. Available: www.noliac.com

[31] D. Campolo, R. Sahai, and R. Fearing, “Development of piezoelectric bending actuators with embedded piezoelectric sensors for micromechanical flapping mechanism,” pp. –.

[32] D. Miller, “New abrasive waterjet system to compete with lasers,” in *WJTA American Waterjet Conference*, Houston (USA), 21-23 August 2005.

[33] A. E. Domiaty and A. A. Rahman, “Fracture mechanics-based model of abrasive waterjet cutting for brittle materials,” *International Journal of Advanced Manufacturing Technology*, vol. 113, pp. 573 – 584, 1997.

[34] M. Kong, D. Axinte, and V. W., “Aspects of material removal mechanism in plain waterjet milling on gamma titanium aluminide,” *Journal of Material Processing Technology*, vol. 210, pp. 573 – 584, 2010.

[35] D. Arola and M. Ramulu, “Mechanism of material removal in abrasive waterjet machining of common aerospace materials,” in *7th American Water Jet Conference*, Seattle (USA), 28-31 August 1999.

[36] J. Zeng and T. Kim, “An erosion model for abrasive waterjet milling of polycristalline ceramics,” *Wear*, vol. 199, pp. 275 – 282, 1996.

[37] A. Momber and R. Kovacevic, “Hydro-abrasive erosion of refractory ceramics,” *Journal of Materials Science*, vol. 38, pp. 2861 – 2874, 2003.

[38] J. Zeng and T. Kim, “An erosion model of polycristalline ceramics in abrasive waterjet cutting,” *Wear*, vol. 193, pp. 207 – 217, 1996.

[39] G. Choi and G. Choi, “Process analysis and monitoring in abrasive waterjet machining of alumina ceramics,” *International Journal of Machining Tools Manufacturing*, vol. 37, pp. 295 – 307, 1997.

[40] J. Nuffer *et al.*, “Reliability investigation of piezoelectric macro fibre composite (mfc) actuators,” in *Adaptronic Congress 2007*, Gottingen (Germany), 23-24 May 2007.

[41] A. Pighi, “Ottimizzazione del taglio awj per schiume metalliche,” Ph.D. dissertation, Politecnico di Milano, FacoltÃ  di Ingegneria Meccanica, 2010.

[42] A. Iqbal, U. Dar, and G. Hussain, “Optimization of abrasive water jet cutting of ductile materials,” *Journal of Wuhan University of Technology*, vol. 26, pp. 88 – 92, 2011.

[43] R. Groppetti, T. Gutema, and A. D. Lucchio, "A contribution to the analysis of some kerf quality attributes for precision abrasive waterjet cutting," in *14th International Conference on Jetting Technology*, Brugge (Belgium), September 1998.

[44] L. Kahlman, K. Ojmertz, and L. Falk, "Abrasive waterjet testing of thermo-mechanical wear of ceramics," *Wear*, vol. 248, pp. 16 – 28, 2001.

[45] R. B. Williams and D. Inman, "An overview of composite actuators with piezoceramic fibers," pp. – . [Online]. Available: www.smart-material.com

[46] D. Montgomery, *Design and Analysis of Experiments*, fifth edition ed. John Wiley and Sons, 1997.

# Elenco dei simboli

| | |
|---|---|
| AWIJ | abrasive water injection jet |
| AWJ | abrasive water jet |
| AWSJ | abrasive water suspension jet |
| DOE | design of experiments |
| EDM | electrical discharge machining |
| FAWJ | fine abrasive water jet |
| MAWJ | micro water jet |
| MEDM | micro electric descharge machining |
| MEMS | micro electro-mechanical system |
| PZT | lead titanate zirconate |
| SEM | scanning electron microscope |
| WJ | water jet |